
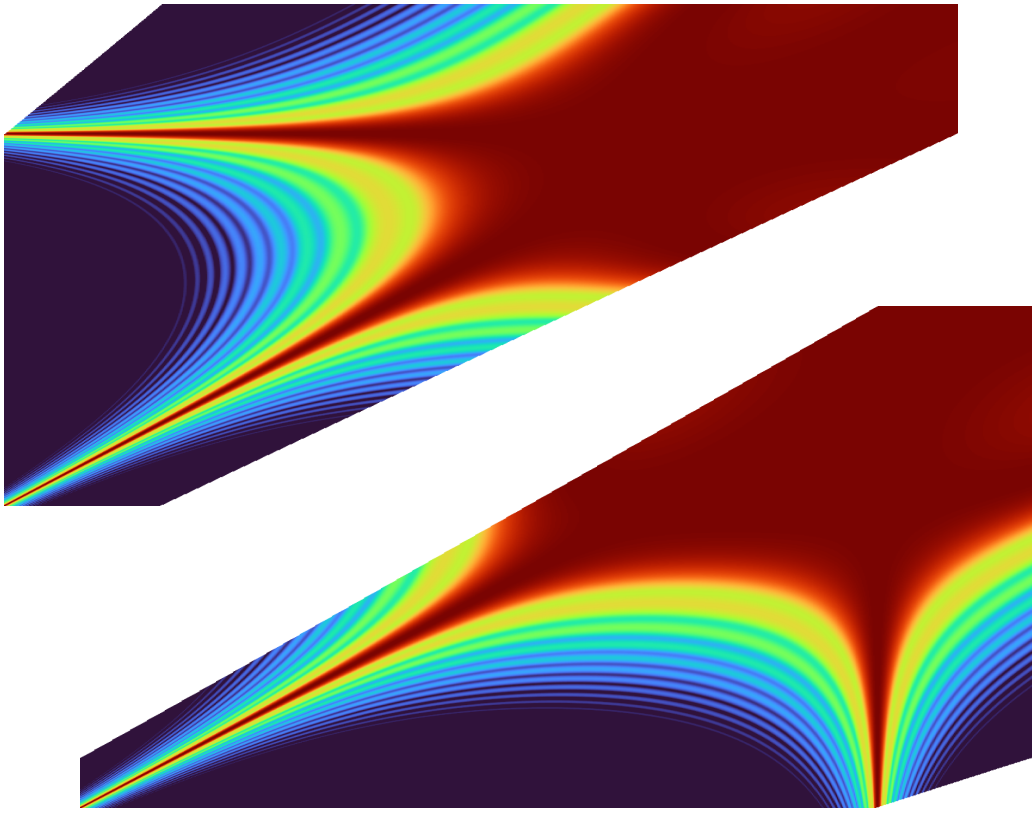


Tasnad Kernetzky

ORCID  0000-0002-5111-5938



Numerical Optimization of

Ultra-Broadband Wavelength Conversion

in Nonlinear Optical Waveguides



Technische Universität München
TUM School of Computation, Information and Technology

Numerical Optimization of Ultra-Broadband Wavelength Conversion in Nonlinear Optical Waveguides

Karl Tasnad Kernetzky

Vollständiger Abdruck der von der TUM School of Computation, Information and Technology der Technischen Universität München zur Erlangung des akademischen Grades eines

Doktors der Ingenieurwissenschaften

genehmigten Dissertation.

Vorsitz:	Prof. Dr.-Ing. Thomas Eibert
Prüfer der Dissertation:	1. Prof. Dr.-Ing. Norbert Hanik
	2. Prof. Dr.-Ing. Christian Jirauschek
	3. Prof. Dr. Christophe Peucheret

Die Dissertation wurde am 28.09.2022 bei der Technischen Universität München eingereicht und durch die TUM School of Computation, Information and Technology am 06.09.2023 angenommen.

To my Family

Preface

This thesis was written during my time as research and teaching assistant in Prof. Norbert Hanik's group [LÜT](#) at the Technical University of Munich. In the first three years of my doctorate from 2015 to 2017, I was working on powerline communications in a joint project with Siemens AG. Although none of that work ended up in this thesis, I am still very grateful for all the [FPGA](#) hardware development skills and insight into corporate life I had the chance to acquire in that phase.

Most of all, I need to thank Prof. Hanik for first supervising my master's thesis and later hiring me as a doctoral researcher. He always made sure I had all the freedom I could ask for. He never built up any pressure which admittedly sometimes lead to interesting side-projects like helping Prof. Günter Söder with the online-learning platform [lntwww](#) or programming a website for tracking kicker matches at the institute. He was helpful whenever I approached him, be it for research questions or help with resolving a conflict with a colleague. With no doubt, Prof. Hanik is an outstanding supervisor. He always knows when somebody needs to be cheered up or reassured that research can be tough.

I learned in the first part of my doctorate that working more or less on your own is a very daunting task. Therefore, I was very grateful that in the second phase I had the opportunity to work together with Ulrike Höfler, Yizhao Jia, Gregor Ronniger and Isaac Sackey. I thank you for all the fruitful and interesting discussions about (not only) research and the nice collaboration over the years!

One of the best parts of a doctorate is the opportunity to work with outstandingly (sometimes even intimidatingly!) smart colleagues. So I want to thank all of my coworkers at [COD](#), [LNT](#) and [LÜT](#) for being – and hopefully staying – a big part of my life! I obviously also enjoyed the many times I was bouldering, climbing, hiking and – last but not least – kicking with so many of you!

Of course, I also made friends over the almost 8 years at the institute. In particular, I want to mention Patrick Schulte for being one of the most humble persons I know and for sacrificing many of his thesis writing hours to ensure a healthy nutrition for us. I will never forget the interesting discussions about society, arts and much much more with Benedikt Leible. Among the countless things I could write about my friendship with Onur Günlü, I just want to mention that he taught me to gain some healthy distance to my work and helped me to my first paper as his co-author. I am not even sure how many *try not to die* experiences I had with Roberto Ferrara in the mountains, but each of them was a unique and very nice experience!

One of my main tasks besides research was being a system administrator for the simulation cluster at the institute. That's where I got to know Thomas Wiegart more closely and where we discovered how much we have in common. Thank you for all the fun hours in the server room, but also the countless hikes, (astro) photo sessions and many more things!

Last but by all means not least, I want to thank my parents, my parents in law and my wife Sophia. I can not list all the things I am grateful, but want to name some. My parents for always supporting me without hesitation and never questioning my choice of studies. My parents in law for all the help with our two small children and for being the parents of such a wonderful being. And Sophia for teaching me a lot about (scientific) writing, for selflessly taking care of our children to give me time to work on the thesis, for tolerating my preference to work rather late than early in the day and of course for becoming the most important part of my life ❤️.

Munich, September 2022

Tasnad Kernetzky

Abstract

This thesis discusses how optical material nonlinearity can be used for ultra-broadband all-optical signal processing in **nano-rib** waveguides and optical fibers.

It starts with an introduction to nonlinear optics, especially the so-called **four-wave mixing (FWM)** process which is used for the signal processing. To achieve **FWM** with high efficiency, it is necessary to perform numerical **phase matching** – the process of finding optimal laser wavelengths and laser-to-waveguide mode assignments.

It is further shown how a high processing bandwidth (in the sense of large range of signal wavelengths) can be achieved by optimizing the geometry of the used waveguides.

A **continuous wave** propagation simulation is presented, which predicts the output power of the desired light wave to a high accuracy.

The thesis later explores whether **FWM** with three or four interacting waveguide modes is feasible in **nano-rib** waveguides and fiber waveguides. It is shown that the case with four modes is impossible and three modes only work with strongly reduced bandwidth and only in **nano-rib** waveguides.

Simulation results are compared to measurements of two manufactured waveguides with the result that the simulation reliably predicts the best-case behavior.

Finally, a special case of **phase matching** in the TE_2 mode of a **nano-rib** waveguide is shown, which enables very flexible operation modes of the waveguide.

Zusammenfassung

Diese Arbeit erörtert wie Materialnichtlinearität für extrem breitbandige und rein optische Signalverarbeitung in **nano-rib** Wellenleitern und Glasfasern verwendet werden kann.

Sie beginnt mit einer Einführung in das Gebiet der nichtlinearen Optik, insbesondere wird die Vierwellenmischung (**FWM**) behandelt, die zur Signalverarbeitung verwendet wird. Um die Effizienz des **FWM** zu maximieren, muss eine numerische Optimierung zur Phasenanpassung (“**phase matching**”) durchgeführt werden. Bei diesem Prozess werden die Laserwellenlängen und die Zuordnung von Lasern zu Modem optimiert.

Des Weiteren wird gezeigt, wie eine hohe Signalverarbeitungsbandbreite (im Sinne von einem großen Bereich von Signalwellenlängen) erzielt werden kann, indem die Wellenleitergeometrie optimiert wird.

Weiter wird eine Simulation basierend auf rein sinusförmigen Wellen (**CW**) vorgestellt, mit der die Leistung der erwünschten Wellen am Wellenleiterausgang in guter Näherung vorausgesagt werden kann.

Danach wird die Machbarkeit von **FWM** mit drei oder vier interagierenden Moden in **nano-rib** Wellenleitern und Glasfasern erörtert. Es wird gezeigt, dass der Fall mit vier Moden nicht verwendbar ist und dass **FWM** mit drei Moden ausschließlich in **nano-rib** Wellenleitern und auch nur mit stark reduzierter Bandbreite verwendbar ist.

Später werden Simulationsergebnisse mit Messungen von zwei Wellenleitern verglichen und gezeigt, dass die Simulation zuverlässig Voraussagen über den Optimalfall liefert.

Schließlich wird noch ein Spezialfall von Phasenanpassung auf Basis der TE_2 Mode eines **nano-rib** Wellenleiters vorgestellt. Diese Konfiguration ermöglicht einen extrem flexiblen Betrieb des Wellenleiters.

Contents

1. Introduction	1
2. Fundamentals of Waveguide Modes and Four-Wave Mixing	5
2.1. Waveguide Modes and Dispersion	5
2.1.1. Modeling the E-Field and Waveguide Modes	6
2.1.2. Dispersion	9
2.2. Examples of Light Waveguides	13
2.2.1. Silica Fibers	14
2.2.2. Silicon on Insulator Nano-Rib Waveguides	17
2.3. Computing Waveguide Modes	22
2.3.1. Analytical Methods	22
2.3.2. An Approximate Method by Marcatili	23
2.3.3. Numerical Finite Difference Methods	24
2.3.3.1. The Semi-Vectorial Linear Polarized FDM Solver	25
2.3.3.2. The Full-Vectorial FDM Solver	28
2.4. Material Nonlinearity and Four-Wave Mixing	29
2.4.1. The Nonlinear Material Polarization	29
2.4.2. Electronic Contribution to Nonlinearity	34
2.4.3. Molecular Contribution to Nonlinearity	35
2.4.4. Further Nonlinear Processes	37
2.4.5. Bragg Scattering and Optical Phase Conjugation	37
2.4.6. Phase Matching	39
2.4.7. Idler Power Estimation	40
3. Numerical Phase Matching and Waveguide Optimizations	43
3.1. Numerical Phase Matching	43
3.1.1. Filtering Mode Combinations	46
3.1.2. Graphical Phase Matching	46
3.1.3. Different Kinds of Phase Matching	48
3.2. Waveguide Geometry Optimization	49
3.2.1. The Effect of Dips	51

4. Frequency Domain Model of Light Propagation in Matter	53
4.1. Derivation of the Propagation Equations	53
4.2. Linear Coupling Model	60
4.3. Nonlinear Coupling Model	61
4.4. Examples of Propagating Waves	63
5. Four-Wave Mixing with Three and Four Modes	67
5.1. Waveguide Geometry and Phase Matching	68
5.2. Considering Modal Overlap	70
5.3. Power Evolution	72
6. Experimental Evaluation	75
6.1. Linear Power Transmission and Group Delay	76
6.2. Normalized Idler Power	80
6.3. Absolute Conversion Efficiency	83
6.4. Geometry Optimization	84
7. Broadband FWM in the TE₂ Mode	85
8. Conclusions	89
A. Appendices	91
A.1. Conventions And Transformations Used Throughout the Thesis	91
A.1.1. Fourier Transform	91
A.1.2. Passband, Analytic, and Baseband Signal Conventions	92
A.1.3. Plane Wave Convention	93
A.1.4. Converting Attenuation	93
A.2. The Maximum of FWM Efficiency	94
A.3. Power Evolution With low Phase Mismatch	97
A.4. Collected Implementation Details and Issues	101
A.4.1. Representing Fields as 3D Vectors of Matrices	101
A.4.2. Linear Combination of LP Modes	101
A.4.3. Optimal FDM Grid	102
A.4.4. PM Optimization for Fibers	103
B. Lists, Notation and Abbreviations	105
B.1. List of Figures	105
B.2. List of Tables	107
B.3. Mathematical Notation	109
B.4. Symbols	110
B.5. Abbreviations	112
Bibliography	115

1

Introduction

The vast majority of internet traffic is carried by different kinds of optical fiber connections. Short-reach access networks typically use multimode fibers to build datacenter, campus or research networks. Metropolitan area networks join the access networks and also provide connections for, e.g., mobile radio stations. The highest bit rates are needed in long-haul trans-oceanic links which transmit data in the terabit per second range over singlemode fibers. All these connections are operated in a very robust way and rarely become the matter of public interest due to failures. For example, the Tonga islands are connected to the internet by only one undersea cable, which was destroyed by an earthquake in January 2022. Although satellite communications were set up as fallback, data rates were lower by many orders of magnitude and internet access was highly restricted. This incident brought the dangers of natural or malignant destruction of these important internet backbone links to public attention.

One ever ongoing research topic is to increase the data throughput capacity of optical links. Major improvements were achieved when two light polarizations were used to transmit orthogonal data, when higher order modulation schemes were applied and most importantly when wavelength division multiplexing was introduced. In the latter technique, several optical channels at different carrier wavelengths in the optical C-band are used in parallel for different data streams. However, the throughput gain by all these techniques starts to saturate and new ideas are explored actively (see e.g. [1] and [2]). The most prominent one is [space-division multiplexing \(SDM\)](#), where either several fiber modes, multiple cores of multicore fibers or a combination of both are modulated with individual data. For example, a throughput of 1.2 Pbit/s was achieved in [3]. Another approach – more related to this work – is to extend transmission beyond the optical C-band. For example, a throughput of 0.6 Pbit/s was achieved in [4] by transmitting in the S- C- and L-bands over a four-core fiber. The problem with this approach is that different transmitters and receivers are needed for different wavelength ranges, increasing the cost and/or decreasing flexibility of transmission systems.

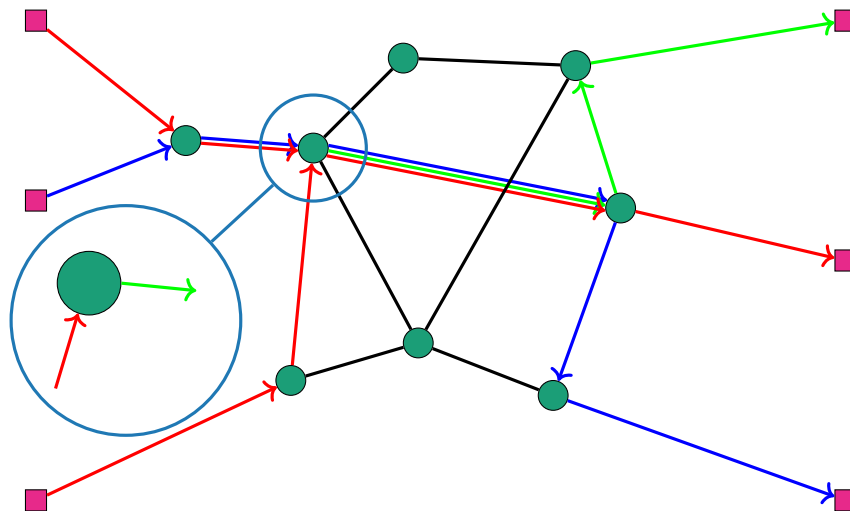


Figure 1.1.: Schematic of a routing scenario where all-optical WLC helps to resolve a wavelength conflict.

However, wavelength converting devices can be used to shift modulated channels from the C-band to other wavelengths into, e.g., the S-band. These devices need to operate in an all-optical fashion without any optical-electrical-optical conversion (otherwise the need for new transmitters and receivers remains). One main task of this thesis are numerical optimizations to build such all-optical wavelength conversion (WLC) devices.

A further potential application of all-optical WLC can be found in optical routing nodes of metropolitan networks and potentially even in access networks. Figure 1.1 shows a schematic of a situation where two signals at the same wavelength (red) arrive at a routing node and should be transmitted in the same outgoing fiber. With WLC, one signal can be converted to another wavelength (green) and transmitted in parallel with the other signals. This can also be beneficial in datacenter interconnect networks [5].

Wavelength conversion has already been studied for optical meshed networks in the late nineties [6]. Among the wavelength multiplexing techniques in [6], “Four-Wave-Mixing in Passive Waveguides” is similar to our approach and to recent experiments [7] with promising results.

The nonlinear response of the fiber’s silica core leads to the accumulation of phase distortions in trans-oceanic links with huge transmission distances. Fortunately, these distortions are deterministic and they can be compensated with a variety of different techniques – a comprehensive overview can be found in [8]. One of these methods is optical phase conjugation (OPC) (also called mid-span spectral inversion), which is illustrated in Fig. 1.2. An OPC device is placed in the middle of the transmission link to phase-conjugate the signal. When the two spans of the link are symmetric w.r.t. loss and dispersion profiles, the accumulated phase distortion from the first half is canceled in the second half. Since the two spans can never be symmetric (especially the loss profile), a higher (odd) number of OPC devices can be distributed along the link to make the spans more symmetric. Mid-span spectral inversion is described in more detail in [9, Chapter 7.3].

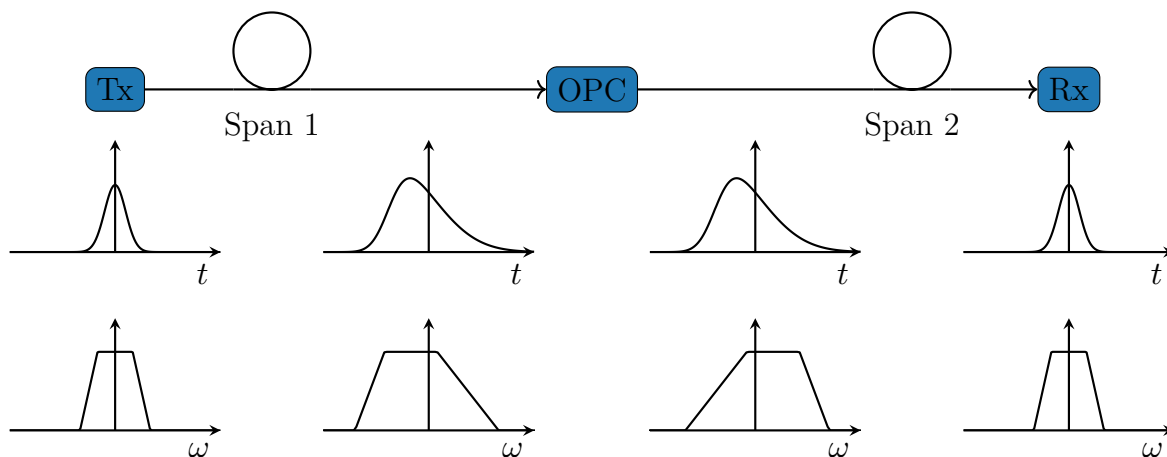


Figure 1.2.: Simple schematic of a transmission system with **optical phase conjugation**.

The idea of compensating distortions by **OPC** has already been suggested in the late seventies [10], demonstrated in a fiber-based experiment in [11] and shown that it can improve optical signal to noise ratio in more recent experiments, e.g. [12]. One goal of our work were numerical optimizations for **OPC** devices.

The propagation of light in every material shows nonlinear effects when the propagating field amplitudes are high enough. While this effect is detrimental in trans-oceanic links mentioned above, it can also be used to achieve all-optical **WLC** and **OPC**. A general survey on all-optical signal processing can be found in [13] – some applications besides **WLC** and **OPC** are wavelength multicasting, tunable optical delays, equalization and optical correlators.

One prominent technique for all-optical signal processing is based on utilizing the third order nonlinear process called **FWM**. In these experiments, the signal is usually launched into a nonlinear medium together with one or two strong pump lasers and a so-called idler wave with the desired properties is generated along the waveguide. There are many experiments based on (highly nonlinear) fibers, e.g. [14], [15] to name two. However, using **silicon on insulator (SOI)** waveguides as nonlinear medium is a very promising alternative, [16] gives a good overview. There are three main reasons why **SOI** waveguides are a better choice than fibers:

1. They can be manufactured in well-established BiCMOS silicon foundries otherwise used to produce electronic chips. This not only lowers costs, but enables co-integration of optics with electronic processing on one single chip [17].
2. Silicon has a more than two orders of magnitude higher nonlinearity compared to silica: $n_2(\text{SiO}_2) = 0.026 \cdot 10^{-18} \text{ m}^2/\text{W}$ [18], $n_2(\text{Si}) = 10 \cdot 10^{-18} \text{ m}^2/\text{W}$ [19, Fig. 6] and [20]. This means the size of the processing device can be drastically reduced from fibers with several hundreds of meters to **SOI** waveguides of only 1 or 2 centimeters.

3. The refractive index contrast in SOI waveguides (roughly $3.48 - 1.44 \approx 2$) is much higher than in fibers ($1.46 - 1.44 \approx 0.02$), which additionally allows smaller waveguide cross sections and thus higher nonlinearity due to higher field amplitudes at the same power.

Therefore, we focus on silica fibers and SOI nano-rib (NR) waveguides in this thesis.

Many all-optical signal processing experiments have been conducted with SOI waveguides. Broadband WLC is shown in theory in [21] and with experimental confirmation in [7], [22]–[24]. One can achieve additional degrees of freedom for optimizing FWM, when more than the fundamental waveguide mode is used. In [25], the authors perform a tedious manual geometry optimization for a strip SOI waveguide to achieve broadband WLC. Such multi-modal WLC was experimentally shown in [26]–[28]. Multi-modal OPC experiments can be found in [29], [30].

Most of our work was conducted in the research project “SPP 2111: Electronic-Photonic Integrated Systems for Ultrafast Signal Processing” [31] by the German research foundation *DFG*. The goal is to develop an integrated, all-optical ultra-broadband photonic signal processor which can be used for OPC and WLC. Our task at Technische Universität München (TUM) was the optimization of laser wavelengths, laser-to-mode assignments and waveguide geometries to achieve broadband FWM with high efficiency. Our partners at Technische Universität Berlin (TUB) and Innovations for High Performance Microelectronics GmbH (IHP) were responsible for the technical aspects of waveguide design like layouting, grating coupler (GC) design, adding mode multiplexers (MUXs), etc. and for manufacturing. Our partners at Fraunhofer-Institut Heinrich-Hertz-Institut für Nachrichtentechnik (HHI) were responsible for conducting WLC system experiments with the waveguides.

The presented material is partly based on our publications [32]–[40]¹. To the best of our knowledge, the numerical phase matching approach presented in Section 3.1 has not been done before.

¹ One further contribution was the joint work [41]. However, it is unrelated to the topic of this thesis.

2

Fundamentals of Waveguide Modes and Four-Wave Mixing

In this chapter, we introduce mathematical basics and concepts relevant for the thesis. The main focus lies on the theory of optical waveguide modes, dispersion, [four-wave mixing \(FWM\)](#) and [phase matching \(PM\)](#).

2.1. Waveguide Modes and Dispersion

This section recaps the basics of waveguide modes and chromatic dispersion. We only consider *classical* waveguides and no others like photonic crystal (hollow core) fibers or structures which guide the wave with metallic surfaces. More specifically, we only deal with silica fibers and [SOI NR](#) waveguides. In these classical waveguides, light propagates in a core region surrounded by material with lower refractive index.

The main subject of this thesis is the optimization of [FWM](#) in *multimode* waveguides. As a rule of thumb, the larger the waveguide's core and the greater the refractive index difference, the more modes are guided by the waveguide. In order to optimize [FWM](#), light waves at different frequencies need to propagate with similar speeds in the waveguide – the optimization of which is called [phase matching](#). Since dispersion in the waveguide depends on frequency and is different among modes, both factors play key roles in [PM](#) and hence are introduced here.

2.1.1. Modeling the E-Field and Waveguide Modes

The propagation of light is at the core of optical communications. The classical (non-quantum) model of the propagation of light is based on Maxwell's equations

$$\nabla \cdot \tilde{\mathbf{D}} = \rho \quad (2.1)$$

$$\nabla \cdot \tilde{\mathbf{B}} = 0 \quad (2.2)$$

$$\nabla \times \tilde{\mathbf{E}} = -\frac{\partial \tilde{\mathbf{B}}}{\partial t} \quad (2.3)$$

$$\nabla \times \tilde{\mathbf{H}} = \frac{\partial \tilde{\mathbf{D}}}{\partial t} + \tilde{\mathbf{J}}, \quad (2.4)$$

which describe the interplay of electric and magnetic fields $\tilde{\mathbf{E}}$ and $\tilde{\mathbf{H}}$, electric displacement field (or flux density) $\tilde{\mathbf{D}}$, magnetic flux density $\tilde{\mathbf{B}}$, the free charge density ρ and the current density in a conducting material $\tilde{\mathbf{J}} = \sigma \tilde{\mathbf{E}}$ (with conductivity σ)². The material permittivity ε and permeability μ connect fields and flux densities via the constitutive relations³

$$\tilde{\mathbf{D}} = \varepsilon \tilde{\mathbf{E}} = \varepsilon_0 \varepsilon_r \tilde{\mathbf{E}} \quad (2.5)$$

$$\tilde{\mathbf{B}} = \mu \tilde{\mathbf{H}} = \mu_0 \mu_r \tilde{\mathbf{H}}, \quad (2.6)$$

where ε_r and μ_r are in general frequency and location dependent and ε_0 and μ_0 are the vacuum permittivity and permeability constants. These quantities are related to the speed of light in vacuum as

$$c_0 = \frac{1}{\sqrt{\varepsilon_0 \mu_0}} \quad (2.7)$$

and to the familiar refractive index n as

$$n = \sqrt{\varepsilon_r \mu_r}. \quad (2.8)$$

For the propagation of light in optical waveguides, we can further assume that:

- There are no free charges, hence $\rho = 0$ and $\sigma = 0$.
- We only consider non-magnetic materials, hence $\mu_r = 1$.
- The frequency dependence of ε is very slow compared to the fast oscillating light fields, hence $\frac{\partial \varepsilon}{\partial t} \approx 0$ for calculations with **continuous wave (CW)** (also called monochromatic) light waves.
- The waveguide is uniform in the propagation direction, hence $\frac{\partial \varepsilon}{\partial z} = 0$.

² The quantities in this section are passband signals, denoted by the tilde. See [Appendix A.1.2](#) for our notation of passband, analytic, baseband and complex phasor signals.

³ These relations are valid for a **linear** medium only. We extend $\tilde{\mathbf{D}}$ by the nonlinear material polarization in [Section 2.4](#) and [Chapter 4](#).

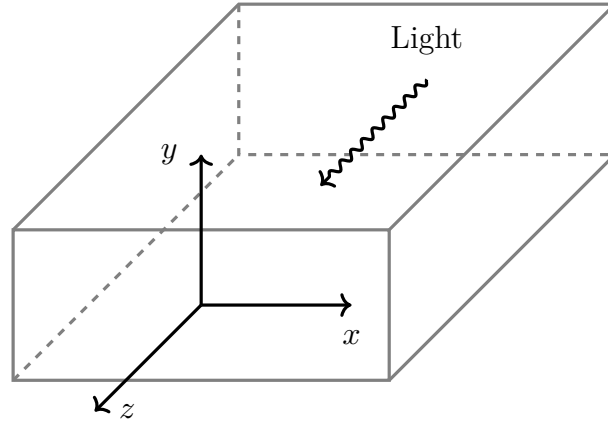


Figure 2.1.: The coordinate system used for light propagation throughout the thesis. The wave travels towards the observer in the $+z$ direction and its polarization is defined by the $\tilde{\mathbf{E}}$ field in the (x, y) plane.

Using the first three assumptions, we can simplify Eqs. (2.1) to (2.4) to

$$\nabla \cdot \tilde{\mathbf{D}} = \nabla \cdot (\varepsilon \tilde{\mathbf{E}}) = 0 \quad (2.9)$$

$$\nabla \cdot \tilde{\mathbf{B}} = \nabla \cdot (\mu \tilde{\mathbf{H}}) = 0 \quad (2.10)$$

$$\nabla \times \tilde{\mathbf{E}} = -\mu_0 \frac{\partial \tilde{\mathbf{H}}}{\partial t} \quad (2.11)$$

$$\nabla \times \tilde{\mathbf{H}} = \varepsilon \frac{\partial \tilde{\mathbf{E}}}{\partial t}. \quad (2.12)$$

Taking the curl of Eq. (2.11), using the generic vector field identity

$$\nabla \times (\nabla \times \tilde{\mathbf{E}}) = \nabla (\nabla \cdot \tilde{\mathbf{E}}) - \Delta \tilde{\mathbf{E}} \quad (2.13)$$

and inserting Eq. (2.12) yields the wave equation

$$\Delta \tilde{\mathbf{E}} - \nabla (\nabla \cdot \tilde{\mathbf{E}}) - \varepsilon \mu_0 \frac{\partial^2 \tilde{\mathbf{E}}}{\partial t^2} = 0, \quad (2.14)$$

which is a second order partial differential equation. Equation (2.14) is a full 3-dimensional model of the wave in space and time. However, for modeling the propagation of light in a waveguide, it is beneficial to split the transversal field distribution from the evolution along the propagation direction. See Fig. 2.1 for our definition of the coordinate system.

It is customary to model the $\widetilde{\mathbf{E}}$ field as⁴

$$\widetilde{\mathbf{E}}(x, y, z, t) = \mathcal{R}e\{\widehat{E}(z, t)\boldsymbol{\Psi}(x, y)e^{j\omega t}e^{-j\beta z}\}, \quad (2.15)$$

where $e^{j(\omega t - \beta z)}$ represents a plane wave at frequency ω and with propagation constant β , $\widehat{E}(z, t)$ is the slowly varying wave amplitude (potentially modulated with data) and $\boldsymbol{\Psi}(x, y)$ is the 3-dimensional transversal light profile. With $\widetilde{\mathbf{E}}$ defined as in Eq. (2.15), the solutions of Eq. (2.14) are called *modes* and each mode consists of a pair of $\boldsymbol{\Psi}$ and β .

A waveguide can support one or more *guided* modes, depending on its core size, the refractive index difference Δn between core and surrounding material, and the propagating light's wavelength λ . As a general rule, a larger core, a higher refractive index difference⁵ and a smaller wavelength increase the number of guided modes. All waveguides have at least one mode that is guided for all wavelengths of propagation light, called the *fundamental* mode. Every other mode has a specific *cutoff* wavelength, which means that it only guides waves with smaller wavelengths.

In symmetric waveguides, there exist two identical “copies” of each mode, just rotated by 90°. They are typically called *x* and *y* polarized. These copies are frequently regarded as two versions of one mode, although they are two distinct and independent solutions of Eq. (2.14)⁶. For instance, a standard single-mode fiber has a core diameter of about 8 μm and, as the name states, supports only one mode at typical telecommunications wavelengths in the C-band around 1550 nm. Since the fiber has circular symmetry, the fundamental mode has actually two versions called HE_{11e} and HE_{11o} . In contrast, plastic optical fibers have a core diameter of about 1 mm and support millions of modes. In between, there exist *few-mode fibers* (FMFs) and multi-mode fibers with core diameters around 20 μm and 50 μm , respectively. They support from some few up to hundreds of modes.

We define the set of all supported and considered modes of the waveguide as

$$\mathcal{M} = \{\text{TE}_0, \text{TE}_1, \text{TE}_2, \text{TE}_3, \dots\}. \quad (2.16)$$

Mode names depend on the waveguide, e.g. $\mathcal{M} = \{\text{LP}_{01x}, \text{LP}_{01y}, \text{LP}_{11ax}, \text{LP}_{11ay}, \dots\}$ for a fiber, etc. Their order is according to their propagation constants β in *decreasing* order, where the first is the fundamental mode.

⁴ The field in Eq. (2.15) is given as a decomposition into its analytic representation, converted back to the passband. See Appendix A.1.2 for our notation of passband, analytic, baseband and complex phasor signals.

⁵ The index difference can be exactly defined for some geometries where one material is uniformly surrounded by another material, e.g. $\Delta n = n_{\text{core}} - n_{\text{clad}}$ for a circular fiber. For more complicated geometries like, e.g., a NR waveguide with different materials surrounding a T-shaped core, it is not possible to define Δn exactly. However, the general trend mentioned in the text is still valid – increasing the refractive index difference by using a higher core index or a lower index in one of the surrounding regions, increases the number of guided modes.

⁶ For example, the modes (in the linear polarized (LP) approximation, see Section 2.3) of a *few-mode fiber* are usually labeled LP_{01} , LP_{11a} , LP_{11b} , etc. Each of these modes exists in two polarizations, e.g., LP_{01x} , LP_{01y} , LP_{11ax} and LP_{11ay} , etc.

We can then model the superposition of CW signals at discrete frequencies propagating in a waveguide in different modes and at different frequencies as

$$\begin{aligned} \sum_{a \in \mathcal{S}} \sum_{(m) \in \mathcal{M}} \tilde{\mathbf{E}}_a^{(m)}(z) &= \sum_{a \in \mathcal{S}} \sum_{(m) \in \mathcal{M}} \mathcal{R}e \left\{ \hat{E}_a^{(m)}(z) \Psi_a^{(m)}(x, y) e^{j(\omega_a t - \beta_a^{(m)} z)} \right\} \\ &= \frac{1}{2} \sum_{a \in \mathcal{S}} \sum_{(m) \in \mathcal{M}} \hat{E}_a^{(m)}(z) \Psi_a^{(m)}(x, y) e^{j(\omega_a t - \beta_a^{(m)} z)} + \text{c.c.} \end{aligned} \quad (2.17)$$

with the set of all considered positive frequencies \mathcal{S} , complex amplitudes $\hat{E}_a^{(m)}$ and plane waves $\exp(j(\omega_a t - \beta_a^{(m)} z))$. The variables a and (m) are to be interpreted as indices to the sets \mathcal{M} and \mathcal{S} , respectively, e.g. $\beta_a^{(m)}$ is the propagation constant of the (m) -th mode in \mathcal{M} , evaluated at the a -th frequency in \mathcal{S} and needs to be understood as $\beta^{(m)}(f_a)$. The transversal field profile Ψ has an implicit slow frequency dependence which is frequently ignored. However, we need to consider it when we perform integrals over mode fields and therefore state the dependence explicitly in Eq. (2.17).

Numerical methods are needed to compute modes of most waveguide geometries, while analytical methods exist for some special cases. Section 2.3 is devoted to the computation of modes and also contains figures for different waveguides.

2.1.2. Dispersion

Despite its name, the propagation “constant” $\beta(\omega)$ is actually frequency dependent and the cause for several effects. It is common to expand it into its Taylor series around some center frequency ω_0

$$\begin{aligned} \beta^{(m)}(\omega) &= \beta_0^{(m)} + \beta_1^{(m)} \Delta\omega + \frac{\beta_2^{(m)}}{2} \Delta\omega^2 + \dots + \frac{\beta_i^{(m)}}{i!} \Delta\omega^i + \dots, \\ \beta_i^{(m)} &= \left. \frac{d^i \beta^{(m)}(\omega)}{d\omega^i} \right|_{\omega=\omega_0} \end{aligned} \quad (2.18)$$

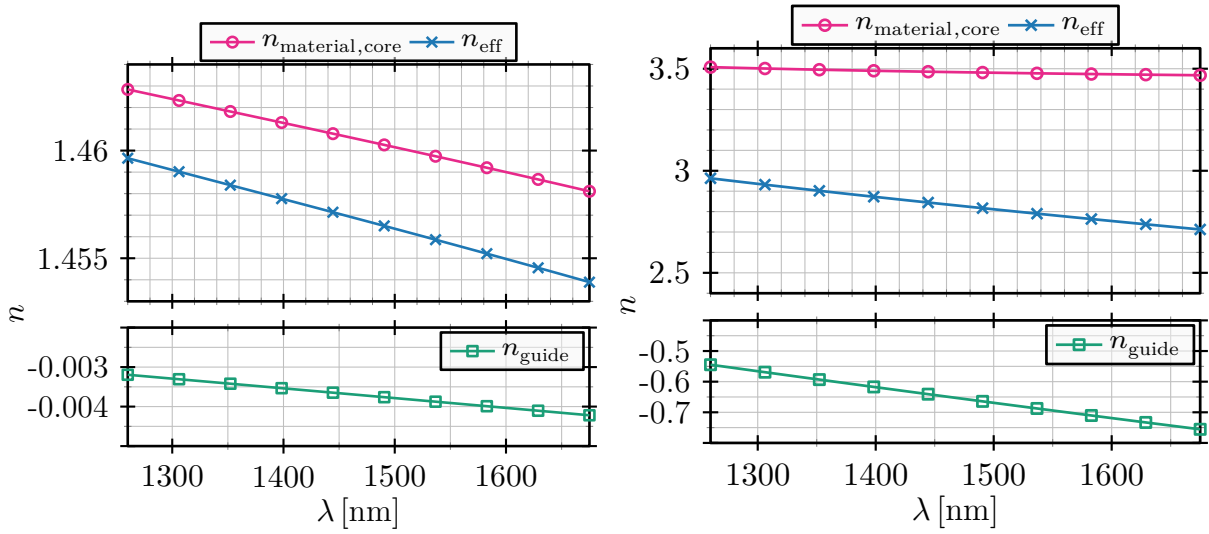
with $\Delta\omega = \omega - \omega_0$. The summands have different physical interpretations: β_0 is responsible for the propagation phase delay of the wave, β_1 for the linear group delay, β_2 for group velocity dispersion, β_3 for the dispersion slope and all higher terms are negligible for typical optical communication applications.

Normalized group delay and the dispersion parameter are defined by derivatives of β

$$\tau_g^{(m)}(\omega) = \frac{d\beta^{(m)}(\omega)}{d\omega} = \frac{d\beta^{(m)}(\lambda(\omega))}{d\lambda} \frac{d\lambda}{d\omega} \quad (2.19)$$

$$D^{(m)}(\lambda) = \frac{d\tau_g^{(m)}(\lambda)}{d\lambda} = \frac{d\tau_g^{(m)}(\omega(\lambda))}{d\omega} \frac{d\omega}{d\lambda} = \frac{d^2 \beta^{(m)}(\omega)}{d\omega^2} \frac{d\omega}{d\lambda}, \quad (2.20)$$

where $\frac{d\omega}{d\lambda} = -\frac{2\pi c_0}{\lambda^2}$ and $\frac{d\lambda}{d\omega} = -\frac{2\pi c_0}{\omega^2}$. Our figures mostly show *relative* normalized group delays $\bar{\tau}_g$, where the curves are vertically shifted by a common offset, such that the fastest plotted mode (with lowest normalized group delay) has a value of zero at 1550 nm.



(a) Dispersion of the HE_{11e} mode of FMF 2 (graded index) in Table 2.2. (b) Dispersion of the TE₀ mode of waveguide 1 (regular) in Table 2.3.

Figure 2.2.: Effective, material and waveguide dispersion (expressed as refractive indices) of the fundamental modes in a FMF and NR waveguide.

The *total* or *effective* chromatic dispersion Eq. (2.20) can be divided into

$$D = D_{\text{material}} + D_{\text{waveguide}}. \quad (2.21)$$

Material dispersion is caused by the frequency dependence of the waveguide material's refractive index itself. This part can be modeled with Sellmeier equations of the form Eq. (2.22) or Eq. (2.23). *Waveguide* dispersion is caused by the waveguiding effect, which in turn is determined by the transversal profile of the refractive index n (equivalently ε_r). Therefore, waveguide dispersion highly depends on the geometry of the waveguide and there is no obvious way to compute it apart from subtracting material from effective dispersion. Figure 2.2 shows an example of the three dispersion values for an FMF and a NR waveguide. The waveguide dispersion is strongly pronounced in the NR waveguide and almost negligible in the fiber.

The Sellmeier equation

$$n = \sqrt{1 + \sum_i \frac{A_i \lambda^2}{\lambda^2 - l_i^2}} \quad (2.22)$$

is a commonly used approximation for the wavelength dependent behavior of a material's refractive index. The Sellmeier-like equation

$$n = \sqrt{\varepsilon_{\text{inf}} + \frac{A}{\lambda^2} + \frac{Bl_1^2}{\lambda^2 - l_1^2}}, \quad (2.23)$$

is a simplification of Eq. (2.22), which is specifically used for silicon [42]. Table 2.1 lists coefficients to be inserted in Eq. (2.22) or Eq. (2.23) for all materials used in this thesis.

Table 2.1.: Sellmeier (-like) coefficients of different materials, to be inserted in Eqs. (2.22) and (2.23).

Material & References	A_1 & l_1 [μm]	A_2 & l_2 [μm]	A_3 & l_3 [μm]
SiO ₂ [43]	0.696 166 3	0.407 942 6	0.897 479 4
	0.068 404 3	0.116 241 4	9.896 161
GeO ₂ [43]	0.806 866 42	0.718 158 48	0.854 168 31
	0.068 972 606	0.153 966 05	11.841 931
99%SiO ₂ , 1%F [44], [45]	0.693 25	0.397 20	0.860 08
	0.067 24	0.117 14	9.7761
Si ₃ N ₄ [46]	3.0249	40 314	
	0.135 340 6	1239.842	
Material & References	ϵ_{inf}	A [μm^2]	B & l_1 [μm]
Si [47, p. 548], [42]	11.6858	0.939 816	$8.104 61 \cdot 10^{-3}$ 1.1071

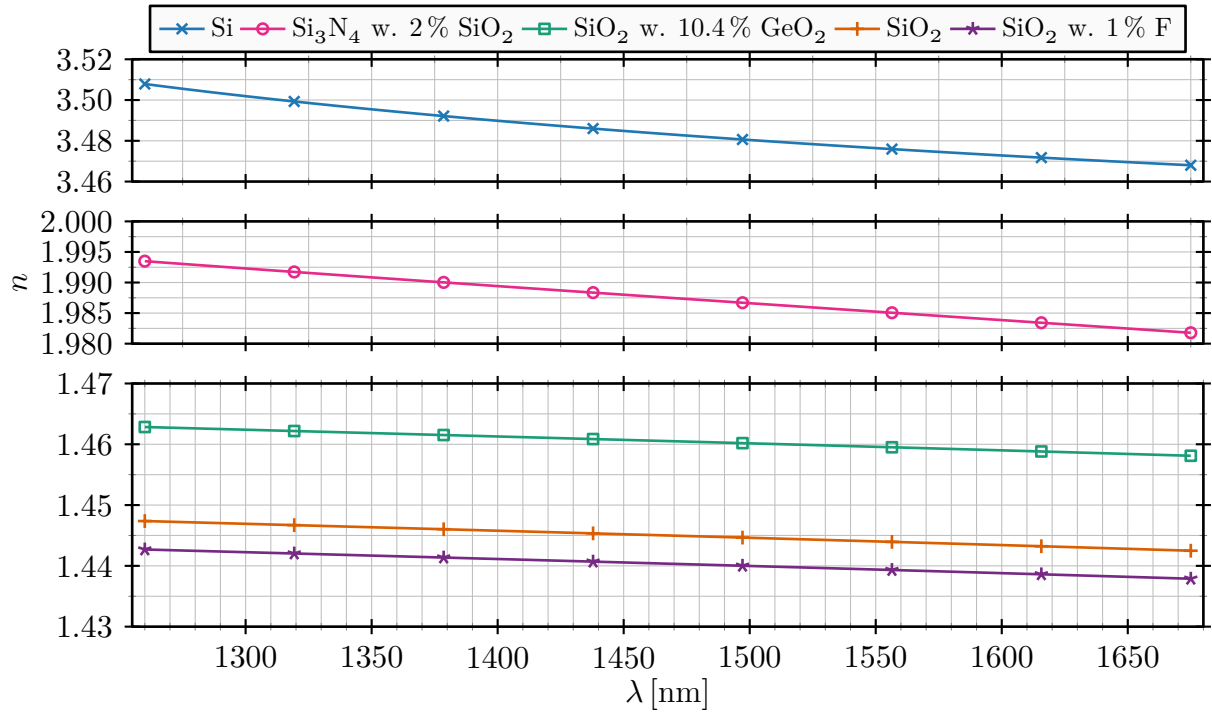


Figure 2.3.: Wavelength dependent refractive index of crystalline silicon, silicon nitride doped with 2% silica, pure silica and silica doped with germanium and fluorine.

Figure 2.3 shows the refractive indices of materials and composite materials used in the thesis. The procedures to compute refractive indices of composite materials differ. For $\text{SiO}_2 + \text{F}$, we use coefficients from direct measurements of the composite material [44], [45]. For $\text{SiO}_2 + \text{GeO}_2$, we can linearly combine the Sellmeier coefficients of the two component materials [43]

$$\begin{aligned}
 A_{i,\text{SiO}_2+\text{GeO}_2} &= (1 - X)A_{i,\text{SiO}_2} + (X)A_{i,\text{GeO}_2} \\
 l_{i,\text{SiO}_2+\text{GeO}_2} &= (1 - X)l_{i,\text{SiO}_2} + (X)l_{i,\text{GeO}_2} \\
 n_{\text{SiO}_2+\text{GeO}_2} &= \sqrt{1 + \sum_i \frac{A_{i,\text{SiO}_2+\text{GeO}_2} \lambda^2}{\lambda^2 - l_{i,\text{SiO}_2+\text{GeO}_2}^2}}
 \end{aligned} \tag{2.24}$$

where X is the fraction of GeO_2 . Finally, for $\text{SiO}_2 + \text{Si}_3\text{N}_4$ we can linearly combine the refractive indices of the component materials [48]

$$n_{\text{SiO}_2+\text{Si}_3\text{N}_4} = (1 - X)n_{\text{SiO}_2} + (X)n_{\text{Si}_3\text{N}_4} \tag{2.25}$$

where X is the fraction of Si_3N_4 .

Table 2.2.: Parameters of **FMFs** used in the thesis. X_{GeO_2} and X_{F} are the percentage of GeO_2 in the core and F in the trench, respectively.

Waveguide	r_{core} [μm]	w_{trench} [μm]	r_{clad} [μm]	γ_{grad}	X_{GeO_2} [%]	X_{F} [%]
1 (step index)	10	0	30	∞	10.4	
2 (graded index)	10	0	30	1.82	10.4	
3 (depressed cladding)	10	10	30	1.82	10.4	1
4 (large core)	40	0	60	1.82	10.4	
5 (example)	20	20	60	1.82	10.4	1

Table 2.3.: Parameters of **NR** waveguides used in the thesis.

Waveguide	w_{rib} [nm]	h_{slab} [nm]	h_{SOI} [nm]	Num. Dips	w_{dip} [nm]	h_{dip} [nm]	$\alpha_{\text{tilt},l}$ [$^\circ$]	$\alpha_{\text{tilt},r}$ [$^\circ$]	w_{lower} [nm]	n_{lower}
1 (regular)	2000	100	200							
2 (dips)	2000	100	200	2	200	50				
3 (tilted rib walls)	2000	100	200				30	30		
4 (lower rib sides)	2000	100	200						200	3.181
5 (zero dispersion)	1947	80	220							
6 (PM fails)	1210	70	220							
7 (third kind PM)	2000	70	220	2	200	150				

2.2. Examples of Light Waveguides

In this section, we introduce the two waveguide types used throughout this thesis – silica fibers and **SOI NR** waveguides. In fibers, the core is surrounded by a *cladding* and the difference in refractive indices is very small – typically $n_{\text{clad}} = 1.44$ and $n_{\text{core}} = 1.46$. In **NR** waveguides, light propagates in the slab and rib regions, which are surrounded by a silica *substrate* and several *coating* layers with both much lower refractive indices than the core – typically $n_{\text{rib}} = 3.48$ and $n_{\text{substrate}} = 1.444$. The sum height of rib and slab is around 200 nm, hence the name “nano”.

We present transversal refractive index profiles, mode fields and dispersion curves for selected examples of both waveguide types. For this purpose, it is enough to know the refractive index profile and no further waveguide properties like nonlinearity are needed (nonlinear effects are introduced in [Section 2.4](#) and [Chapter 4](#)).

We collect waveguide parameters like dimensions, doping fractions and grading exponents for all waveguides used across this thesis in [Tables 2.2](#) and [2.3](#).

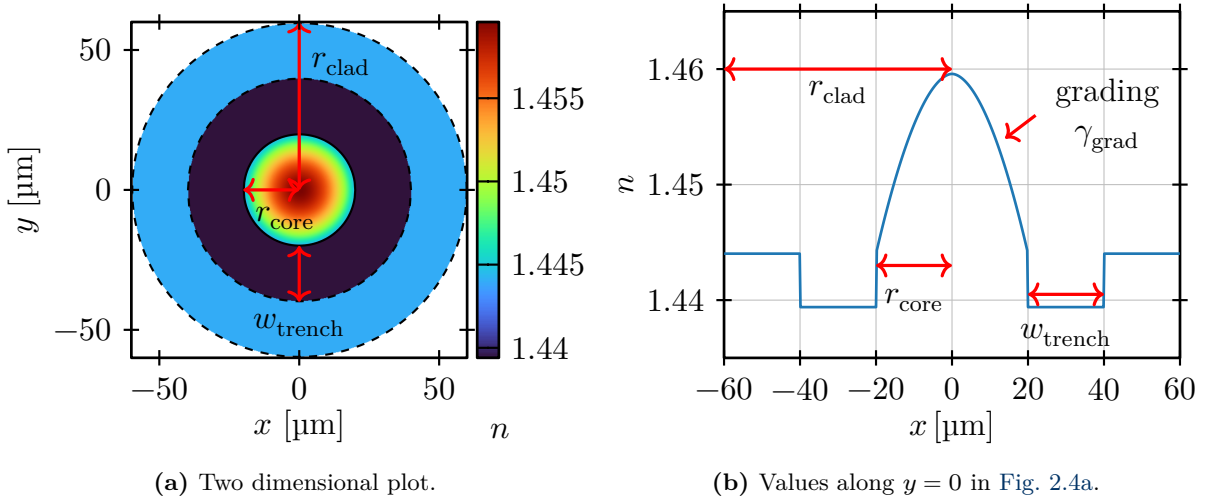


Figure 2.4.: Refractive index profile of a graded index, depressed cladding FMF. Parameters are the core radius, cladding radius, trench width and grading index, the values in this example are taken from FMF 5 (example) in Table 2.2.

2.2.1. Silica Fibers

Figure 2.4 shows our definition of dimensions for graded index depressed cladding few-mode fibers. They consist of a cladding, a trench with lower refractive index and a core with higher refractive index.

While the cladding consists of pure SiO_2 , core and trench are doped with GeO_2 and F, respectively (see Tables 2.1 and 2.2 and Fig. 2.3). The resulting refractive indices are wavelength dependent and can be calculated with the help of Eq. (2.22).

The concentration of GeO_2 in the core has a graded profile and the refractive index can be computed as

$$n = \sqrt{n_{\text{core}}^2 - (n_{\text{core}}^2 - n_{\text{clad}}^2) \left(\frac{r}{r_{\text{core}}} \right)^{\gamma_{\text{grad}}}}, \quad (2.26)$$

where n_{core} is the index in the center of the core, r the distance from the center and γ_{grad} the grading exponent (typically close to 2 or infinity for step index fibers).

Depressed cladding fibers have a trench around the core with a refractive index lower than in the cladding.

Figure 2.5 shows the four selected mode fields (starting with the fundamental one) of FMF 2 (graded index) in Table 2.2. The figure shows “vectorial” mode fields, which are the physical modes of the waveguide. While some of them are approximately linearly polarized in x or y direction (HE_{11} and HE_{12} in Fig. 2.5), others have complex polarization profiles (TE_{01} and EH_{110} in Fig. 2.5). In the latter cases, the $\tilde{\mathbf{E}}$ -fields point in arbitrary directions in the x, y, z plane (with usually negligible z component). Vector modes can be combined to yield approximately linear polarized (LP) modes, see Section 2.3.3 and Appendix A.4.2. Mode fields of the step index fiber (FMF 1 (step index) in Table 2.2) are very similar to those in Fig. 2.5, except that the grading “squeezes” the modes and they are smaller compared to the step index fiber.

The depressed cladding graded index fiber (FMF 3 (depressed cladding) in Table 2.2) has almost the same mode fields as without the trench, except that slightly less power is guided outside of the fiber’s core due to the higher index contrast.

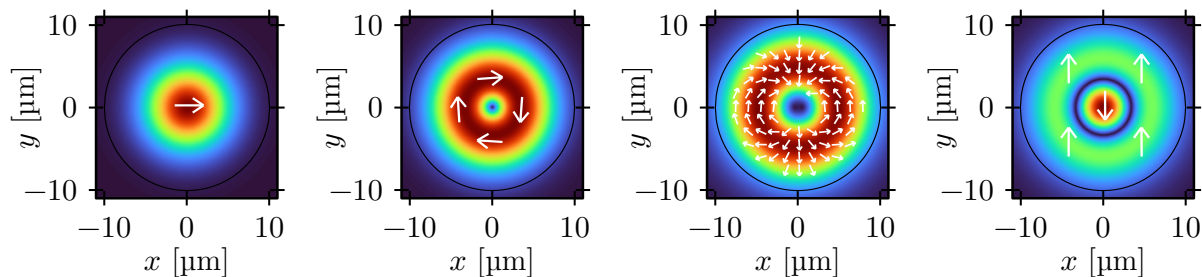


Figure 2.5.: Transversal electric field distributions of the four modes HE_{11e} , TE_{01} , EH_{11o} and HE_{12o} of FMF 2 (graded index) in Table 2.2. Colors encode magnitudes (high values are red and low values are blue) and arrows encode polarization directions.

Finally, Fig. 2.6 shows relative normalized group delays and dispersions of the same four modes that are shown in Fig. 2.5 – for a step index, graded index, depressed cladding graded index fiber and a fiber with very large core. By comparing Figs. 2.6a, 2.6c and 2.6e, one can clearly see that differential mode delay (DMD) is reduced by adding a grading and even further by adding a trench. Although the DMD in the fiber with large core is even lower, it's not possible to exploit it. We have to keep in mind that this fiber supports a vast number of guided modes and the DMD of all its guided modes is much larger than that of the four depicted modes.

Depressed cladding fibers have traditionally been used to minimize dispersion in single-mode fibers by shifting the zero dispersion wavelength [49]. However, they are also beneficial to reduce DMD and to equalize dispersion slopes among modes⁷ [50], [51]. For example, the dispersion slopes in Fig. 2.6f are almost equal among the modes, in contrast to Fig. 2.6d.

⁷ We briefly show in Section 3.1.2 how similar dispersion helps with FWM.

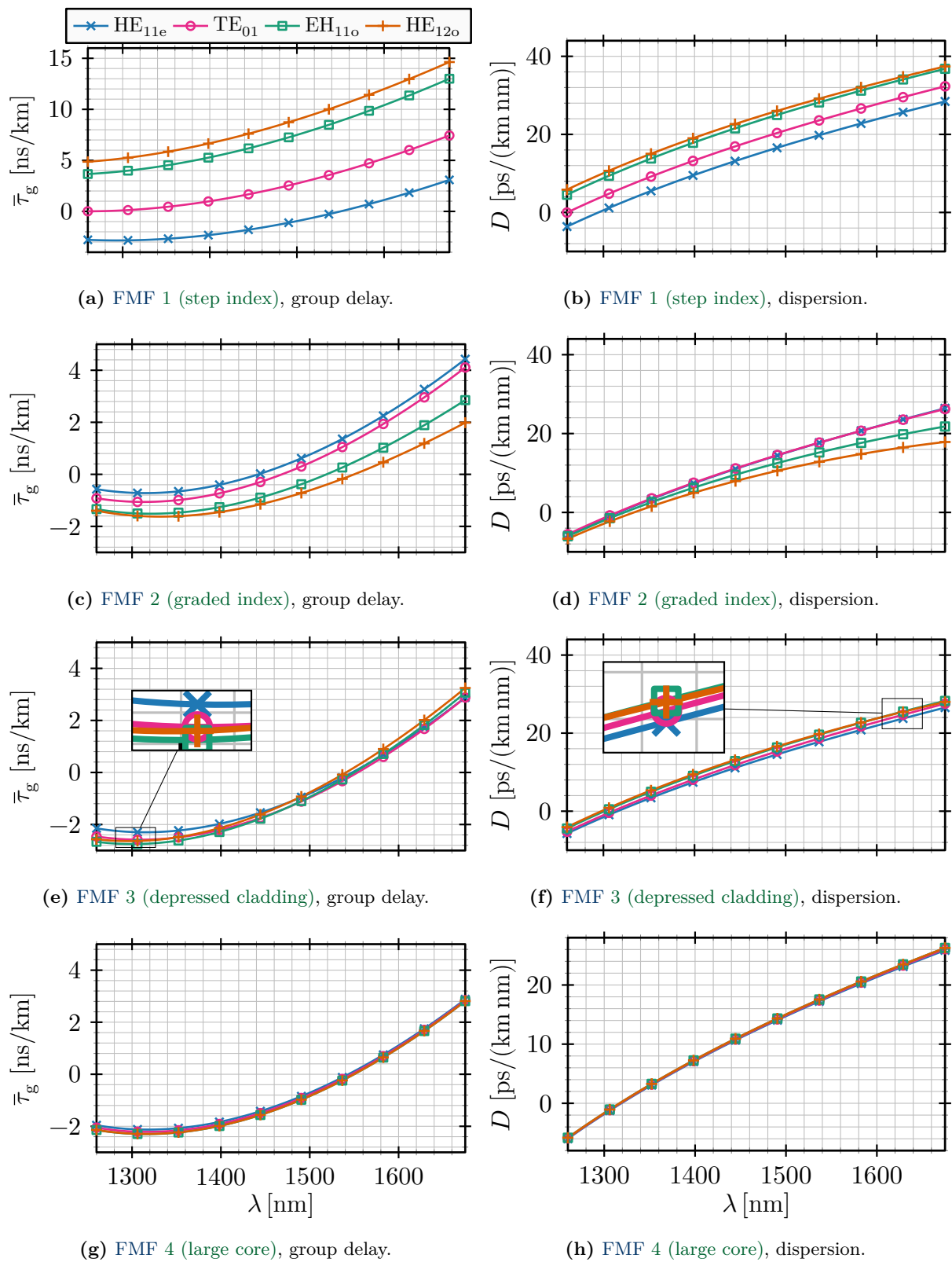


Figure 2.6.: Normalized relative group delay and dispersion of four selected modes of FMMs 1 (step index), 2 (graded index), 3 (depressed cladding) and 4 (large core) in Table 2.2. The legend at the top is valid for all plots.

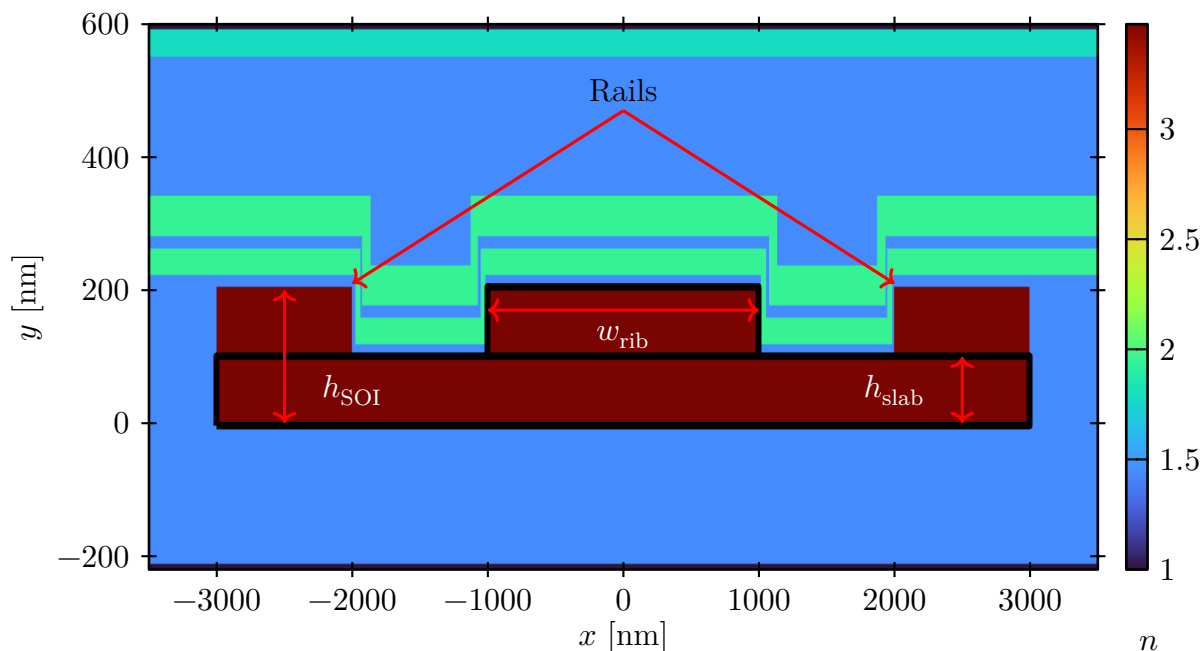


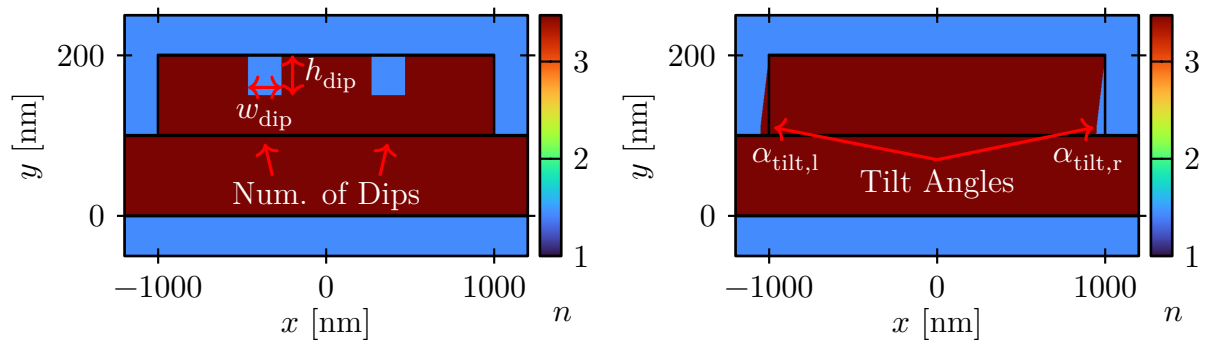
Figure 2.7.: Refractive index profile of NR waveguide 1 (regular) in Table 2.3, with layer stack and rails. Note that the axes are scaled differently and the waveguide appears to be taller than it is.

2.2.2. Silicon on Insulator Nano-Rib Waveguides

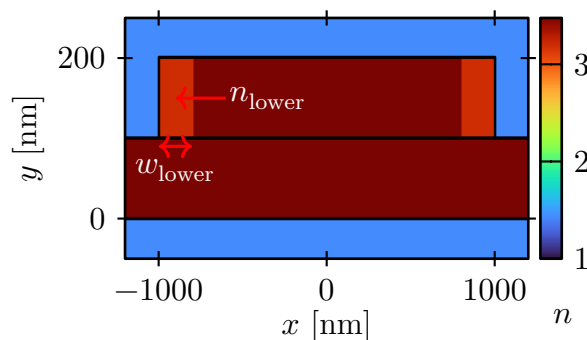
Definitions of our NR waveguide parameters are shown in Fig. 2.7. The core is made of the silicon parts *slab*, *rib* and *rails* and is surrounded by the silica substrate and coating⁸. During manufacturing, silicon nitride and silica protective layers are added above the core. We show these layers only once in Fig. 2.7 and don't mention them again, although they are used in all simulation results later in the thesis⁹. The rails on the left and right of the slab are used to apply a reverse voltage to reduce free carriers and therefore attenuation [20]. Since the voltage does not affect neither dispersion nor nonlinearity and the rails are far enough from the rib that they also don't affect dispersion or mode fields, we don't include rails in our simulations.

⁸ Sellmeier coefficients for all used materials are listed in Table 2.1 and plotted in Fig. 2.3. Note that in contrast to fibers, we don't list material doping fractions in Table 2.3. The NR waveguide consists of pure silicon and silica, except for the silicon nitride protective layers which are fixed by the manufacturing process (that we can't influence) and their effect is marginal anyways.

⁹ Note that the thickness and refractive index values of the protective layers are slightly randomized. The exact values are subject to a non-disclosure agreement with the manufacturing partner we were collaborating with, because they would reveal confidential information about the etching process. We performed our simulations with the exact values, but if we used the randomized ones instead, the effect on results would be negligible.



(a) “Dips” etched into the rib, dimensions like waveguide 2 (dips) in Table 2.3. (b) Tilted rib side walls, dimensions like waveguide 3 (tilted rib walls) in Table 2.3.



(c) Rib sidewalls with lowered refractive index, dimensions like waveguide 4 (lower rib sides) in Table 2.3.

Figure 2.8.: Variants of the NR waveguide with tunable parameters: Number, width and height (etching depth) of dips, angles of the wall tilts (positive and negative angles possible), and width and refractive index of rib sides with lowered refractive index.

Fig. 2.8 shows further waveguide parameters we defined and used in some simulations. For example, Fig. 2.8a shows *dips* we can etch into the waveguide to alter the dispersion for FWM optimization. As parameters, we can choose the number of dips, their width and depth¹⁰. Furthermore, we tested hypotheses about manufacturing errors in Chapter 6. There, we needed the extra geometry parameters like tilted rib walls (Fig. 2.8b).

Figures 2.9 and 2.10 show the four lowest order modes of waveguides 1 (regular) and 2 (dips) in Table 2.3, respectively. All modes are approximately linear polarized and are usually called TE_0 , TE_1 , TE_2 and TE_3 (meaning “Transversal Electric” with zero, one, two and three polarity inversions). The first two resemble LP_{01} and LP_{11} of a FMF – except for the smaller size and much narrower vertical than horizontal dimension. The higher order modes don’t have equivalents in fibers, but they are also approximately linearly polarized. We don’t show mode field plots for waveguides with tilted rib walls and lowered rib side refractive indices, since there is almost no visual difference to Fig. 2.9.

¹⁰ Since SOI waveguides are manufactured by an etching process, we have to obey some rules. For example, it is not possible to have too narrow structures in the x dimension and only discrete etching depths are possible. Both limitations can be mitigated, albeit at increased costs (more etching steps, better etching process, etc.). Therefore, we ignore these limitations in some proof-of-concept simulations.

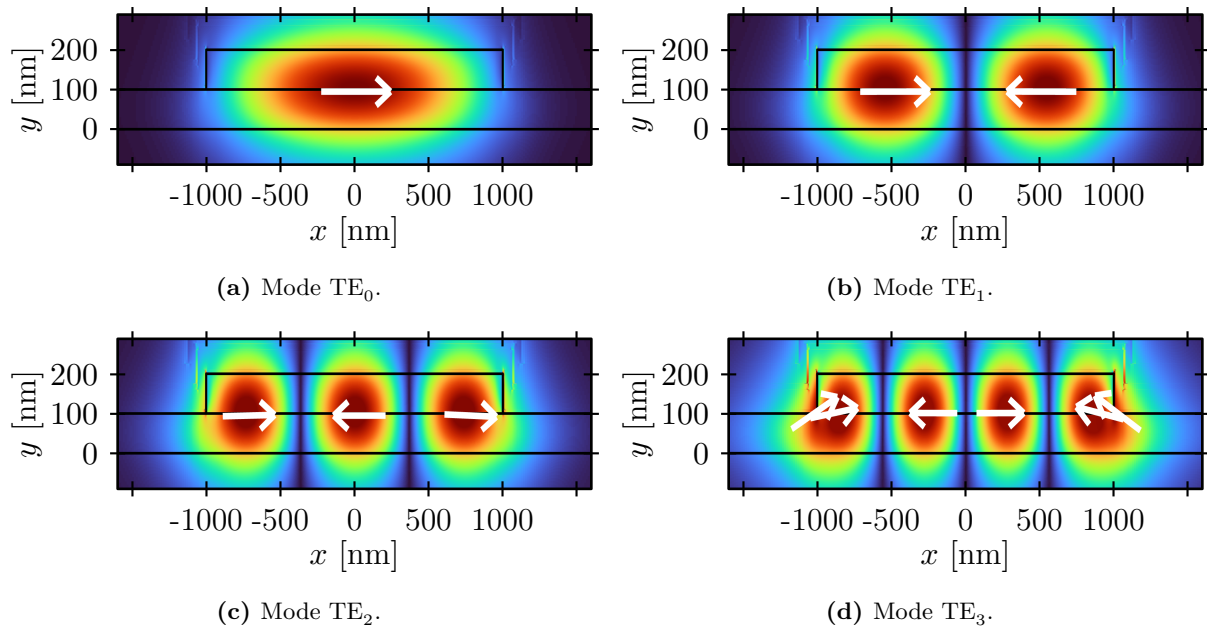


Figure 2.9.: Transversal electric field distributions of the four lowest order modes TE_0 , TE_1 , TE_2 and TE_3 of waveguide 1 (regular) in Table 2.3. Colors encode magnitudes (high values are red and low values are blue) and arrows polarization directions.

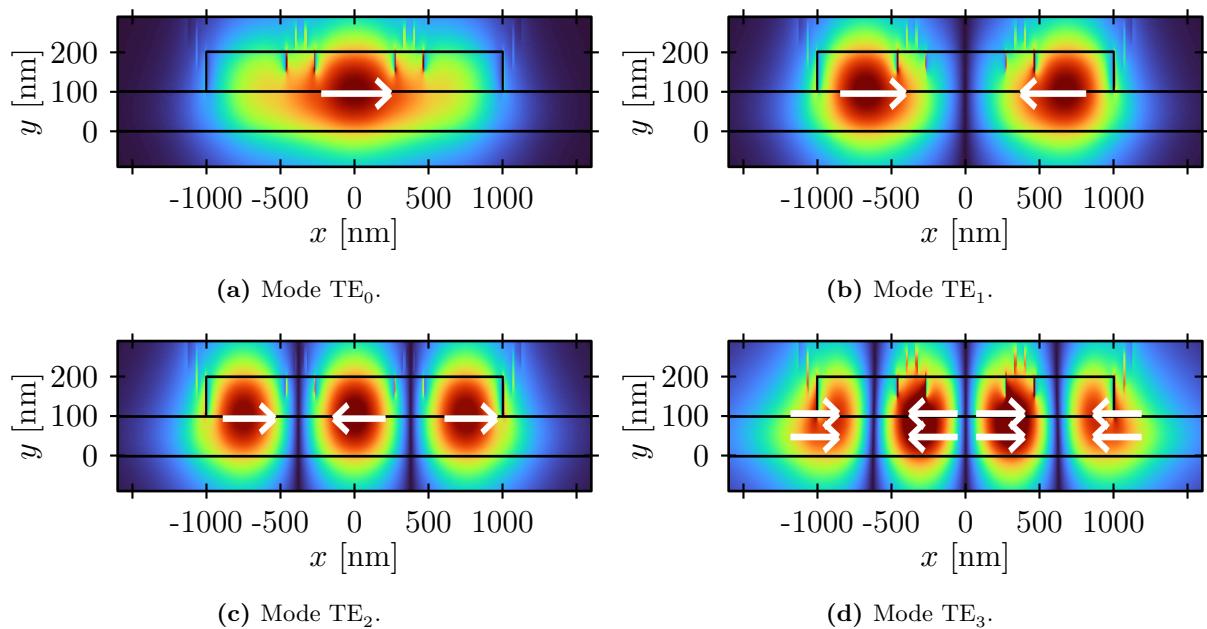


Figure 2.10.: Transversal electric field distributions of the four lowest order modes TE_0 , TE_1 , TE_2 and TE_3 of waveguide 2 (dips) in Table 2.3 which has two dips. Colors encode magnitudes (high values are red and low values are blue) and arrows polarization directions.

The most important parameters of NR waveguides are w_{rib} and h_{SOI} . Since most of the light power propagates in the rib and slab region below it (see e.g. Fig. 2.9a), the rib width and SOI height determine the core's size similar to r_{core} in fibers. The larger these values, the better the guiding and the higher the number of guided modes. When the light wavelength approaches a mode's cutoff wavelength, increasing fractions of the power propagate in the slab sides, i.e., the mode field gets larger (see e.g. the lower part of the outer lobes in Fig. 2.9d and especially Fig. 2.10d). Hence, the slab height also has an impact on dispersion and mode confinement.

Imagine slab height in Fig. 2.9d is slowly increased. More and more of the power left and right outside of the rib will also propagate in silicon and the mode's dispersion shifts closer to lower order modes (which propagate almost only in silicon). As a consequence, the dispersion of modes close to cutoff will deviate more from the lower order modes in waveguides with low slabs. This can lead to a very broad zero dispersion region useful for FWM (see e.g. TE_3 in Fig. 2.11f, Section 3.1.3 and Chapter 7).

Finally, Fig. 2.11 shows group delay and dispersion of waveguides 1 (regular), 2 (dips), 5 (zero dispersion) and 6 (PM fails) in Table 2.3. When comparing e.g. Figs. 2.6b and 2.11b, one can see that NR waveguides have orders of magnitude larger dispersion and also the wavelength dependent behavior is quite different from fibers – leading to substantially different FWM behavior.

Etching dips into the rib mostly affects modes that have significant power at the dip positions. For example, the mode fields in Fig. 2.10 show that TE_3 is severely affected, while TE_2 hardly is. Dips have a similar effect as lowering the slab or shrinking the core, except that they act on certain modes only. For example, the effect on mode TE_3 is clearly visible in Fig. 2.11d (compared to Fig. 2.11b), while TE_2 almost does not change. Therefore, adding dips can be beneficial for fine-tuning waveguide dispersion for PM.

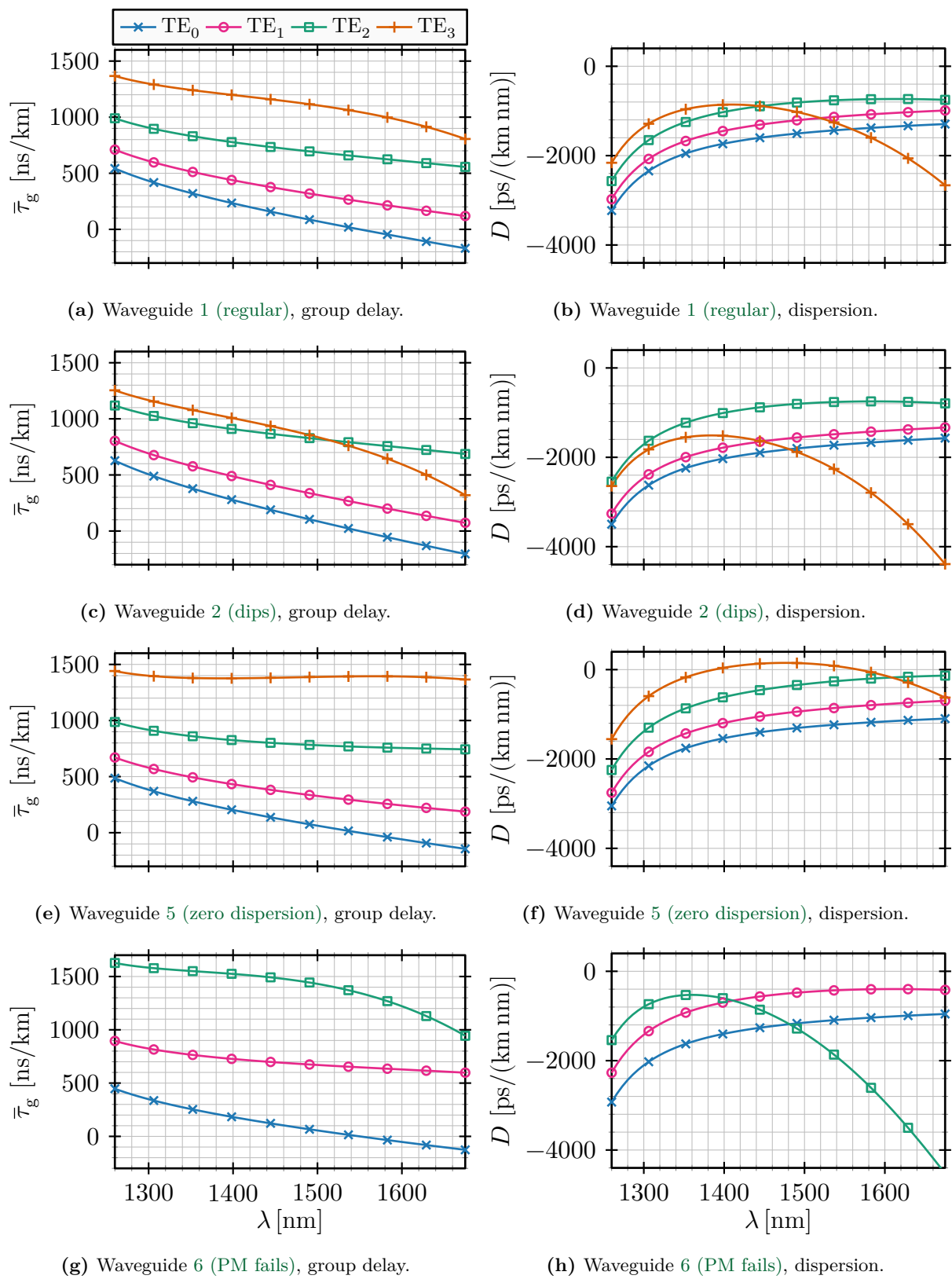


Figure 2.11.: Normalized relative group delay and dispersion of the four lowest order modes in NR waveguides 1 (regular), 2 (dips), 5 (zero dispersion) and 6 (PM fails) in Table 2.3. The legend at the top is valid for all plots.

2.3. Computing Waveguide Modes

In this section, we introduce different methods for computing transversal mode fields $\Psi^{(X)}(x, y)$ and their associated propagation constants β . The amplitude $\hat{E}(z, t)$ of a fully characterized wave as in Eq. (2.15) is excluded from computing mode fields, i.e., the mode field is determined except for a multiplication factor. Apart from this factor, modes are fully determined by the transversal relative permittivity $\varepsilon_r(x, y)$ of the waveguide and the frequency we evaluate the modes at.

All mode solving methods start from the wave Eq. (2.14) without nonlinearity. Later in Section 2.4 we introduce the nonlinear material polarization (see Eqs. (2.42) and (2.43)). Throughout the whole thesis, it is assumed that propagating wave amplitudes are small enough, such that nonlinearity does not influence the modal profiles. This assumption is justified for our applications in communications, but might fail for high intensity laser physics, where effects like self-focusing start to emerge.

Since modes are always computed at one fixed frequency, we don't explicitly include frequency dependence in the nomenclature of Ψ , β and ε_r in this chapter. To get the frequency dependent behavior as in Figs. 2.6 and 2.11, one needs to repeat the computation of modes over a sweep of frequencies. This also affects the wavelengths in the Sellmeier equations Eqs. (2.22) and (2.23).

For a limited set of waveguide geometries, Eq. (2.14) has analytic solutions. For a further number of geometries, there exist approximative methods. However, modes have to be computed with numerical methods in the general case.

2.3.1. Analytical Methods

The geometries with known analytic solutions include circular step index and graded index fibers, elliptical fibers and strip waveguides. In-detail derivation of mode fields and propagation constants of the above mentioned waveguides can be found in [52, Chapter 12]. Alternatively, derivations for circular fibers are also found in [53, Chapter 2.4] and [54, Chapter 2.2].

As an example, we summarize the solution for circular fibers in the weakly guiding approximation (valid if the refractive index difference between core and cladding is small, which is true for typical optical fibers). The \mathbf{E} and \mathbf{H} fields of a propagating wave have 6 components ($E_x, E_y, E_z, H_x, H_y, H_z$), out of which only two are independent due to the four Maxwell equations the fields have to fulfill¹¹. Usually E_z and H_z are computed and the other components are derived from these two. The E_z component is modeled in a separable form and in cylindrical coordinates (the procedure for H_z is similar) [54, Chapter 2.2]

$$E_z(r, \phi, z, \omega) = A(\omega)F(r)e^{jm\phi}e^{-j\beta z}. \quad (2.27)$$

In this equation, the field is in frequency domain and $A(\omega)$ contains the time and frequency dependence.

A solution of Eq. (2.14) can be obtained, if Eq. (2.27) it is inserted and cylindrical coordinates are used. The radial behavior of light intensity $F(r)$ is oscillatory in the core and is modeled by Bessel functions of the first kind $J_i(r)$ (i being the radial mode index). In the cladding, the fields decay quickly, which is modeled by modified Bessel functions of the second kind $K_i(r)$. The azimuthal behavior $e^{jm\phi}$ is also oscillatory, with azimuthal mode index m . Connecting continuous

¹¹ We use the analytic form of fields in this chapter, see Appendix A.1.2.

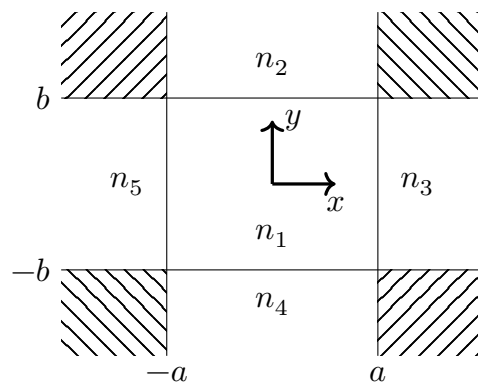


Figure 2.12.: Refractive index regions of a buried rectangular waveguide, defined in Marcatili's approximation.

field components at the core-cladding boundary yields an eigenvalue equation, solutions of which are the propagation constants. Since the resulting equation is transcendental, it has to be solved by a numerical or graphical method. Nevertheless, this method is regarded as analytical since the only numerical computation is solving one equation (with e.g. Newton's method). The demand on computational power is very low, especially if compared to numerical linear algebra based methods like presented in Section 2.3.3.

2.3.2. An Approximate Method by Marcatili

A famous example of an approximative solution is Marcatili's method for a buried optical waveguide [55] (also described in detail in [53, Chapter 2.3]). The main idea is to divide the refractive index profile into the five zones shown in Fig. 2.12.

Marcatili introduced the approximation that fields vanish in the hatched corner regions. This way, the continuity conditions reduce to the direct borders between n_1 and the four regions n_2 to n_5 , permitting an analytical solution. With this approximation, the fields have a doubly-cosine like behavior $\cos(k_x x + \alpha_1) \cos(k_y y + \alpha_2)$ in the central region n_1 ¹². In the outer regions, the fields decay exponentially with distance from region 1 and oscillate in the direction parallel to the core. For example, the fields in region 2 are proportional to $\cos(k_x x + \alpha_1) \exp(-\gamma_y(y - b))$, where γ_y is a decay constant¹³. Connecting fields at the region borders leads to the characteristic equation, which can be used to determine the values for the constants $k_{\{x,y\}}$, $\alpha_{\{1,2\}}$ and $\gamma_{\{x,y\}}$. Finally, β is computed as $\beta^2 = k_0^2 n_1^2 - k_x^2 - k_y^2$.

Marcatili's method also requires to solve the transcendental characteristic equation, which also needs numerical or graphical computations. Nevertheless, the computations are again much faster compared to numerical methods and can give good estimates of mode fields in this kind of waveguides – almost instantaneously on modern computers.

¹² The constants α should not be confused with waveguide attenuation α introduced in Section 2.4.1.

¹³ The constants γ should not be confused with the nonlinearity parameter γ introduced in Section 2.4.7.

2.3.3. Numerical Finite Difference Methods

The analytical and approximative methods are limited to a small set of fixed waveguide geometries. To lift this restriction and be able to compute modes and propagation constants of arbitrary waveguide profiles, numerical methods need to be used. Since our main goal was to optimize the geometry of NR waveguides, we clearly needed this flexibility. Hence, all our results were computed with solvers based on [finite-difference methods \(FDMs\)](#)¹⁴.

The general idea of FDM is to discretize the waveguide cross section into a *grid* and approximate all differential operators in [Eq. \(2.14\)](#) by truncated Taylor expansions of the fields on the grid points. The discrete field points can be reorganized into a matrix eigenvalue equation where eigenvectors are the mode fields and eigenvalues the associated propagation constants. FDM also makes use of the fact that only two out of the 6 field components have to be solved and the others can be derived from those two. The precision only depends on the grid point density, which directly translates into computation time and memory demand. One convenient property is, that already small grid sizes of 100×100 points are sufficient to get a first estimate of mode fields and propagation constants and thus dispersion properties. Computing 12 modes with such a small grid only takes less than a second on recent hardware and therefore exploring dispersion for changing geometries can be performed very quickly. However, larger grids need to be used to obtain reliable and resilient data without artifacts (see [Appendix A.4.3](#) for grid size optimizations).

In this section, we present two FDM solvers. The first solver is semi-vectorial and based on [\[53, Chapter 4\]](#). It computes modes in the LP approximation, which means that each mode has two nonzero components – either E_x and H_y (TE_n modes), or E_y and H_x (TM_n modes). The second solver is based on [\[56\]](#) and computes the physical waveguide modes which are *hybrid* in a sense that all components of the \mathbf{E} and \mathbf{H} fields are nonzero.

Both solvers need the same input:

- The frequency to compute modes at.
- The number of modes to compute.
- The discretization grid.
- The waveguide's refractive index profile $n(x, y)$, sampled at the discretization grid's points and valid for the frequency above.

With this information, both solvers compute the requested number of modes and return their transversal field components $\Psi^{(X)}(x, y)$ and $\beta^{(X)}$ – valid for the requested frequency.

In [Appendix A.4](#), we collected some implementation details and issues which concern both types of solvers.

¹⁴ It should be mentioned that there also exist [finite-element methods \(FEMs\)](#). Both methods – FDM and FEM – are widely used to compute waveguide modes. In this work, we exclusively used FDM.

2.3.3.1. The Semi-Vectorial Linear Polarized FDM Solver

Starting with the analytic signal form of the E-field from Eq. (2.15) with constant amplitude

$$\mathbf{E}(x, y, z, t) = \hat{E}\Psi(x, y)e^{j\omega t}e^{-j\beta z}, \quad (2.28)$$

the wave Eq. (2.14) becomes

$$\Delta\mathbf{E} - \nabla(\nabla \cdot \mathbf{E}) - k_0^2\varepsilon_r\mathbf{E} = 0, \quad (2.29)$$

where $k_0^2 = \omega^2\varepsilon_0\mu_0$. With using

$$\begin{aligned} \nabla \cdot \mathbf{D} = 0 &= \nabla \cdot (\varepsilon\mathbf{E}) = \varepsilon_0\nabla(\varepsilon_r) \cdot \mathbf{E} + \varepsilon_0\varepsilon_r\nabla \cdot \mathbf{E} \\ \Rightarrow \nabla \cdot \mathbf{E} &= -\frac{\nabla\varepsilon_r}{\varepsilon_r} \cdot \mathbf{E}, \end{aligned} \quad (2.30)$$

we get

$$\Delta\mathbf{E} + \nabla\left(\frac{\nabla\varepsilon_r}{\varepsilon_r} \cdot \mathbf{E}\right) + k_0^2\varepsilon_r\mathbf{E} = 0. \quad (2.31)$$

With the Laplace operator split into transversal and longitudinal components

$$\Delta = \Delta_t + \partial_z^2, \quad (2.32)$$

we get

$$\Delta_t\mathbf{E} + \nabla\left(\frac{\nabla\varepsilon_r}{\varepsilon_r} \cdot \mathbf{E}\right) + k_0^2\varepsilon_r\mathbf{E} = \beta^2\mathbf{E}. \quad (2.33)$$

This is an operator eigenvector/eigenvalue equation of the form $\mathcal{OP}\{\mathbf{E}\} = \mathbf{E}\mathbf{V} \cdot \mathbf{E}$. Its multitude of solutions are the sought mode fields $\Psi^{(X)}(x, y)$ and propagation constants $\beta^{(X)}$ which generate the set \mathcal{M} defined in Eq. (2.16).

After several algebraic manipulations (see [53, Chapter 4]), the wave equation

$$\partial_x^2 E_x + \partial_y^2 E_x + \partial_x\left(\frac{1}{\varepsilon_r}\frac{\partial\varepsilon_r}{\partial x}E_x\right) = (\beta^2 - k_0^2\varepsilon_r)E_x \quad (2.34)$$

is obtained. In the process, several approximations were used. Firstly, $\frac{\partial\varepsilon}{\partial z} = 0$, i.e., the refractive index is constant in the propagation direction. This is a valid assumption, since computing modes does not consider any effects which disturb the propagation along the waveguide like linear or nonlinear mode coupling. Secondly, $\mathbf{E} = E_x\mathbf{e}_x$, i.e., the E-field is linear polarized in x direction. This is a linear polarized method, hence this assumption.

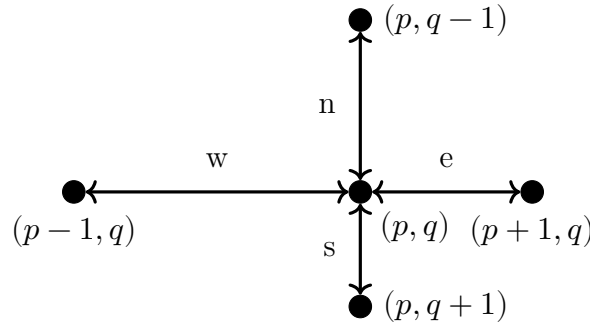


Figure 2.13.: Non-equidistant discretization grid used in the FDM solvers, c.f. [53, Fig. 4.3].

Finally, the semi-vectorial approximation neglects the second order derivatives $\partial_x \left(\frac{1}{\varepsilon_r} \frac{\partial \varepsilon_r}{\partial y} E_y \right)$ for the TE modes and $\partial_y \left(\frac{1}{\varepsilon_r} \frac{\partial \varepsilon_r}{\partial x} E_x \right)$ for the TM modes which arise in the calculations. These terms otherwise couple the x and y components.

Now the main FDM idea to discretize fields on a grid is applied. Figure 2.13 shows one node in the grid and all its direct neighbors to the north, east, south and west. The grid points are labeled with horizontal and vertical coordinates p and q , respectively. The distances between points n , e , s and w are allowed to vary along the grid.

The next step is to approximate all derivatives in Eq. (2.34) with the help of Taylor series expansions. For example, the expansions of the E-field in four directions

$$E_{x,p+1,q} = E_{x,p,q} + \left. \frac{\partial E_x}{\partial x} \right|_{p,q} \cdot e + \frac{1}{2!} \left. \frac{\partial^2 E_x}{\partial x^2} \right|_{p,q} \cdot e^2 + O(e^3) \quad (2.35)$$

$$E_{x,p-1,q} = E_{x,p,q} - \left. \frac{\partial E_x}{\partial x} \right|_{p,q} \cdot w + \frac{1}{2!} \left. \frac{\partial^2 E_x}{\partial x^2} \right|_{p,q} \cdot w^2 + O(w^3) \quad (2.36)$$

$$E_{x,p,q+1} = E_{x,p,q} + \left. \frac{\partial E_x}{\partial y} \right|_{p,q} \cdot s + \frac{1}{2!} \left. \frac{\partial^2 E_x}{\partial y^2} \right|_{p,q} \cdot s^2 + O(s^3) \quad (2.37)$$

$$E_{x,p,q-1} = E_{x,p,q} - \left. \frac{\partial E_x}{\partial y} \right|_{p,q} \cdot n + \frac{1}{2!} \left. \frac{\partial^2 E_x}{\partial y^2} \right|_{p,q} \cdot n^2 + O(n^3) \quad (2.38)$$

can be truncated (by ignoring the O-terms) and combined as (Eq. (2.35)) $\cdot w$ + (Eq. (2.36)) $\cdot e$ to yield an approximation for the derivative

$$\left. \frac{\partial^2 E_x}{\partial x^2} \right|_{p,q} \approx \frac{2}{ew(e+w)} (w \cdot E_{x,p+1,q} + e \cdot E_{x,p-1,q} - (e+w) \cdot E_{x,p,q}). \quad (2.39)$$

The error is $O(h^2)$ for an equidistant grid. In the non-equidistant case, an additional error with $O(e-w)$ emerges and hence there should not be too many non-equidistant nodes in the grid and if there are, the difference in distances should be small.

A similar derivation can be performed for $\left. \frac{\partial^2 E_x}{\partial y^2} \right|_{p,q}$ and a slightly more involved derivation for $\frac{\partial}{\partial x} \left(\frac{1}{\varepsilon_r} \frac{\partial \varepsilon_r}{\partial x} E_x \right)$.

After all derivatives in Eq. (2.34) are replaced by their approximations, we get a set of difference equations for all points in the grid¹⁵

$$\begin{aligned} & \alpha_w E_{x,p-1,q} + \alpha_e E_{x,p+1,q} + \alpha_n E_{x,p,q-1} + \alpha_s E_{x,p,q+1} + \\ & (\alpha_x + \alpha_y) E_{x,p,q} + (k_0^2 \varepsilon_{r,(p,q)} - \beta^2) E_{x,p,q} = 0, \end{aligned} \quad (2.40)$$

where

$$\begin{aligned} \alpha_n &= \frac{2}{n(n+s)} & \alpha_e &= \frac{2}{e(e+w)} \frac{2\varepsilon_{r,(p+1,q)}}{\varepsilon_{r,(p,q)} + \varepsilon_{r,(p+1,q)}} \\ \alpha_s &= \frac{2}{s(n+s)} & \alpha_w &= \frac{2}{w(e+w)} \frac{2\varepsilon_{r,(p-1,q)}}{\varepsilon_{r,(p,q)} + \varepsilon_{r,(p-1,q)}} \\ \alpha_y &= -(\alpha_n + \alpha_s) & \alpha_x &= \frac{-4}{ew} + \alpha_e + \alpha_w. \end{aligned} \quad (2.41)$$

All points of E_x on the grid can be rearranged into a vector Φ (e.g. by stacking the columns of the grid matrix on top of each other) and the $\alpha_{\{n,e,s,w,x,y\}}$ coefficients can be collected into a matrix $\underline{\mathbf{A}}$. With this, the discrete wave Eq. (2.40) can be rewritten as a classical matrix eigenvalue problem $\underline{\mathbf{A}}\Phi = \beta^2\Phi$, solvable with linear algebra software. The eigenvalues are the squared propagation constants β^2 belonging to the transversal field values E_x , which need to be rearranged from vector into matrix form by unstacking the columns.

Finally, to get all components of the TE and TM modes, similar derivations need to be performed for the E_y , H_x and H_y components.

Figure 2.14 shows the six lowest order modes of a circular fiber, computed with the linear polarized solver. In addition to the fields in the figure, there are six y polarized modes with identical power distributions and propagation constants. Note that the mode profiles are different from the vector modes in Fig. 2.5, which were computed with the solver presented in Section 2.3.3.2. In Appendix A.4.2, we show how a set of vector modes can be combined into a set of linearly polarized modes. The NR waveguide modes are almost linearly polarized and the two solvers give very similar results. We have already shown the modes in Fig. 2.9.

¹⁵ The constants α should not be confused with waveguide attenuation α introduced in Section 2.4.1.

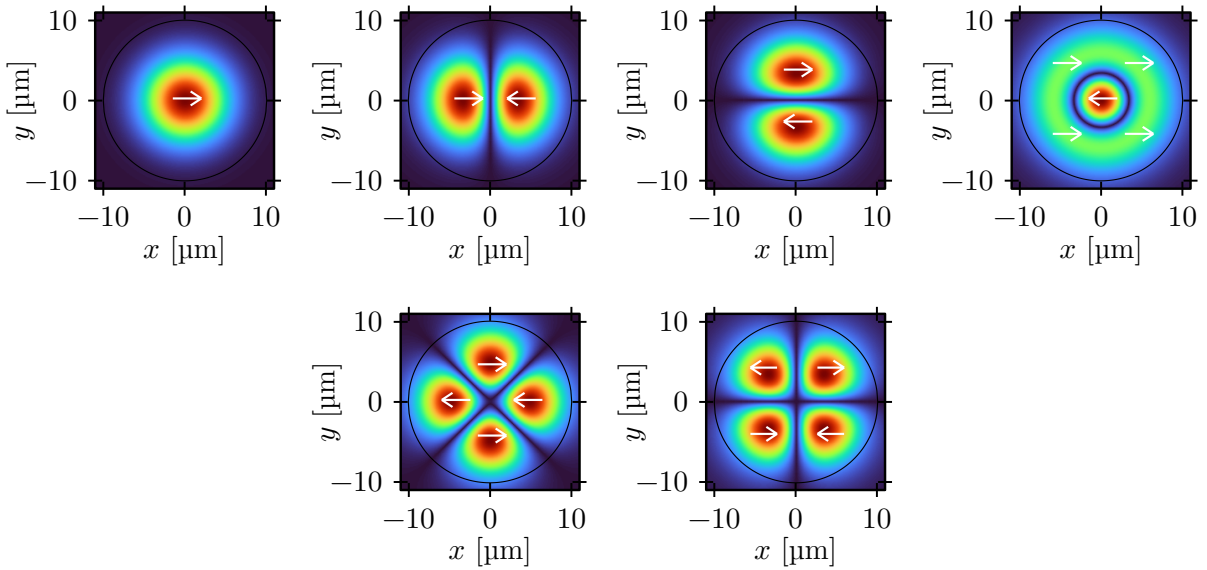


Figure 2.14.: Transversal electric field distributions of the six modes LP_{01x} , LP_{11ax} , LP_{11bx} , LP_{02x} , LP_{21ax} and LP_{21bx} of FMF 2 (graded index) in Table 2.2, computed with the linear polarized solver. Colors encode magnitudes and arrows polarization directions.

2.3.3.2. The Full-Vectorial FDM Solver

The solver we almost exclusively use throughout the thesis is a full-vectorial FDM, based on [57]. We started from the freely available MATLAB code [58] of [56] and dropped support for material anisotropy.

The derivation is similar to the procedure presented in Section 2.3.3.1, but with some important differences. Since it does not matter which two of the six field components are computed, one can choose the H_x and H_y components instead. This has the benefit that the magnetic field is continuous at permittivity borders and $\nabla \cdot \mathbf{H} = \mathbf{0}$ ensures that there are no spurious (non-physical) modes [59]. The resulting difference equations (which now also couple the x and y components) can again be collected into a matrix-vector eigenvalue problem where the solution gives propagation constants and mode fields again.

The main difference to the computed modes of the semi-vectorial solver presented in Section 2.3.3.1 is, that now all E- and H-field components are nonzero. Depending on the waveguide and mode order, the ratio between both transversal components can assume all values. For example, the TE_0 mode of a NR waveguide is very close to linear polarization and its E_x component is much stronger than its E_y component (similarly $H_y \gg H_x$). As a second example, consider a circular step or graded index fiber. The circular geometry leads to degenerate x and y modes. Now assume that the x polarized HE_{11} mode is rotated by 45° . The resulting mode's E_x and E_y components now assume the same amplitude. The E_z and H_z components have small but nonzero amplitudes for all geometries and modes.

2.4. Material Nonlinearity and Four-Wave Mixing

This section covers an introduction to nonlinear propagation of light in matter, with focus on communications. We recommend [60] for a similar but more detailed introduction and in-depth analysis of the topics only briefly mentioned here, as well as [61], [62] (in German language) and [63] where the latter two focus on communications. The ultimate goal of this section is to arrive at very useful and remarkably simple equations, which enable us to assess the conversion efficiency of the nonlinear processes we want to use for all-optical signal processing in the remainder of the thesis. Here, we derive an approximation for the generated signal's power at the end of the waveguide. In Chapter 4, we derive propagation equations for a discrete set of CW waves in frequency domain which model the evolution of wave powers *along* the waveguide.

2.4.1. The Nonlinear Material Polarization

We start by adding nonlinear material polarization effects to the constitutive relation Eq. (2.5) of the electric displacement field. When a light wave interacts with material, it slightly displaces the electrons from their nuclei and atoms from their equilibrium positions in molecules, creating small dipoles. Since light frequency is in the Terahertz regime, the dipoles radiate back to the medium and influence light propagation. Therefore, the electric displacement is driven by two components: directly by the electric field – proportional to the vacuum permittivity ε_0 – and by the induced dipoles. The constitutive relation can now be written as

$$\tilde{\mathbf{D}}(t) = \varepsilon_0 \tilde{\mathbf{E}}(t) + \tilde{\mathbf{P}}(t), \quad (2.42)$$

where the material polarization $\tilde{\mathbf{P}}(t)$ measures the dipole moment per unit volume and can be expanded as a power series of the electric field¹⁶:

$$\begin{aligned} \tilde{\mathbf{P}}(t) &= \varepsilon_0 \overset{\leftrightarrow}{\chi}^{[1]} \tilde{\mathbf{E}}(t) + \varepsilon_0 \overset{\leftrightarrow}{\chi}^{[2]} : \tilde{\mathbf{E}}(t) \tilde{\mathbf{E}}(t) + \varepsilon_0 \overset{\leftrightarrow}{\chi}^{[3]} : \tilde{\mathbf{E}}(t) \tilde{\mathbf{E}}(t) \tilde{\mathbf{E}}(t) + \dots \\ &= \tilde{\mathbf{P}}^{[1]}(t) + \tilde{\mathbf{P}}^{[2]}(t) + \tilde{\mathbf{P}}^{[3]}(t) + \dots \end{aligned} \quad (2.43)$$

Note that we assume an instantaneous material response in this chapter and extend this power series to a Volterra series in Chapter 4. The first order susceptibility is related to the relative permittivity via

$$\overset{\leftrightarrow}{\chi}^{[1]} + \mathbf{1} = \underline{\varepsilon}_r \quad (2.44)$$

for the general case of anisotropic materials. The real part models refraction and the imaginary part the light attenuation

$$\mathcal{P} \propto e^{-j\alpha z}, \quad (2.45)$$

i.e., the exponential loss of light power in the medium.

All higher order susceptibilities give rise to different types of nonlinear effects, with decreasing magnitude for increasing order. Susceptibilities are tensors of increasing rank, i.e. $\overset{\leftrightarrow}{\chi}^{[1]}$ is a tensor of second rank (a matrix), $\overset{\leftrightarrow}{\chi}^{[2]}$ a tensor of rank 3, etc.

Figure 2.15 shows three different exemplary potentials by which electrons can be bound to their atoms, see [60, ch. 1.4]. The displacement and retraction force of an electron are the first

¹⁶ We introduce material polarization $\tilde{\mathbf{P}}(t)$ in the constitutive relation as shown. Alternatively, it is possible to introduce a current density $\tilde{\mathbf{J}}(t) = \partial_t \tilde{\mathbf{P}}(t)$ in Ampère's law Eq. (2.12) driven by the material polarization. See for example [64, Chapter 3.3].

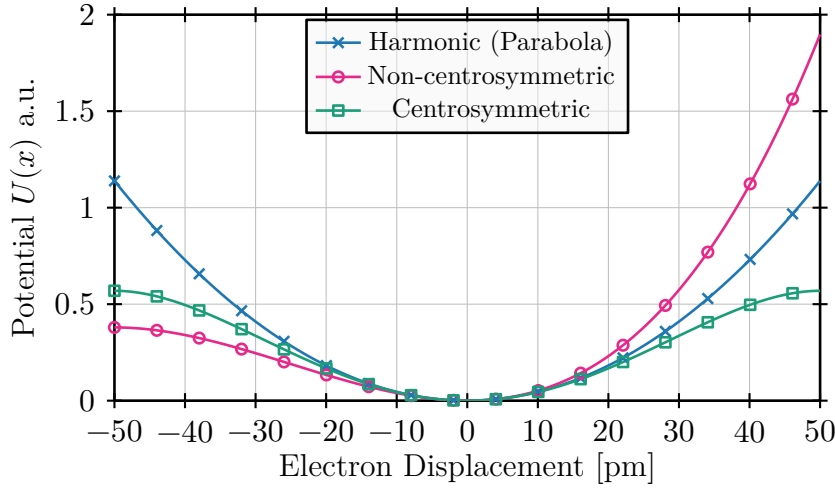


Figure 2.15.: Schematic of different types of electron potential wells. Harmonic potential (no nonlinearity), potential in a non-centrosymmetric medium (all susceptibilities $\vec{\chi}^{[1]}, \vec{\chi}^{[2]}, \vec{\chi}^{[3]}, \dots$ are nonzero) and potential in a centrosymmetric medium (only odd susceptibilities $\vec{\chi}^{[1]}, \vec{\chi}^{[3]}, \vec{\chi}^{[5]}, \dots$ are nonzero).

derivative of the potential. Hence, a parabolic potential leads to purely linear behavior and all other potentials introduce nonlinear effects. The two depicted non-parabolic potentials have a term of third and fourth order, respectively and it can be seen that they are very close to the parabolic one for low displacements, i.e., low light intensities of the electric field do not create strong nonlinear effects. In this regime, the material response is linear in very good approximation and only $\vec{\chi}^{[1]}$ is of relevance. However, with increasing light intensity and electron displacement nonlinear effects start to grow and higher order susceptibilities $\vec{\chi}^{[2]}, \vec{\chi}^{[3]}$, etc. start to become important. Note that not only the light intensity is important, but also the propagation length where nonlinear effects can build up. For example, due to the long distances in trans-oceanic communications, nonlinearity plays a significant role – even though optical fibers have relatively low nonlinearity.

If the electric field is rotated by 180° in a material with inversion symmetry (centrosymmetric material), the material polarization field also has to rotate accordingly. Hence, all even orders of susceptibilities need to vanish and the electron potential is symmetric in electron displacement (see nonlinear potentials in Fig. 2.15).

The effects of a *linear* medium on light are a frequency-dependent attenuation and phase shift, but no new frequency component can arise. A nonlinear material however, will always generate new frequencies at harmonics, sums and differences of the propagating frequencies.

We only consider centrosymmetric materials, since the core materials we use are always either silicon or silica – both have inversion symmetry. Furthermore, all susceptibilities higher than third order are negligible for optical communications. Therefore, the constitutive relation simplifies to

$$\vec{D}(t) = \varepsilon_0 (\mathbf{1} + \vec{\chi}^{[1]}) \vec{E}(t) + \varepsilon_0 \vec{\chi}^{[3]} : \vec{E}(t) \vec{E}(t) \vec{E}(t). \quad (2.46)$$

However, it is instructional to start with the second order nonlinearity induced by $\vec{\chi}^{[2]}(t)$ for the discussion of generated frequencies. For this discussion we also drop the tensor and vector nature of susceptibilities and fields. To see all types of second order nonlinear effects, we need to

model the electric field with at least two real sinusoidal components

$$\tilde{E}(t) = \hat{E}_1 e^{j\omega_1 t} + \hat{E}_2 e^{j\omega_2 t} + \hat{E}_1^* e^{-j\omega_1 t} + \hat{E}_2^* e^{-j\omega_2 t} =: \dot{p}_1 + \dot{p}_2 + \dot{n}_1 + \dot{n}_2, \quad (2.47)$$

where we define $\dot{p}_i = \hat{E}_i e^{j\omega_i t}$ and $\dot{n}_i = \dot{p}_i^* = \hat{E}_i^* e^{-j\omega_i t}$ as shorthand for fields at *positive* and *negative* frequencies (the circles are added to avoid confusion between \dot{n} and the refractive index n). Now we can compute the second order material polarization

$$\begin{aligned} \tilde{P}^{[2]} &= \varepsilon_0 \chi^{[2]} \tilde{E}^2 = \varepsilon_0 \chi^{[2]} (\dot{p}_1 + \dot{p}_2 + \dot{n}_1 + \dot{n}_2)^2 \\ &= \varepsilon_0 \chi^{[2]} (\dot{p}_1^2 + 2\dot{p}_1 \dot{n}_1 + 2\dot{p}_1 \dot{p}_2 + 2\dot{p}_1 \dot{n}_2 \\ &\quad + \dot{n}_1^2 + 2\dot{p}_2 \dot{n}_1 + 2\dot{n}_1 \dot{n}_2 \\ &\quad + \dot{p}_2^2 + 2\dot{p}_2 \dot{n}_2 \\ &\quad + \dot{n}_2^2) \\ &= \varepsilon_0 \chi^{[2]} (\underbrace{\dot{p}_1^2 + \dot{p}_2^2}_A + \underbrace{2\dot{p}_1 \dot{p}_2}_B + \underbrace{2\dot{p}_1 \dot{n}_2}_C + \underbrace{\dot{p}_1 \dot{n}_1 + \dot{p}_2 \dot{n}_2}_D + \underbrace{\text{c.c.}}_E), \end{aligned} \quad (2.48)$$

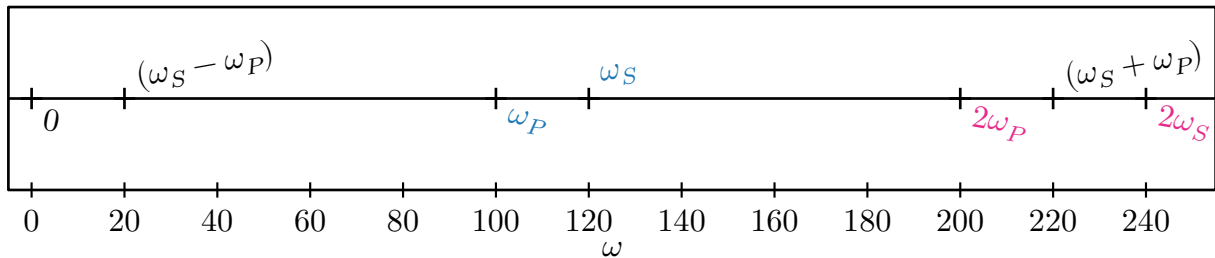
with 16 summands in total. For $\omega_1 \neq \omega_2$, the resulting field has $9 + 4 = 13$ distinct frequencies: nine generated frequencies (note that both, $\dot{p}_1 \dot{n}_1$ and $\dot{p}_2 \dot{n}_2$, combine to frequency zero) and four input frequencies. Figure 2.16a shows all non-degenerate positive frequency components. The categories of generated fields have different interpretations:

- A: Frequencies at the double of one input frequency, this is called **second harmonic generation (SHG)**.
- B: Frequencies at the sum of two input frequencies, this is called **sum frequency generation (SFG)**.
- C: Frequencies at the difference of two input frequencies, this is called **difference frequency generation (DFG)**.
- D: Frequencies at frequency zero, this is called **optical rectification (OR)**.
- E: All other frequencies are complex conjugate copies of the above groups and are collected in the c.c. term¹⁷.

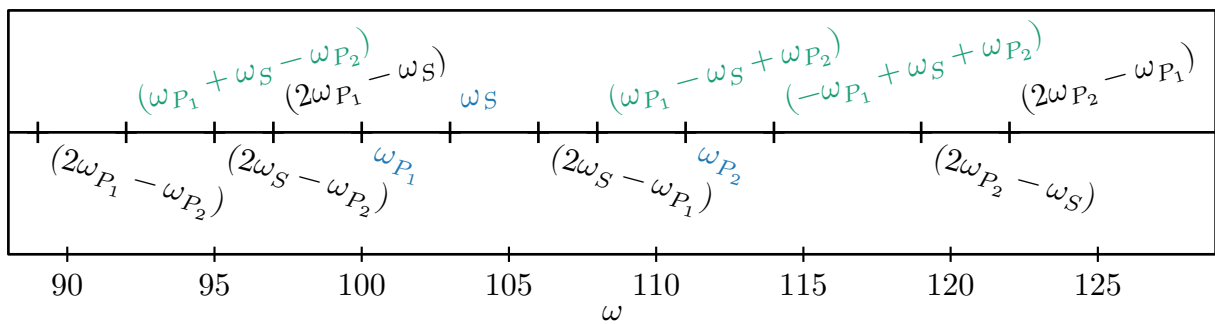
To see all third order nonlinear effects, we need real sinusoidal fields at least at three frequencies

$$\tilde{E}(t) = \hat{E}_1 e^{j\omega_1 t} + \hat{E}_2 e^{j\omega_2 t} + \hat{E}_3 e^{j\omega_3 t} + \text{c.c.} =: \dot{p}_1 + \dot{p}_2 + \dot{p}_3 + \dot{n}_1 + \dot{n}_2 + \dot{n}_3. \quad (2.49)$$

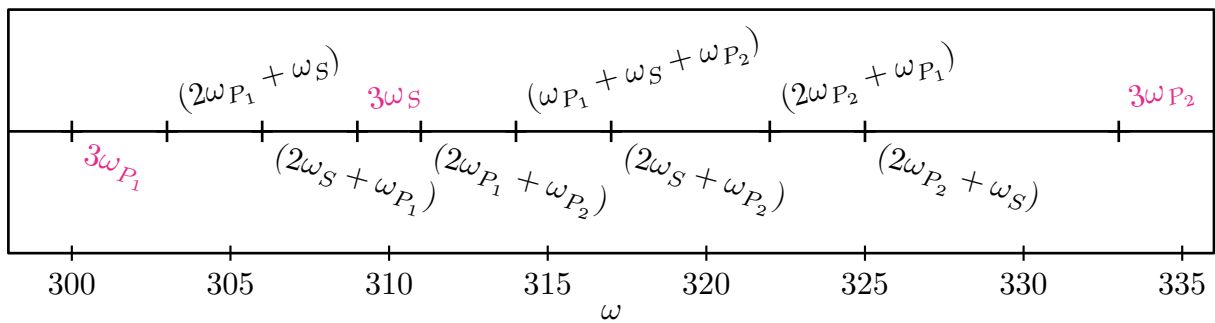
¹⁷ We divided the two terms $2\dot{p}_1 \dot{n}_1$ and $2\dot{p}_2 \dot{n}_2$ which have frequency zero among the positive and negative half of the spectrum. Thus, half of them is hidden in the c.c. and the factor 2 disappears.



(a) Frequencies arising from the second order nonlinear interaction of two sinusoidal waves S and P .



(b) Frequencies arising from the third order nonlinear interaction of three sinusoidal waves S , P_1 and P_2 , zoom on the input frequency range.



(c) Frequencies arising from the third order nonlinear interaction of three sinusoidal waves S , P_1 and P_2 , zoom on the range at three times the input frequencies.

Figure 2.16.: Frequencies generated by nonlinear propagation of two and three sinusoidal waves in a nonlinear medium. Only the positive spectral components are shown since the negative spectrum is the conjugated and mirrored copy of the positive one. Input waves are blue, SHG and third harmonic generation (THG) terms are red and FWM terms are green.

This time, we have to compute the third power of six components leading to 216 summands

$$\begin{aligned}
\tilde{P}^{[3]} &= \varepsilon_0 \chi^{[3]} \tilde{E}^3 = \varepsilon_0 \chi^{[3]} (\hat{p}_1 + \hat{p}_2 + \hat{p}_3 + \hat{n}_1 + \hat{n}_2 + \hat{n}_3)^3 \\
&= \varepsilon_0 \chi^{[3]} (\underbrace{3\hat{p}_1^2 \hat{n}_1 + 6\hat{p}_1 \hat{p}_2 \hat{n}_2 + 6\hat{p}_1 \hat{p}_3 \hat{n}_3}_{\text{A}} + \underbrace{\hat{p}_1^3}_{\text{B}} + \underbrace{6\hat{p}_1 \hat{p}_2 \hat{p}_3}_{\text{C}} \\
&\quad + \underbrace{6\hat{p}_1 \hat{p}_2 \hat{n}_3 + 6\hat{p}_1 \hat{n}_2 \hat{p}_3 + 6\hat{n}_1 \hat{p}_2 \hat{p}_3}_{\text{D}} + \underbrace{3\hat{p}_1^2 \hat{p}_2 + 3\hat{p}_1^2 \hat{p}_3 + 3\hat{p}_1^2 \hat{n}_2 + 3\hat{p}_1^2 \hat{n}_3}_{\text{E}} \\
&\quad + \underbrace{[\dots]}_{\text{F}} + \underbrace{\text{c.c.}}_{\text{G}}). \tag{2.50}
\end{aligned}$$

However, many summands produce the same frequency and for $\omega_1 \neq \omega_2 \neq \omega_3$, the resulting field has $38+6 = 44$ distinct frequencies (generated + input frequencies). Figures 2.16b and 2.16c show all non-degenerate positive frequency components. Again, the groups have different meanings:

- A: Frequencies at ω_1 , this leads to the intensity dependent refractive index (also called Kerr effect) $n = n_0 + n_2 I$, where n_0 is the regular refractive index. Self-phase modulation (SPM) and cross-phase modulation (XPM) also belong to this group.
- B: Frequencies at three times ω_1 , called THG.
- C: Frequencies at the sum of three input frequencies, called SFG.
- D: Frequencies at the sum of two positive and one negative input frequency, the result of DFG processes. *This is called FWM.*
- E: We collected all processes at the double of one frequency plus or minus one other frequency in this group. Several processes belong here, among others degenerate FWM and modulational interaction (e.g. $\hat{p}_1^2 \hat{n}_2$).
- F: In Eq. (2.50), we mainly listed processes for \hat{p}_1 . There exist alike terms for \hat{p}_2 and \hat{p}_3 which are hidden in this ellipsis – for a more complete list, see [60, p. 13].
- G: Again, all complex conjugate copies of the terms in categories A to F are hidden in c.c.

We are interested in the FWM processes (category D), which are all the product of three interacting frequencies: two positive and one negative. They are typically further categorized into optical phase conjugation (OPC) and Bragg scattering (BS). Their generated wave will be a phase conjugate copy of the wave which has a negative contribution in the summand. For example, the result of $6\hat{p}_1 \hat{p}_2 \hat{n}_3$ will be a conjugate copy of the wave at ω_3 . Hence, if ω_3 is the frequency of the signal to be converted (in the case of $6\hat{p}_1 \hat{p}_2 \hat{n}_3$), the process is called OPC and BS¹⁸ otherwise.

¹⁸ According to [65], the name BS comes from an analogy to a spatial process which was analyzed in [66]. In that process, two photons with opposite momentum are annihilated and two photons at anti-Stokes frequencies are emitted in the process. Although the analogy is somewhat weak (the process in [66] is for counter-propagating waves and deals with the instability of modal profiles due to self-focusing), the name BS is widely used for this kind of FWM process.

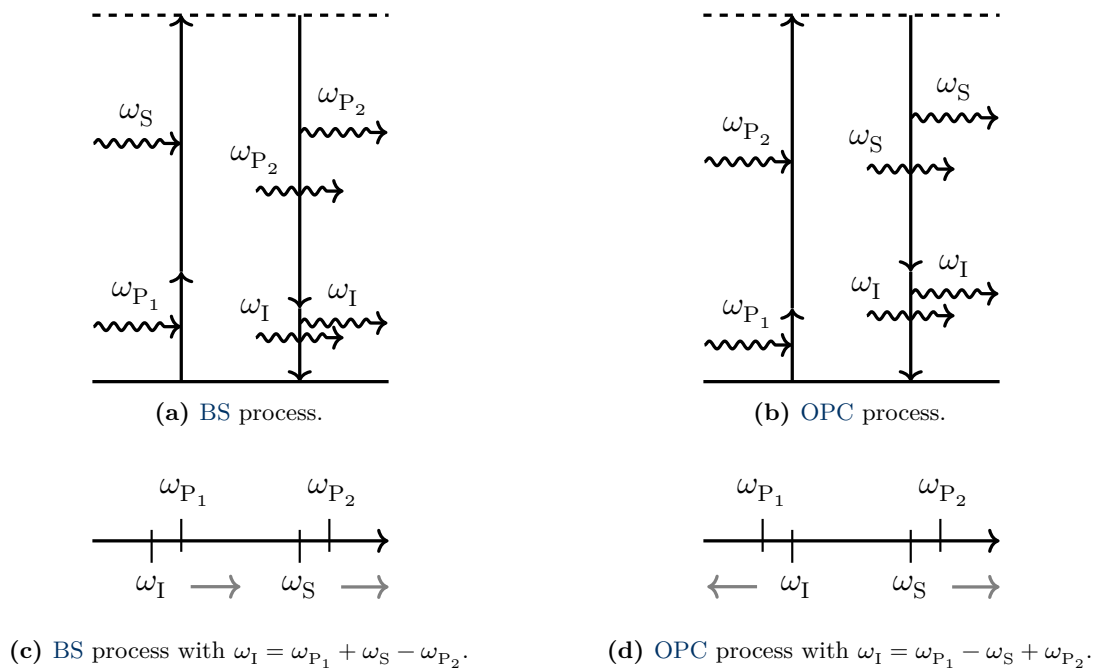


Figure 2.17.: Energy diagrams and frequencies for a BS and an OPC FWM process. In both processes, two photons are destroyed to elevate an atom or molecule to a higher virtual state. Then, the state falls back to the ground level due to stimulated emission (depicted as photons passing through a state transition) and creates two new photons. One photon at the frequency of pump 2 for BS (at the frequency of the signal for OPC) and one photon at the idler frequency. The gray arrows in Fig. 2.17c and Fig. 2.17d indicate the idler frequency's direction when the signal frequency is changed.

This figure shows the contribution of electrons in the matter, Fig. 2.19 shows the molecular contribution.

2.4.2. Electronic Contribution to Nonlinearity

The processes in Eq. (2.50) can have a variety of quantum mechanical origins, an overview is found in e.g. [19, Fig. 5]. We are interested in BS and OPC in silicon or silica crystals. In these cases, the main contributions come from the displacement of electrons and nuclei by the electric field. Energy level diagrams and involved frequencies of a BS and an OPC process are shown in Fig. 2.17. We call the interacting waves pump 1 (P_1), pump 2 (P_2), signal (S) and idler (I) in anticipation of the FWM principle we use in the rest of the thesis (introduced in Section 2.4.5): two pumps and the signal are launched into a waveguide and generate an idler by nonlinear interaction during propagation.

In the figure, state transitions are depicted with regular arrows and wavy arrows depict photons. If photons terminate in a transition arrow, they are annihilated. If they originate from a transition arrow, they are created. If they go through a transition arrow, they stimulate that transition and are not affected otherwise. Energy conservation dictates that the sum of photon frequencies stays constant in the process, since photon energy is $\hbar\omega$. This translates to conservation of transition lengths in the energy diagrams, i.e. the sum length of the two upward transitions on the left needs to match the sum length of the two downward transitions on the right.

To understand the energy level transitions, consider Fig. 2.17a which shows a BS process. Here, a photon of pump 1 and a signal photon are annihilated to elevate an electron or nucleus to a higher *virtual* state. A virtual state can only be occupied for a very brief moment in the order of femtoseconds [62, p. 212]. Hence, the state immediately transitions back to the ground state by emitting two new photons. This emission process is not spontaneous, but stimulated by the presence of the strong pump 2 field and the presence of the idler field (which grows along the waveguide). In this case, energy conservation dictates

$$\omega_{P_1} + \omega_S = \omega_{P_2} + \omega_I \quad (2.51)$$

or

$$\omega_I = \omega_{P_1} + \omega_S - \omega_{P_2}. \quad (2.52)$$

This determines which idler frequency is generated when signal and pumps are fixed, as well as in which direction the idler frequency moves if the signal frequency is changed. In the BS process, the idler *follows* the signal (which is indicated in Fig. 2.17c) and always maintains the same distance (exactly the frequency separation between the two pumps).

Figures 2.17b and 2.17d show the energy levels and frequencies for an OPC process. In this case, we have

$$\omega_I = \omega_{P_1} - \omega_S + \omega_{P_2}, \quad (2.53)$$

which means the idler will move in opposite direction as the signal and the pump separation does not impose a constraint on the distance between the two.

2.4.3. Molecular Contribution to Nonlinearity

A second important contribution to the two FWM processes comes from interactions with the crystal lattice – Raman and Brillouin scattering. This is a very brief section and we refer the reader to [62, Chapters 8 and 9], [63, Chapters 10 and 11] and [60, Chapters 8-10] for a detailed analysis.

In Raman and Brillouin scattering, lattice vibrations (or their associated quantum particle the *phonon*) are either stimulated or annihilated in the process. Since the quantum state of the material is changed after the interaction, it is *non-parametric*. This implies that energy is transferred to or from the material and that energy diagrams involve actual energy states, not only virtual states. The simplest forms of Raman scattering are shown in Fig. 2.18. Figure 2.18a shows how a *Stokes* wave is created by annihilating a photon at frequency ω and emitting a photon at the lower frequency ω_{St} . The energy difference between the photons is used to emit a phonon. The phonon energy spectrum depends on the material and determines both, Raman gain and the frequency difference between the source and Stokes waves $\omega_{St} = \omega - \Omega_R$. For silicon and silica, the Raman gain peak is near 15 THz with a **full width at half maximum (FWHM)** bandwidth of roughly 10 THz in silica [63, chapter 10.2] and 100 GHz in silicon [67].

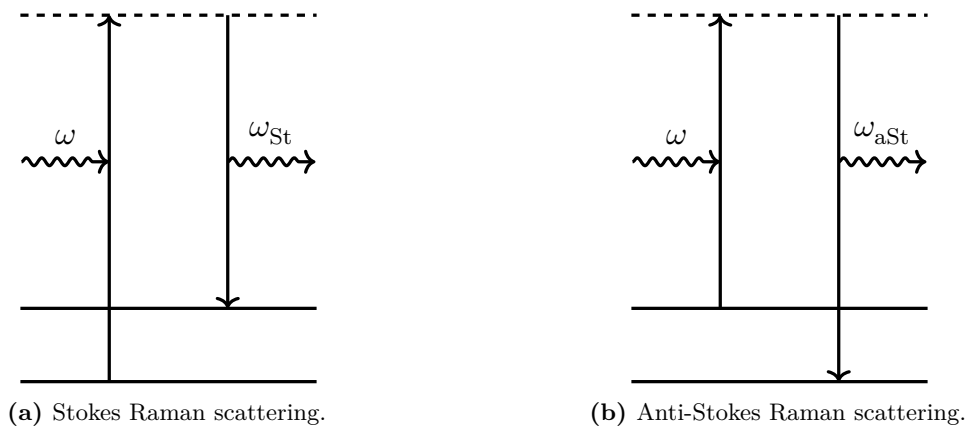


Figure 2.18.: Energy diagrams of the two Raman scattering processes. In the Stokes process, power is transferred to lower frequencies by elevating a molecule or atom to a higher vibrational energy state (creating an optical phonon). In the anti-Stokes process, the power is transferred to higher frequencies by annihilating an optical phonon and creating a photon with the sum energy.

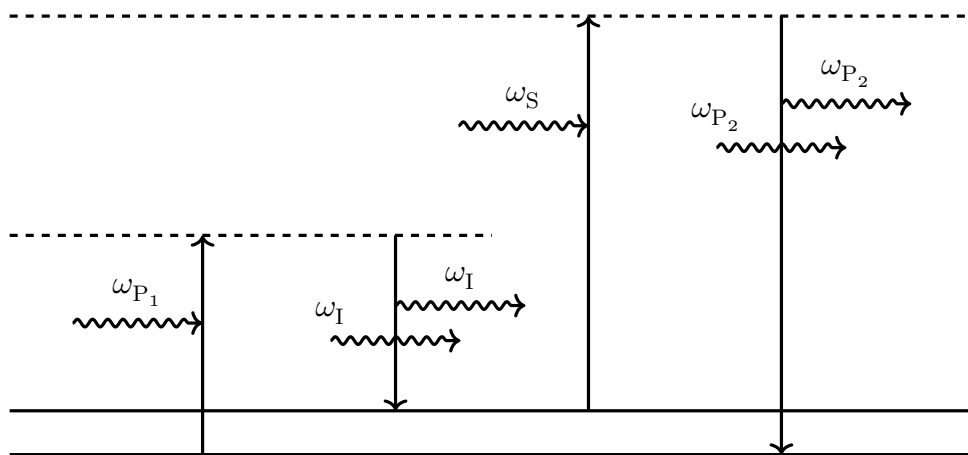


Figure 2.19.: Stimulated Raman scattering contribution to the BS process in Fig. 2.17.

Figure 2.18b shows the *anti-Stokes* process where a photon scatters with an atom or molecule which is already in a higher energy state (i.e. scatters with a phonon) and emits a photon at higher frequency $\omega_{aSt} = \omega + \Omega_R$. Since the anti-Stokes process requires a phonon, it is much less likely to happen, compared to the Stokes process.

The Raman contribution to BS is shown in Fig. 2.19. The process starts with a stimulated creation of a Stokes photon, leaving the system in a higher energy state. From there, a stimulated anti-Stokes process takes place and annihilates the phonon.

The two kinds of phonons which can exist in a crystal are shown in Fig. 2.20. On the one hand, scattering of photons with optical phonons (Fig. 2.20a) is the Raman scattering described above. On the other hand, scattering of photons with acoustic phonons (Fig. 2.20b) is called Brillouin scattering. Optical phonons can be thought of as particles of molecule vibrations and acoustic phonons as particles of sound waves and Brillouin scattering is the reflection of photons from acoustic waves traveling along the waveguide.

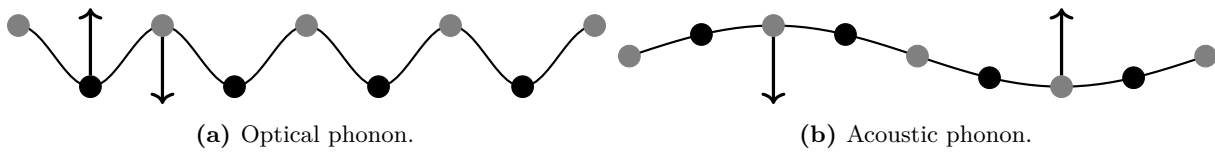


Figure 2.20.: The two types of possible phonons in a crystal, c.f. [62, p. 311].

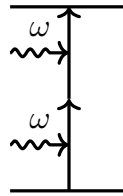


Figure 2.21.: Energy diagram of **two-photon absorption**. Two photons are annihilated to lift an atom or molecule to a higher energy state.

Hence, the energy of acoustic phonons is much lower and with it the frequency shift – it is in the order of 10 GHz with **FWHM** bandwidth of roughly 20 MHz [62, p. 278]. Usually, Brillouin scattering is an unwanted process in optical communications, and suppression techniques are utilized [54, chapter 9.2.3].

2.4.4. Further Nonlinear Processes

A multitude of further processes can contribute to nonlinear interaction. For example, the electric fields can rotate polar molecules in liquids and gases, which is a large contribution to attenuation in fibers with residual water in the core. We ignore this effect in the thesis.

Another important non-parametric process is **two-photon absorption (TPA)**. When the sum energy of two photons is close to a transition energy between two (real, non-virtual) states, they can be annihilated and the system is left in a higher energy state. **Figure 2.21** shows the simple energy diagram of this absorption process. Since this process removes two photons from the propagating light, it leads to a nonlinear attenuation.

The system eventually falls back to the ground state by either emitting a non-coherent photon at a the sum frequency, by emitting a phonon, or by stimulated emission from the propagating fields (called **free-carrier absorption (FCA)**). The latter case leads to yet another nonlinear attenuation. To reduce the number of free carriers and thus **FCA**, a diode under reverse bias can be added to the waveguide [20]. Thus, we assume that all free carriers are removed by such a diode and ignore **FCA** in the rest of this thesis.

2.4.5. Bragg Scattering and Optical Phase Conjugation

Our goal is the optimization of waveguide geometries for all-optical signal processing. With the help of **FWM**, we can achieve wavelength conversion through the **BS** process and optical phase conjugation through **OPC**. For that, 2 pumps are launched together with the signal into a waveguide with material nonlinearity. At the output of the waveguide, pumps and signal are filtered away and the generated idler with desired properties is extracted.

The principle is sketched in **Fig. 2.22** for an example of a **NR** waveguide. In the most general case of inter-modal **FWM**, the four interacting waves can be in up to four different waveguide modes (*o*), (*p*), (*q*) and (*m*). No mode multiplexer is shown in the figure, but is of course needed in such an experiment.

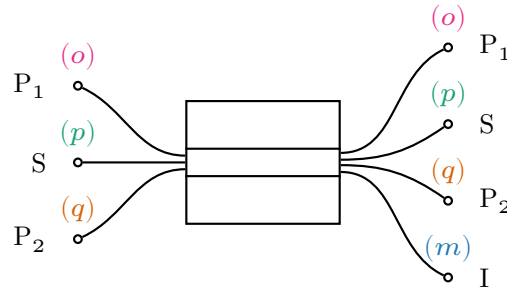


Figure 2.22.: Working principle of inter-modal FWM-based all-optical signal processing. Two pumps and the signal enter the waveguide in modes (o) , (p) and (q) and generate a FWM idler through nonlinear interaction in mode (m) .

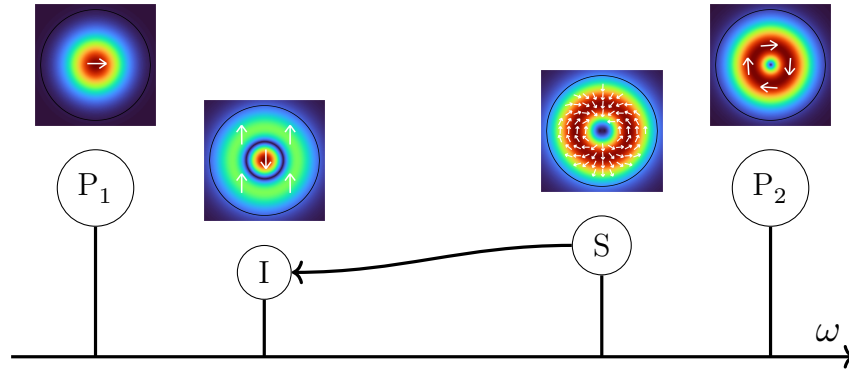


Figure 2.23.: Example of an OPC FWM process. Note that this figure is merely an example and modes are not selected according to any specific condition.

Figure 2.23 shows an example of OPC in a multimode fiber, where modes were arbitrarily selected. The horizontal arrow indicates that a (conjugated) copy of the signal is created in the process.

In the rest of the thesis, we consider the OPC process and one BS process, namely

$$\text{BS} : \omega_I = \omega_{P_1} + \omega_S - \omega_{P_2} \quad (2.54)$$

$$\text{OPC} : \omega_I = \omega_{P_1} - \omega_S + \omega_{P_2}. \quad (2.55)$$

We do not include the BS process with

$$\omega_I = -\omega_{P_1} + \omega_S + \omega_{P_2} \quad (2.56)$$

in optimizations, since it can always be converted to Eq. (2.54) by simply swapping pump frequencies.

2.4.6. Phase Matching

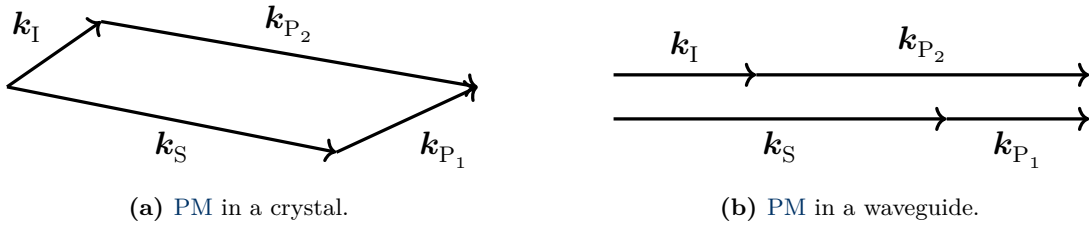


Figure 2.24.: Phase matching diagrams in a crystal and in a waveguide. In the latter, one is not free to choose the propagation direction, since all waves travel along the waveguide. Hence, PM needs to be achieved by means of the magnitude of the wave vectors.

Up to now, we completely ignored that not only energy but also momentum needs to be conserved in all nonlinear processes. The photon momentum is given as $\mathbf{p} = \hbar\mathbf{k}$ with wave vector \mathbf{k} . Since we deal with light propagation in a waveguide in communications applications, it is customary to define the component of the wave vector in the propagation direction as $\beta = \mathbf{k} \cdot \mathbf{e}_z$. This is the so-called *propagation constant* already introduced in Eq. (2.15). In a FWM process, the momentum of all annihilated photons has to match the momentum of all created photons. For example, the momentum of signal and pump 1 has to match the momentum of idler and pump 2 for the BS process in Fig. 2.17a. In Fig. 2.24, two types of momentum conservation are shown. In the general case of FWM in a crystal, the waves can have arbitrary directions, as shown in Fig. 2.24a. However, for propagation in a waveguide all waves are collinear (i.e. they travel in the same direction) and momentum conservation can only be fulfilled by adjusting wave vector lengths (see Fig. 2.24b). Therefore, momentum conservation dictates that the propagation constants have to fulfill

$$\text{BS : } \beta_{P_1} + \beta_S = \beta_{P_2} + \beta_I \quad (2.57)$$

$$\text{OPC : } \beta_{P_1} + \beta_{P_2} = \beta_S + \beta_I. \quad (2.58)$$

The process of adjusting parameters such that Eq. (2.57) or Eq. (2.58) are fulfilled is called *phase matching*. In a perfectly phase-matched experiment, the idler amplitude grows linearly along the waveguide [60, p. 77]. However, if PM is not perfect, the residual *phase mismatch*

$$\text{BS : } \Delta\beta = \beta_{P_1} + \beta_S - \beta_{P_2} - \beta_I \quad (2.59)$$

$$\text{OPC : } \Delta\beta = \beta_{P_1} - \beta_S + \beta_{P_2} - \beta_I \quad (2.60)$$

leads to an oscillation in the idler's amplitude, with a period that depends on the magnitude of the phase mismatch [63, chap. 7.3]. Since propagation constants are frequency dependent and differ for waveguide modes (see Eqs. (2.17) and (2.18)), PM becomes the process of minimizing

$$\text{BS : } \Delta\beta = \beta^{(o)}(\omega_{P_1}) + \beta^{(p)}(\omega_S) - \beta^{(q)}(\omega_{P_2}) - \beta^{(m)}(\omega_I) \quad (2.61)$$

$$\text{OPC : } \Delta\beta = \beta^{(o)}(\omega_{P_1}) - \beta^{(p)}(\omega_S) + \beta^{(q)}(\omega_{P_2}) - \beta^{(m)}(\omega_I). \quad (2.62)$$

We usually maximize the **FWM** efficiency

$$\eta_{\text{FWM}}(\Delta\beta) = \frac{1 - \exp(-(\alpha + j\Delta\beta)L_{\text{wg}})}{(\alpha + j\Delta\beta)L_{\text{wg}}} \quad (2.63)$$

instead (we show in [Appendix A.2](#) that optimizing the **FWM** efficiency minimizes $\Delta\beta$). L_{wg} and α are the waveguide length and the waveguide attenuation exponent, respectively. The **FWM** efficiency was first derived in [68] and extended to **FMFs** in [15], by using Eq. (17) from [69]. A very similar idea is used, e.g., in [70] to assess **FWM** efficiency in silicon rib waveguides. Our numerical **PM** procedure is described in [Chapter 3](#).

2.4.7. Idler Power Estimation

The efficiency of signal conversion can be ultimately defined by the idler power at the waveguide output, or, equivalently, by the CE_{IO} :

Definition 1. We define the input-output conversion efficiency (CE_{IO}) as

$$\text{CE}_{\text{IO}} = \frac{\mathcal{P}_{\text{I}}(z = L_{\text{wg}})}{\mathcal{P}_{\text{S}}(z = 0)}, \quad (2.64)$$

where we always assume that signal power is measured before the waveguide and before any coupling losses occur. Similarly, the idler power is measured after the waveguide and after all output coupling losses occurred.

For given input powers \mathcal{P}_{P_1} , \mathcal{P}_{S} and \mathcal{P}_{P_2} , the idler power can be estimated as [15]

$$\mathcal{P}_{\text{I}} = 4(\gamma^{(mopq)})^2 L_{\text{wg}}^2 \mathcal{P}_{\text{P}_1} \mathcal{P}_{\text{S}} \mathcal{P}_{\text{P}_2} e^{-\alpha L_{\text{wg}}} |\eta_{\text{FWM}}(\Delta\beta)|^2. \quad (2.65)$$

The nonlinearity coefficient is defined as [15], [71]

$$\gamma^{(mopq)} = \frac{\omega_0 n_2}{c_0 A_{\text{eff}\times}^{(mopq)}} \quad (2.66)$$

with the material parameter nonlinear refractive index n_2 and speed of light in vacuum c_0 . The cross effective area between involved modes is given by [54, Chapter 10.2.1]

$$A_{\text{eff}\times}^{(mopq)} = \frac{\sqrt{\mathcal{J}^{(m)} \mathcal{J}^{(o)} \mathcal{J}^{(p)} \mathcal{J}^{(q)}}}{\left| \iint [(\Psi^{(m)})^* \cdot \Psi^{(o)}] [(\Psi^{(p)})^* \cdot \Psi^{(q)}] dA \right|}, \quad (2.67)$$

where $\Psi^{(X)}$ are the transversal mode profiles defined in [Eq. \(2.15\)](#), $\mathcal{J}^{(X)} = \iint |\Psi^{(X)}|^2 dA$ and dA denotes integration over the waveguide cross section.

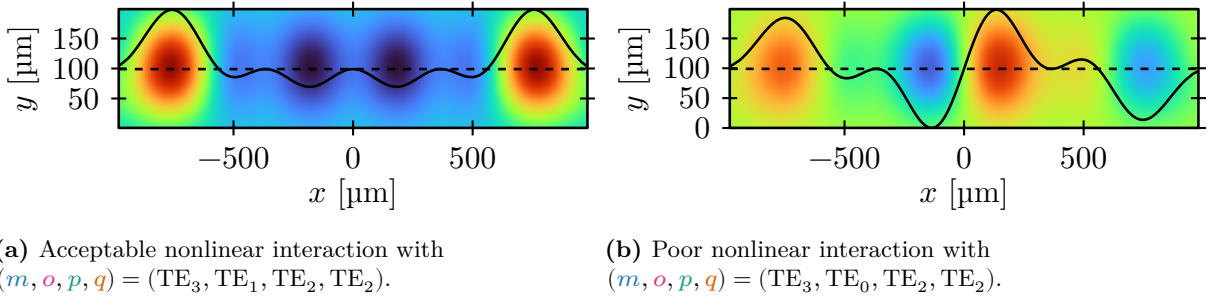


Figure 2.25.: An example of overlapped mode fields (m) , (o) , (p) , and (q) of waveguide 1 (regular) in Table 2.3, demonstrating good and bad nonlinear interaction. The 1D plot shows the magnitude of the field at $y = 100$ nm. Only the power *distribution* is of interest here, hence no scale is shown.

From Eq. (2.65), it is clear that $\mathcal{P}_I \propto |\eta_{\text{FWM}}(\Delta\beta)|^2$. However, this estimate of idler power relies on the three main approximations in η_{FWM} : 1) The attenuation is constant (neither frequency, nor mode dependent). 2) There is no linear coupling. 3) The pumps and signal are only depleted by linear attenuation and not by nonlinear interaction. The third assumption is usually valid in all-optical signal processing experiments, since the pumps and signal are much stronger (usually around 20 dBm and 10 dBm) than the generated idler (typically less than -20 dBm). However, due to the first two assumptions, η_{FWM} fails to capture variable attenuation and linear coupling, which usually need to be considered in real-world applications. The FWM efficiency can be remarkably exact, though, when linear coupling is low due to few propagating modes and the attenuation is flat due to small considered wavelength differences, e.g. in [15] or [14]. In many of the investigated configurations in this thesis, attenuation is quite likely frequency dependent due to the large considered bandwidths. Also, the considered waveguides potentially allow the propagation of many guided modes. Since the group delays of neighboring modes are very close in waveguides with large cores, linear coupling will also have an effect on FWM. Nevertheless, Eq. (2.65) serves as a good metric for a best-case analysis. For example, FWM efficiency predicted the bandwidth quite well in our experiments in Chapter 6. The idler power is computed with high accuracy in our propagation simulation in Chapter 4.

Equation (2.67) adds a dependency of CE_{IO} on the selection of modes, especially the denominator can become very small for certain choices of (m) , (o) , (p) and (q) . Figure 2.25 shows the intensities for two configurations of overlapped and multiplied fields of an exemplary NR waveguide (1 (regular) in Table 2.3). The surface plot depicts the integrand of the denominator in Eq. (2.67) and the black lines show the cross section along $y = 100$ nm. It can be seen that the integral over Fig. 2.25a will give a positive number and the integral over Fig. 2.25b will be close to zero, since positive and negative lobes cancel each other. Therefore, the idler power will be much higher in the first case. In the shown example, the numerically computed nonlinearity coefficients are $\gamma^{(\text{TE}_3, \text{TE}_1, \text{TE}_2, \text{TE}_2)} = 20.69/(\text{W m})$ and $\gamma^{(\text{TE}_3, \text{TE}_0, \text{TE}_2, \text{TE}_2)} = 0.0147/(\text{W m})$ – a factor of 1411 or 31.50 dB. These numbers highly depend on the grid size used for the mode solver. For example, the grid size for the numbers above was $(x \times y) = (800 \times 1200)$ points. Reducing the grid to (200×300) , we get $\gamma^{(\text{TE}_3, \text{TE}_1, \text{TE}_2, \text{TE}_2)} = 20.71/(\text{W m})$ and $\gamma^{(\text{TE}_3, \text{TE}_0, \text{TE}_2, \text{TE}_2)} = 0.0031/(\text{W m})$ – a factor of 6747 or 38.29 dB.

For these integrals, we only consider regions *inside* of the waveguide cores (as shown in Fig. 2.25). This way, we avoid integrating over material borders where the electric field shows Dirac-delta-like behavior. Integrating over borders needs a much higher resolution and even then the results are distorted.

We show in Chapter 5 that good PM can almost exclusively be achieved when either one mode is used for all lasers ($(m) = (o) = (p) = (q)$), or exactly two modes are used with two lasers in each. These cases represent the good case of overlap integrals (similar to Fig. 2.25a), since the product of the fields behaves like a function of fourth order in one case and like two quadratic functions in the second case. In both cases, the lobes are always positive and the integral never becomes zero.

In summary of this rather long Section 2.4, we can optimize PM by maximizing the FWM efficiency $\eta_{\text{FWM}}(\Delta\beta)$ with underlying phase mismatch equations Eq. (2.61) and Eq. (2.62). The idler power is influenced by modal overlap as well, which also needs to be considered and can be derived from η_{FWM} with the help of Eq. (2.65).

3

Numerical Phase Matching and Waveguide Optimizations

In this section, we present our numerical simulation framework for [phase matching](#) and for optimizing waveguide dimensions, both based on the [FWM](#) efficiency defined in [Eq. \(2.63\)](#).

3.1. Numerical Phase Matching

Our main goal is achieving [PM](#) for ultra-broadband operation. We define the [FWM](#) bandwidth as metric of quality:

Definition 2. The [FWM](#) bandwidth B_{FWM} is the frequency range the signal can be moved, while the estimate of idler power ($|\eta_{\text{FWM}}|^2$) does not drop by more than 3 dB from its peak value. All other parameters like waveguide dimensions, pump frequencies and mode assignments are kept constant.

The task of our numerical [phase matching](#) algorithm is to find the highest achievable B_{FWM} of a waveguide with given dimensions and for given [FWM](#) process [BS](#) or [OPC](#). The result is the optimal choice of wavelengths and waveguide modes for the four propagating waves (pumps, signal and idler). We have several possibilities for constraining the optimization. First of all, we need to provide the set of modes which are considered, e.g. we only want guided modes and usually only a subset of them. Secondly, all wavelengths can be constrained. For example, we can force the signal into the C-band and the idler into the O-band to get the optimal [PM](#) for C-to-O-band conversion in the considered waveguide. In this work, we focused on combination of signal and idler wavelengths shown in [Fig. 3.1](#). The pumps can optionally also be constrained if, e.g., only high power lasers for some wavelengths or bands are available in a physical experiment.

Furthermore, if two or more of the four lasers have the same wavelength, [FWM](#) is degenerate.

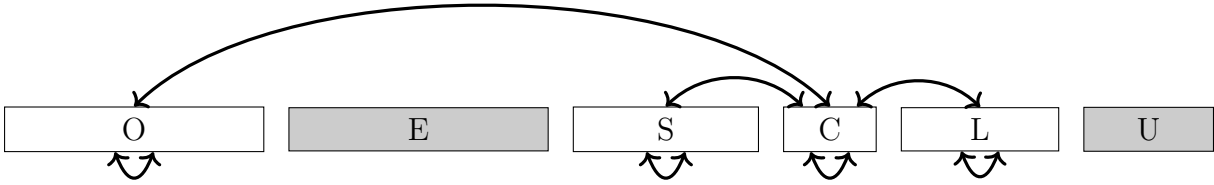


Figure 3.1.: Signal and idler range combinations considered in this work.

Degenerate FWM is not a problem per se, but can lead to problems in the FWM processes we are interested in (BS and OPC). In our experiments, the pumps are stronger than the signal which again is much stronger than the generated idler – roughly 20 dBm, 10 dBm and -30 dBm. Due to linear coupling, the pumps leak into all modes. If the idler wavelength coincides with a pump, it becomes impossible to filter away the pump at the waveguide’s output. For the OPC process (Eq. (2.55)) this means, that the signal can never have the same wavelength as neither pump 1 nor pump 2. For the BS process (Eq. (2.54)) this means that the signal can never have the same wavelength as pump 2. For the alternative BS process (Eq. (2.56)) this means that the signal can never have the same wavelength as pump 1.

Further, enforcing a separation between the two pumps is not necessary for the OPC process. However, the idler in the BS process then has the same wavelength as the input signal, which, of course, defeats the purpose of wavelength conversion. Hence, we always remove configurations from the search space where signal or idler are closer to a pump than 250 GHz (roughly 2 nm) and where the two pumps are closer to each other than 800 GHz (roughly 6.4 nm). Note that these values are suitable for optimizing NR waveguides. We have to use the approach in Appendix A.4.4 for fiber optimizations.

Figure 3.2 shows the normalized squared FWM efficiency $|\eta_{\text{FWM}}(\Delta\beta)/\max|\eta_{\text{FWM}}||^2$ in logarithmic scale, for the BS process in fiber 3 (depressed cladding) in Table 2.2. Normalization is not strictly necessary, it is only convenient to have unit maximum $\eta_{\text{FWM}}(\Delta\beta = 0) = 1$. We show in Appendix A.2 that indeed the maximum is achieved for $\Delta\beta = 0$. This exemplary plot is intended to be similar to the simulated and measured BS results in [15], Fig. 2 (e) and (f). In our example, pump 1 is fixed at its optimum $\lambda_{P_1} = 1538.0$ nm and the mode assignment is $P_1 \rightarrow \text{HE}_{11e}$, $P_2 \rightarrow \text{TE}_{01}$, $S \rightarrow \text{TE}_{01}$, $I \rightarrow \text{HE}_{11e}$ ¹⁹. The wavelengths of signal and pump 2 are on the horizontal and vertical axes, respectively. The dashed gray lines mark where FWM is degenerate, i.e., pump 1, pump 2 or signal coincide. In this plot, the line where pump 1 and pump 2 coincide is out of the depicted range at $P_2 = 1538$ nm.

¹⁹ Note that the mode assignment is swapped compared to [15], i.e. in our simulation I and P_1 are in the fundamental mode HE_{11e} and S and P_2 in the higher order mode TE_{01} , in contrast to [15] where I and P_1 are in LP_{01} and S and P_2 in LP_{11} . In our fiber, the relative group delay of HE_{11e} is *above* TE_{01} (see Fig. 2.6e), while in the fiber used in [15] LP_{01} is *below* LP_{11} (see [14, Fig. 2] where a similar fiber is used). The swapping of group delays depends on the fraction of Germanium in the core and since we do not have that data available, we can’t adjust our fiber. However, we get a good match by just swapping the mode assignment which is sufficient for this comparison.

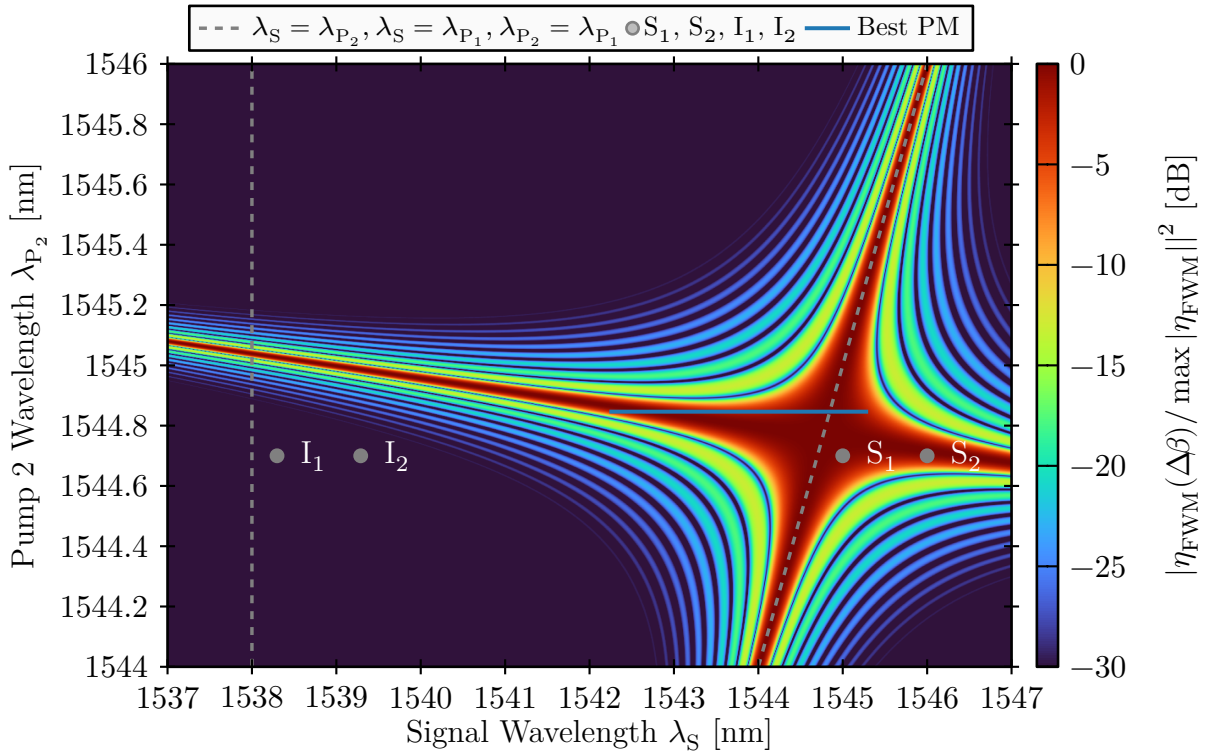


Figure 3.2.: Example of FWM efficiency $|\eta_{\text{FWM}}(\Delta\beta)/\max|\eta_{\text{FWM}}||^2$ for fiber 3 (depressed cladding) in Table 2.2, for the BS process. The fiber and η_{FWM} are similar to [15]. Here, $\lambda_{\text{P}_1} = 1538.0$ nm and the mode assignment is $\text{P}_1 \rightarrow \text{HE}_{11\text{e}}$, $\text{P}_2 \rightarrow \text{TE}_{01}$, $\text{S} \rightarrow \text{TE}_{01}$, $\text{I} \rightarrow \text{HE}_{11\text{e}}$. The best PM region ($\lambda_{\text{P}_2} = 1544.85$ nm) and exemplary signal and idler wavelengths for $\lambda_{\text{P}_2} = 1544.7$ nm are marked.

Two possible operating points are marked in the plot, where neither signal nor idler cross a pump when S is moved from S_1 to S_2 . In this example, input wavelengths are $\text{P}_2 = 1544.7$ nm, $\text{S}_1 = 1545$ nm and $\text{S}_2 = 1546$ nm and the idler will be generated with high efficiency between $\text{I}_1 = 1538.3$ nm and $\text{I}_2 = 1539.3$ nm. The small discrepancy in wavelengths and tilt of the “arms” between our Fig. 3.2 and Fig. 2 in [15] can be attributed to the fact that fiber parameters of [15] are not fully available.

Having introduced Fig. 3.2, we can explain one last constraint of our optimization. To ensure that PM is not too sensitive to variations of pump 2’s wavelength, we only count regions of good PM for B_{FWM} where pump 2 can vary at least 50 GHz (roughly 0.4 nm). In other words, only those parts of the red region in the figure are considered for B_{FWM} , which are at least 0.4 nm high. Hence, the best PM region (marked in the figure) would not be considered by the optimization process, since its height is only about 0.1 nm. We only included it (by temporarily lowering the requirement to 0.1 nm) to be able to compare our results to [15].

The implementation of our PM optimization algorithm is based on Fig. 3.2. For all combinations of considered mode assignments and pump 1 wavelengths (usually 400 values uniformly sampled from low O-band to high U-band), such an image is generated in memory and the best achievable B_{FWM} is computed. For that, the algorithm computes B_{FWM} in each line of the image, incorporating all constraints mentioned above.

For example, 2 nm are subtracted if the signal crosses a pump in the region (e.g. P_2 in the marked optimum in Fig. 3.2). The highest bandwidth for this image is then stored. After the process is repeated for all images, the mode assignments and wavelengths which result in the highest B_{FWM} are returned.

One caveat for optimizing *fibers* (but not NR waveguides) is explained in Appendix A.4.4.

3.1.1. Filtering Mode Combinations

The wavelength-independent coefficient β_0 in Eq. (2.18) is subject to high fluctuations along the propagation in fibers [14]. It tends to disturb PM and inhibit a buildup of the idler in multi-modal FWM. Therefore, most of the times we assign modes (m) , (o) , (p) , (q) in Eqs. (2.61) and (2.62) in a way, that the $\beta_0^{(X)}$ terms cancel out. It requires further studies to determine if this assumption also holds for NR waveguides with propagation distances in the range of centimeters. However, this was not subject of the thesis. With this assumption, three possibilities per FWM process remain:

$$\text{BS} \begin{cases} \Delta\beta = +\beta^{(A)}(\omega_{P_1}) + \beta^{(A)}(\omega_S) - \beta^{(A)}(\omega_{P_2}) - \beta^{(A)}(\omega_I) & (3.1) \\ \Delta\beta = +\beta^{(B)}(\omega_{P_1}) + \beta^{(A)}(\omega_S) - \beta^{(B)}(\omega_{P_2}) - \beta^{(A)}(\omega_I) & (3.2) \\ \Delta\beta = +\beta^{(B)}(\omega_{P_1}) + \beta^{(A)}(\omega_S) - \beta^{(A)}(\omega_{P_2}) - \beta^{(B)}(\omega_I) & (3.3) \end{cases}$$

$$\text{OPC} \begin{cases} \Delta\beta = +\beta^{(A)}(\omega_{P_1}) - \beta^{(A)}(\omega_S) + \beta^{(A)}(\omega_{P_2}) - \beta^{(A)}(\omega_I) & (3.4) \\ \Delta\beta = +\beta^{(B)}(\omega_{P_1}) - \beta^{(B)}(\omega_S) + \beta^{(A)}(\omega_{P_2}) - \beta^{(A)}(\omega_I) & (3.5) \\ \Delta\beta = +\beta^{(B)}(\omega_{P_1}) - \beta^{(A)}(\omega_S) + \beta^{(A)}(\omega_{P_2}) - \beta^{(B)}(\omega_I) & (3.6) \end{cases}$$

Note how there is always one pair of β in the same mode with opposite sign. This limits multi-modal FWM to using either one mode for all lasers, or two modes with two lasers in each. In Chapter 5, we analyze how FWM with 3 or 4 distinct modes performs, ignoring this restriction.

3.1.2. Graphical Phase Matching

In [14], the authors presented a graphical PM method which works for the processes Eqs. (3.2), (3.3), (3.5) and (3.6). They showed that PM is achieved if the normalized group delays (see Eq. (2.19)) fulfill

$$\tau_g^{(A)}\left(\frac{\omega_1 + \omega_2}{2}\right) = \tau_g^{(B)}\left(\frac{\omega_3 + \omega_4}{2}\right), \quad (3.7)$$

where $\omega_{\{1,2,3,4\}} \in \{\omega_S, \omega_I, \omega_{P_1}, \omega_{P_2}\}$, depending on which of the processes is considered. Or, in words, the group delay of mode (A) , evaluated at the mean frequency of the waves propagating in mode (A) , needs to match the group delay of mode (B) evaluated at the mean frequency of the waves in mode (B) .

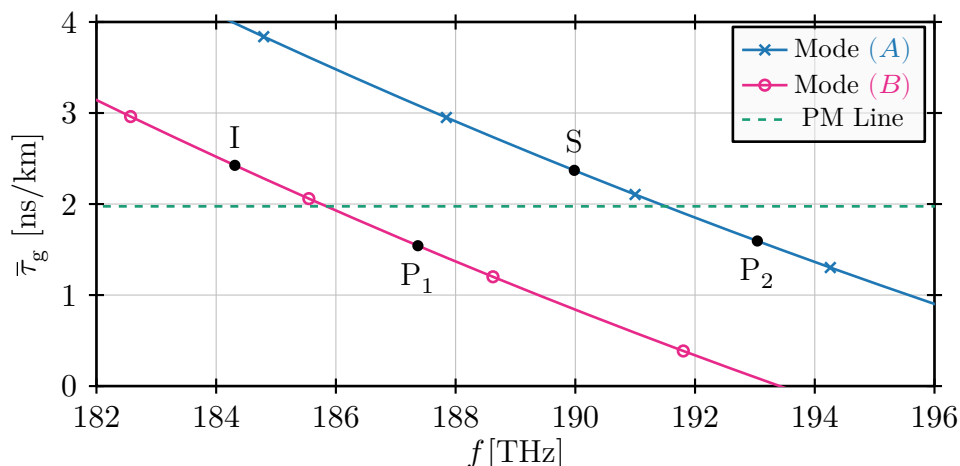


Figure 3.3.: An example of the graphical phase matching approach introduced in Section 3.1.2. A BS process as in Eq. (3.3) is shown.

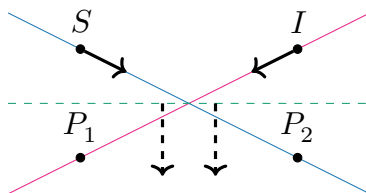


Figure 3.4.: Hypothetical optimal group delay curves leading to broadband intra-band PM for the OPC process. Arrows indicate in which directions signal, idler and the lines with same group delay (see Eq. (3.7)) move.

Consider Fig. 3.3 for an example. The group delay in mode (A) at the mean frequency of idler and pump 1 matches the group delay in mode (B) at the mean frequency of signal and pump 2, highlighted by the green horizontal dashed line (at roughly 2 ns/km).

Since a BS process is depicted, the idler will follow the signal in the same direction if its frequency is changed. Therefore, good PM is maintained if the slopes of the two group delay curves are close to each other, i.e., the two modes have similar dispersion $D^{(A)} \approx D^{(B)}$. This is why the authors in [15] chose a depressed cladding fiber (see Section 2.2.1).

For OPC, group delay curves of the shape shown in Fig. 3.4 would be optimal, since the signal and idler move in opposite directions (see Eq. (2.55)). However, this shape does not exist in NR waveguides and fibers since it requires negative dispersion for one mode and positive for the other mode with same magnitudes. Modes close to cutoff come close to this picture, but the effect is not achieved and PM optimization always returns other (better) configurations.

Hence, numerical optimizations like the one introduced in Section 3.1 need to be used in the general case.

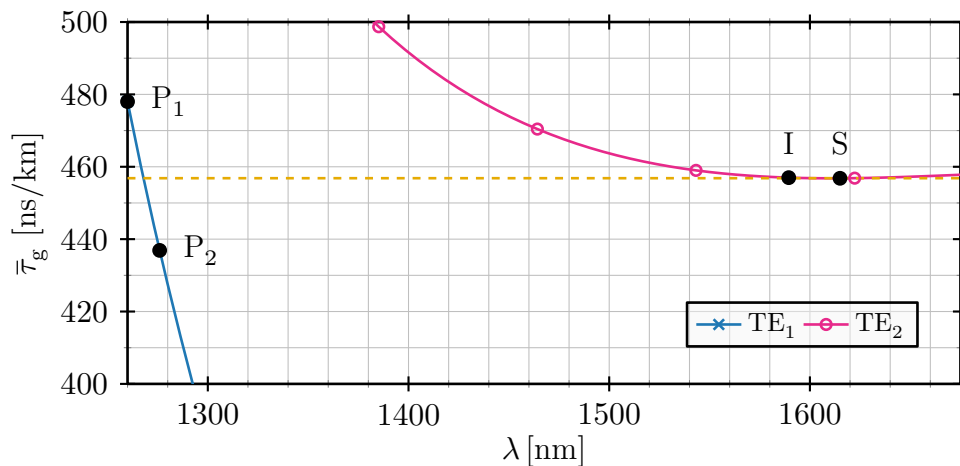


Figure 3.5.: An example of the third kind PM in waveguide 7 (third kind PM) in Table 2.3. The two pumps are in a mode with regular group delay and signal and idler in a mode with low dispersion in the regime of interest.

3.1.3. Different Kinds of Phase Matching

In this short section, we present selected PM constellations which can arise in waveguides with different types of group delay curves. This is not an exhaustive list, we just show three interesting cases.

In the first kind, one mode with a broad low dispersion region is used for all propagating lasers. e.g. TE_3 in Figs. 2.11e and 2.11f. This broad close-to-zero dispersion region is only found in NR waveguides and not in fibers. It can be used for very versatile BS and OPC FWM configurations, due to the vast wavelength region it covers. Note that this differs only slightly from classical singlemode FWM by the fact that it's usually not the fundamental mode TE_0 , but a higher order mode.

The second kind of PM could be called the *classical* approach, since it is commonly used in fiber-based FWM experiments such as in [15] or [14]. This PM type works as the graphical approach in Section 3.1.2. Two waveguide modes with different group delays are used, but the dispersion of both modes is very similar, i.e., the group delay curves have almost the same slope and Eq. (3.7) is fulfilled. This kind of PM works for BS, but not for OPC. When the signal is shifted towards longer wavelengths, the idler will follow (see Eq. (2.54)) and the group delays at the mean wavelengths in both modes both move at similar “speeds”.

The third kind of PM is a combination of the first two kinds and an example is shown in Fig. 3.5, for waveguide 7 (third kind PM) in Table 2.3. One mode has regular group delay and the other mode a region with low dispersion. When the signal is moved, the group delay at mean signal and idler wavelength does not change significantly due to the low dispersion and Eq. (3.7) is fulfilled again. This kind of PM also only works for BS and not for OPC. Further note that this PM process is very sensitive to pump placement and to small variations in waveguide parameters (see [33]).

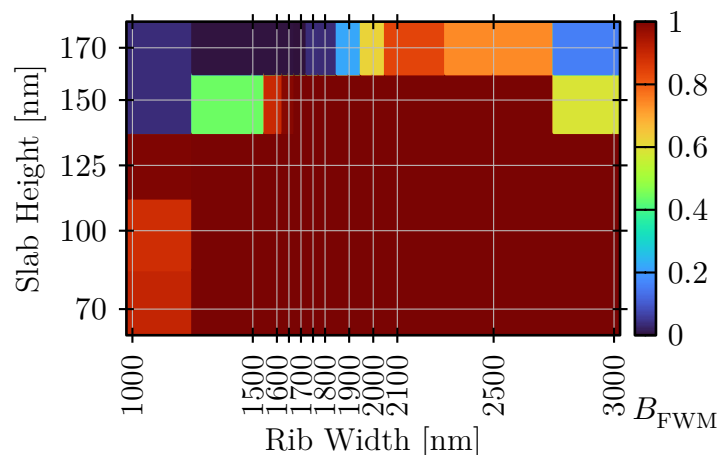


Figure 3.6.: Highest achievable FWM bandwidths for C- to O-band WLC (BS FWM process) in waveguides with different geometries. Two-mode configurations are enforced. All bandwidths are normalized to the C-band’s width.

3.2. Waveguide Geometry Optimization

One of our main goals is to optimize waveguide geometry to achieve maximal FWM bandwidth B_{FWM} . For that, we sweep over dimension parameters of interest and perform the PM explained in Section 3.1 for each combination of values.

For fibers, we usually sweep over core radius r_{core} and trench width w_{trench} (both defined in Fig. 2.4). For NR waveguides, we usually sweep over rib width w_{rib} and slab height h_{slab} (both defined in Fig. 2.7). However, our framework supports sweeping over many more parameters like, e.g., core material or number and size of etched *dips* in the rib (see Fig. 2.8a for the definition of dips).

We presented geometry optimizations of NR waveguides over rib width, slab height, number of dips, dip width and dip depth in [33]. Table 3.1 lists the main results. Each scenario controls three parameters: 1) The FWM process OPC or BS. 2) Either the optimizer was allowed to freely choose from one-mode and two-mode configurations, or it was forced to use two-mode configurations (called “2M”). 3) Signal and idler were enforced to be in certain optical bands, selected from O,S,C and L – according to Fig. 3.1. The two pumps were always free to be placed in the O, S, C and L-bands. We reported all scenarios in Fig. 3.1 for BS. Additionally, we included C- to C-band OPC.

As an example, Fig. 3.6 shows highest achievable C- to O-band WLC bandwidths for enforced two-mode operation (“2M”). It can be seen that many geometries lead to a bandwidth of at least the C-band (which is the maximum of this scenario).

The main conclusion in [33] is that all-optical processing can be achieved with very high bandwidth for all scenarios – most of them even with close-to or maximum possible bandwidth. Only O-to-O-band conversion is limited to 52 nm.

Table 3.1.: Optimization results of our work in [33]. Each scenario defines the FWM process (BS or OPC), the source and target bands and whether multimode operation was enforced (“2M”) or the optimizer was allowed to use one or two modes. The modes in the second column are given in the order pump 1, signal, pump 2, idler. The last column shows the obtained and maximum possible FWM bandwidth for the scenario, where the maximum depends on the width of source and target bands, the FWM process, pump placement and enforced signal to pump separation (5 nm in this case).

Scenario	Modes [TE _x]	w_{rib} [nm]	h_{slab} [nm]	Num. Dips	w_{dip} [nm]	h_{dip} [nm]	B_{FWM} [nm]
BS, O→O	0,1,1,0	3000	70	2	400	150	52 / 95
BS, S→S	2,2,2,2	1500	70	0	200	70	65 / 65
BS, C→C	2,2,2,2	1500	70	0	200	70	29 / 30
BS, L→L	2,2,2,2	1500	70	0	200	70	54 / 55
BS, C→O	1,2,2,1	1500	70	1	300	70	35 / 35
BS, C→S	2,2,2,2	1500	70	0	200	70	35 / 35
BS, C→L	2,2,2,2	1500	70	0	200	70	35 / 35
BS, O→O, 2M	0,1,1,0	3000	70	2	400	150	52 / 95
BS, S→S, 2M	1,2,1,2	2000	70	2	200	150	61 / 65
BS, C→C, 2M	2,1,2,1	1800	70	1	200	150	29 / 30
BS, L→L, 2M	2,1,2,1	1600	70	1	200	120	53 / 55
BS, C→O, 2M	1,2,2,1	1500	70	1	300	70	35 / 35
BS, C→S, 2M	2,1,1,2	1650	100	1	400	70	35 / 35
BS, C→L, 2M	2,1,1,2	2100	100	1	400	70	35 / 35
OPC, C→C	2,2,2,2	1750	70	2	200	70	35 / 35
OPC, C→C, 2M	2,1,1,2	1800	100	1	400	70	19 / 30

Table 3.2.: Geometry parameter search space for a small optimization over dip parameters. Dip parameters are defined in Fig. 2.8a.

Parameter	Considered Values
w_{rib} [nm]	1700
h_{slab} [nm]	72
h_{SOI} [nm]	220
Number of dips	[0, 1, 2]
w_{dip} [nm]	[200, 300, 400]
h_{dip} [nm]	[70, 150]

3.2.1. The Effect of Dips

The second main result in [33] was that dips can greatly influence dispersion properties and hence introduce useful additional degrees of freedom for PM. Dips force the mode fields into different shapes (see e.g. Fig. 2.10) and alter the group delay and dispersion curves in a non-trivial way. Instead of repeating the results of [33], we show a small dip parameter optimization with parameters listed in Table 3.2 for O- to O-band WLC. Here, the optimizer was allowed to freely choose configurations with one or two modes. The achievable FWM bandwidths for each dip configuration are presented in Fig. 3.7.

For this waveguide, the configuration with no dips is able to achieve a bandwidth of roughly 23% of the O-band while the best configuration has two dips and achieves roughly 54% of the O-band. When one dip is etched into the middle of the waveguide, it is best to make it as wide and as deep as possible, while for two dips it is best to etch them as narrow and as shallow as possible.

The group delay curves of the waveguide without dips and the waveguide with highest B_{FWM} are compared in Fig. 3.8. The largest effect is on modes which have significant fractions of power at the dip positions (TE_1 and TE_3) and the effect is stronger for the weakly guided mode TE_3 . The altered TE_3 mode makes it possible to use a configuration with modes TE_2 and TE_3 , while in the case without dips TE_0 and TE_1 are used.

This small simulation highlights the fact that dips really can be beneficial to fine-tune dispersion. Unfortunately it turned out that manufactured waveguides with dips have very high loss and we could not achieve FWM in those waveguides. However, improving the etching process and potentially the coupling of light in- and out of the waveguide could be able to mitigate the effect.

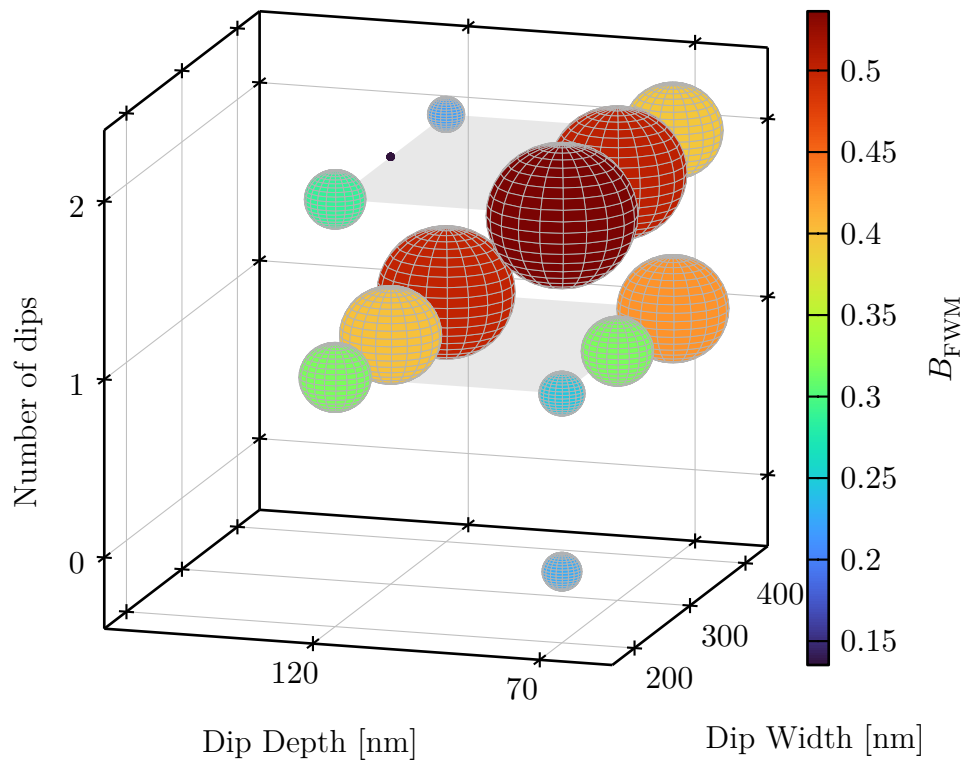


Figure 3.7.: FWM bandwidth for different dip configurations in a waveguide with $w_{\text{rib}} = 1700$ nm and $h_{\text{slab}} = 72$ nm, for O- to O-band WLC. Ball size and ball color both encode the highest achievable B_{FWM} , normalized to the O-band's width.

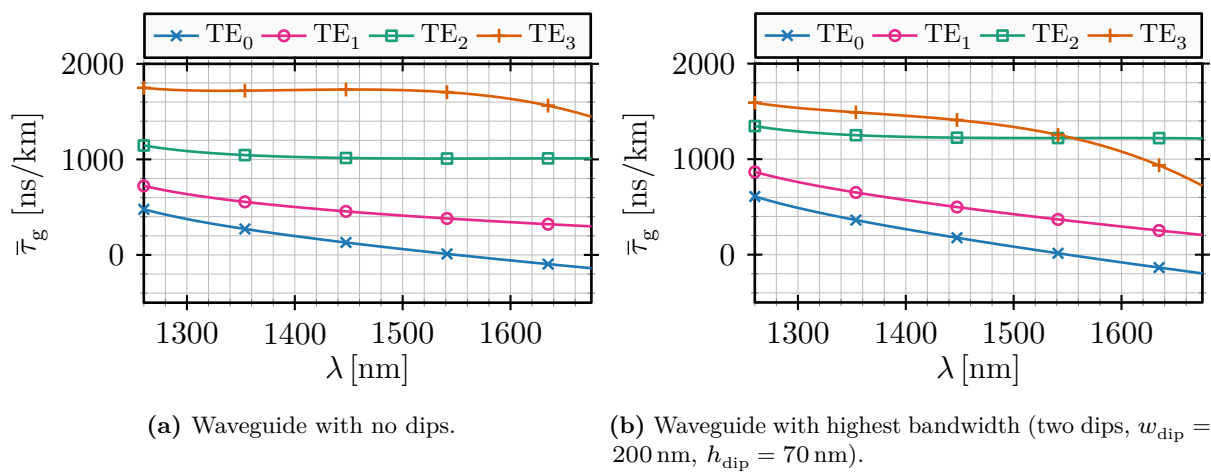


Figure 3.8.: Normalized relative group delays for two waveguides of Fig. 3.7.

4

Frequency Domain Model of Light Propagation in Matter

As explained in [Section 2.4.7](#), the idler power based on [Eq. \(2.65\)](#) does not cover several effects. To be able to predict the idler power with higher accuracy, we developed a [CW](#) frequency domain propagation simulation framework which computes complex amplitudes as the waves propagate along the waveguide. The effects of mode dependent attenuation, linear mode coupling and nonlinear coupling are all considered here.

4.1. Derivation of the Propagation Equations

In general, the material response to light is not instantaneous and the power series expansion of material polarization [Eq. \(2.46\)](#) needs to be generalized to a Volterra series

$$\begin{aligned} \tilde{\mathbf{D}}(t) = \varepsilon_0 \tilde{\mathbf{E}}(t) + \tilde{\mathbf{P}}^{[1]}(t) + \tilde{\mathbf{P}}^{[3]}(t) &= \varepsilon_0 \tilde{\mathbf{E}}(t) + \varepsilon_0 \int_{-\infty}^{\infty} \overset{\leftrightarrow}{\chi}^{[1]}(\tau) \tilde{\mathbf{E}}(t - \tau) d\tau \\ &+ \varepsilon_0 \iiint_{-\infty}^{\infty} \overset{\leftrightarrow}{\chi}^{[3]}(\tau_b, \tau_c, \tau_d) \tilde{\mathbf{E}}(t - \tau_b) \tilde{\mathbf{E}}(t - \tau_c) \tilde{\mathbf{E}}(t - \tau_d) d\tau_b d\tau_c d\tau_d, \end{aligned} \quad (4.1)$$

where $\tilde{\mathbf{P}}^{[1]}$ is responsible for waveguiding and dispersion and $\tilde{\mathbf{P}}^{[3]}$ for third order material nonlinearities. With the Fourier convolution theorem [Eq. \(A.5\)](#), the frequency domain representation of $\tilde{\mathbf{P}}^{[1]}(t)$ is

$$\begin{aligned} \tilde{\mathbf{P}}^{[1]}(f) &= \varepsilon_0 \overset{\leftrightarrow}{\mathbf{X}}^{[1]}(f) \tilde{\mathbf{E}}(f), \\ \overset{\leftrightarrow}{\mathbf{X}}^{[1]}(f) &= \int_{-\infty}^{\infty} \overset{\leftrightarrow}{\chi}^{[1]}(t) e^{-j2\pi ft} dt. \end{aligned} \quad (4.2)$$

To convert $\tilde{\mathbf{P}}^{[3]}(t)$ into the frequency domain, we start with

$$\begin{aligned}\tilde{\mathbf{P}}^{[3]}(f) &= \int_{-\infty}^{\infty} \tilde{\mathbf{P}}^{[3]}(t) e^{-j2\pi ft} dt \\ &= \varepsilon_0 \int_{-\infty}^{\infty} \iiint_{-\infty}^{\infty} \overset{\leftrightarrow}{\chi}^{[3]}(\tau_b, \tau_c, \tau_d) : \tilde{\mathbf{E}}(t - \tau_b) \tilde{\mathbf{E}}(t - \tau_c) \tilde{\mathbf{E}}(t - \tau_d) e^{-j2\pi ft} d\tau_b d\tau_c d\tau_d dt.\end{aligned}\quad (4.3)$$

With the Fourier time shift property Eq. (A.3) we can replace the E-fields with

$$\begin{aligned}\tilde{\mathbf{E}}(t - \tau_b) &= \int_{-\infty}^{\infty} \tilde{\mathbf{E}}(f_b) e^{-j2\pi\tau_b f_b} e^{j2\pi f_b t} df_b \\ \tilde{\mathbf{E}}(t - \tau_c) &= \int_{-\infty}^{\infty} \tilde{\mathbf{E}}(f_c) e^{-j2\pi\tau_c f_c} e^{j2\pi f_c t} df_c \\ \tilde{\mathbf{E}}(t - \tau_d) &= \int_{-\infty}^{\infty} \tilde{\mathbf{E}}(f_d) e^{-j2\pi\tau_d f_d} e^{j2\pi f_d t} df_d.\end{aligned}\quad (4.4)$$

Inserting Eq. (4.4) in Eq. (4.3) and reordering terms leads to

$$\begin{aligned}\tilde{\mathbf{P}}^{[3]}(f) &= \varepsilon_0 \iiint_{-\infty}^{\infty} \iiint_{-\infty}^{\infty} \overset{\leftrightarrow}{\chi}^{[3]}(\tau_b, \tau_c, \tau_d) e^{-j2\pi f_b \tau_b} e^{-j2\pi f_c \tau_c} e^{-j2\pi f_d \tau_d} d\tau_b d\tau_c d\tau_d : \\ &\quad \underbrace{\overset{\leftrightarrow}{\mathbf{X}}^{[3]}(f_b, f_c, f_d)} \\ &\quad : \tilde{\mathbf{E}}(f_b) \tilde{\mathbf{E}}(f_c) \tilde{\mathbf{E}}(f_d) \underbrace{\int_{-\infty}^{\infty} e^{j2\pi(f_b + f_c + f_d)t} e^{-j2\pi ft} dt}_{\delta(f - f_b - f_c - f_d)} df_b df_c df_d \\ &= \varepsilon_0 \iiint_{-\infty}^{\infty} \overset{\leftrightarrow}{\mathbf{X}}^{[3]}(f \leftarrow f_b, f_c, f_d) : \tilde{\mathbf{E}}(f_b) \tilde{\mathbf{E}}(f_c) \tilde{\mathbf{E}}(f_d) * \\ &\quad * \delta(f - f_b - f_c - f_d) df_b df_c df_d.\end{aligned}\quad (4.5)$$

The susceptibility $\overset{\leftrightarrow}{\mathbf{X}}^{[3]}(f \leftarrow f_b, f_c, f_d)$ does not have a direct dependence on f , but since that is the frequency at which the nonlinear material polarization is generated, it is included in the nomenclature. It is nevertheless separated with an arrow to make clear that it depends on f_b , f_c and f_d and is not a parameter of $\overset{\leftrightarrow}{\mathbf{X}}^{[3]}$.

With the susceptibilities in frequency domain at hand, Eq. (4.1) can be written as

$$\tilde{\mathbf{D}}(f) = \varepsilon_0 \tilde{\mathbf{E}}(f) + \overset{\leftrightarrow}{\chi}^{[1]}(f) \tilde{\mathbf{E}}(f) + \tilde{\mathbf{P}}^{[3]}(f) = \varepsilon_0 (\varepsilon'_r \mathbf{1} + \underline{\Delta\varepsilon}_r) \tilde{\mathbf{E}}(f) + \tilde{\mathbf{P}}^{[3]}(f), \quad (4.6)$$

where $\mathbf{1}$ is the identity matrix and we split the permittivity into a waveguiding and dispersion part ε'_r , and a part modeling linear coupling due to waveguide imperfections $\underline{\Delta\varepsilon}_r$.

Note that both, $\varepsilon_r'(x, y)$ and $\underline{\Delta\varepsilon}_r(x, y)$ vary with transversal coordinates x and y .

We heuristically introduce ε_r'' which models mode and frequency dependent linear attenuation and get

$$\widetilde{\mathbf{D}}(f) = \underbrace{\varepsilon_0 \varepsilon_r' \widetilde{\mathbf{E}}(f)}_{\text{Waveguiding \& Dispersion}} - \underbrace{j \varepsilon_0 \varepsilon_r'' \widetilde{\mathbf{E}}(f)}_{\text{Attenuation}} + \underbrace{\varepsilon_0 \underline{\Delta\varepsilon}_r \widetilde{\mathbf{E}}(f)}_{\text{Linear Coupling}} + \underbrace{\widetilde{\mathbf{P}}^{[3]}(f)}_{\text{Nonlinear Coupling}}. \quad (4.7)$$

Rearranging all perturbations into

$$\widetilde{\mathbf{P}}'(f) := -j \varepsilon_0 \varepsilon_r'' \widetilde{\mathbf{E}}(f) + \varepsilon_0 \underline{\Delta\varepsilon}_r \widetilde{\mathbf{E}}(f) + \widetilde{\mathbf{P}}^{[3]}(f) \quad (4.8)$$

yields

$$\widetilde{\mathbf{D}}(f) = \varepsilon_0 \varepsilon_r' \widetilde{\mathbf{E}}(f) + \widetilde{\mathbf{P}}'(f). \quad (4.9)$$

We start again with Maxwell's Eqs. (2.9) to (2.12). Since we operate in frequency domain now, we can replace time derivatives by $j2\pi f = j\omega$ (see Eq. (A.4)). Taking the curl of Eq. (2.11) and using the double curl identity Eq. (2.13) gives

$$\Delta \widetilde{\mathbf{E}}(f) - \nabla (\nabla \cdot \widetilde{\mathbf{E}}(f)) = -\mu_0 \omega^2 \widetilde{\mathbf{D}}(f). \quad (4.10)$$

Inserting Eq. (4.9) for the displacement field in Eq. (2.9) gives

$$\nabla \cdot \widetilde{\mathbf{D}}(f) = \varepsilon_0 \nabla \cdot (\varepsilon_r' \widetilde{\mathbf{E}}(f)) + \nabla \cdot \widetilde{\mathbf{P}}'(f) = \mathbf{0} \quad (4.11)$$

$$\Rightarrow \nabla \cdot \widetilde{\mathbf{E}}(f) = -\frac{\nabla \varepsilon_r'}{\varepsilon_r'} \cdot \widetilde{\mathbf{E}}(f) - \frac{1}{\varepsilon_0 \varepsilon_r'} \nabla \cdot \widetilde{\mathbf{P}}'(f) \quad (4.12)$$

With Eq. (4.9) and Eq. (4.12), Eq. (4.10) becomes

$$\Delta \widetilde{\mathbf{E}}(f) + \nabla \left(\underbrace{\frac{\nabla \varepsilon_r'}{\varepsilon_r'} \cdot \widetilde{\mathbf{E}}(f) + \frac{1}{\varepsilon_0 \varepsilon_r'} \nabla \cdot \widetilde{\mathbf{P}}'(f)}_{\text{«A»}} \right) + k_0^2 \varepsilon_r' \widetilde{\mathbf{E}}(f) = -\mu_0 \omega^2 \widetilde{\mathbf{P}}'(f), \quad (4.13)$$

where we used the free-space wave number $k_0^2 = \mu_0 \varepsilon_0 \omega^2$.

The perturbation $\widetilde{\mathbf{P}}'(f)$ in the displacement field Eq. (4.9) is much smaller than the E-field part and we can use the approximation that $\widetilde{\mathbf{P}}'(f)$ does not alter mode fields. Using this perturbation approach in Eq. (4.11), we get

$$\nabla \cdot \widetilde{\mathbf{P}}'(f) = \mathbf{0}. \quad (4.14)$$

Hence, the part of Eq. (4.13) marked with «A» vanishes. Transforming the E-field model Eq. (2.17) into frequency domain

$$\widetilde{\mathbf{E}}(f) = \frac{1}{2} \sum_{a \in \mathcal{S}} \sum_{(m) \in \mathcal{M}} \widehat{E}_a^{(m)}(z) \Psi_a^{(m)}(x, y) e^{-j\beta_a^{(m)} z} \delta(f - f_a) + \text{c.c.} \quad (4.15)$$

and inserting it into Eq. (4.13), we can evaluate the x , y and z components.

Since all operations are linear (we deal with nonlinearity later and keep it hidden in $\tilde{\mathbf{P}}'(f)$ for now), we can take out the summations over frequencies and modes. After some calculus and algebra and the assumption $\frac{\partial \varepsilon'_r}{\partial z} \approx 0$, the equation for the x component is

$$\begin{aligned} & \frac{1}{2} \sum_{a \in \mathcal{S}} \sum_{(m) \in \mathcal{M}} \left\{ (\partial_x^2 + \partial_y^2) (\Psi_{x,a}^{(m)}) + \left(k_0^2 \varepsilon'_r - \beta_a^{(m)2} \right) \Psi_{x,a}^{(m)} \right. \\ & \left. + \partial_x \left[\frac{1}{\varepsilon'_r} (\Psi_{x,a}^{(m)} \partial_x \varepsilon'_r + \Psi_{y,a}^{(m)} \partial_y \varepsilon'_r) \right] \right\} \hat{E}_a^{(m)} e^{-j\beta_a^{(m)} z} \delta(f - f_a) \\ & + \left(\frac{d^2 \hat{E}_a^{(m)}}{dz^2} - 2j\beta_a^{(m)} \frac{d\hat{E}_a^{(m)}}{dz} \right) \Psi_{x,a}^{(m)} e^{-j\beta_a^{(m)} z} \delta(f - f_a) + \text{c.c.} = -\mu_0 \omega^2 \tilde{\mathbf{P}}'_x(f). \end{aligned} \quad (4.16)$$

Since the field amplitude $\hat{E}_a^{(m)}(z)$ only changes due to the perturbations in $\tilde{\mathbf{P}}'(f)$, all addends with $\frac{d\hat{E}}{dz}$ (marked **green**) vanish in the homogeneous equation ($\tilde{\mathbf{P}}'(f) = \mathbf{0}$). Due to mode orthogonality, this is valid for all summands in Eq. (4.16). Based on the assumption that $\tilde{\mathbf{P}}'(f)$ does not alter Ψ , this also has to hold for $\tilde{\mathbf{P}}'(f) \neq \mathbf{0}$ and the parts marked **red** are always zero. The equation for the y component is obtained by simply switching x and y indices in Eq. (4.16) after removing the **red** parts. The z component is slightly different, but with the slowly varying wave approximation $|\partial_z \hat{E}_a^{(m)}| \ll |\beta_a^{(m)} \hat{E}_a^{(m)}|$, the result is the same as switching x and z indices in Eq. (4.16) after removing the **red** parts. With the second slowly varying wave approximation $|\frac{d^2 \hat{E}_a^{(m)}}{dz^2}| \ll |2\beta_a^{(m)} \frac{d\hat{E}_a^{(m)}}{dz}|$, we get the vectorial equation

$$\frac{1}{2} \sum_{a \in \mathcal{S}} \sum_{(m) \in \mathcal{M}} -2j\beta_a^{(m)} \frac{d\hat{E}_a^{(m)}}{dz} \Psi_a^{(m)} e^{-j\beta_a^{(m)} z} \delta(f - f_a) + \text{c.c.} = -\mu_0 \omega^2 \tilde{\mathbf{P}}'(f). \quad (4.17)$$

The next step is inserting the E-field model Eq. (4.15) into the third order nonlinearity Eq. (4.5):

$$\begin{aligned} \tilde{\mathbf{P}}^{[3]}(f) &= \varepsilon_0 \iiint_{-\infty}^{\infty} \hat{\mathbf{X}}^{[3]}(f \leftarrow f_b, f_c, f_d): \\ & \left(\frac{1}{2} \sum_{b' \in \mathcal{S}} \sum_{(o) \in \mathcal{M}} \hat{E}_{b'}^{(o)} \Psi_{b'}^{(o)} e^{-j\beta_{b'}^{(o)} z} \delta(f_b - f_{b'}) + \text{c.c.} \right) \\ & \left(\frac{1}{2} \sum_{c' \in \mathcal{S}} \sum_{(p) \in \mathcal{M}} \hat{E}_{c'}^{(p)} \Psi_{c'}^{(p)} e^{-j\beta_{c'}^{(p)} z} \delta(f_c - f_{c'}) + \text{c.c.} \right) \\ & \left(\frac{1}{2} \sum_{d' \in \mathcal{S}} \sum_{(q) \in \mathcal{M}} \hat{E}_{d'}^{(q)} \Psi_{d'}^{(q)} e^{-j\beta_{d'}^{(q)} z} \delta(f_d - f_{d'}) + \text{c.c.} \right) \\ & * \delta(f - f_b - f_c - f_d) df_b df_c df_d. \end{aligned} \quad (4.18)$$

We dropped the (z) and (x, y) arguments of $\hat{E}(z)$ and $\Psi(x, y)$ for brevity and changed to primed indices for the summations, since they are distinct from the integration indices.

Taking out the summations and defining the terms

$$\mathcal{J}_{b'}^{(o)} = \hat{E}_{b'}^{(o)} \Psi_{b'}^{(o)} e^{-j\beta_{b'}^{(o)} z} \delta(f_b - f_{b'}) \quad (4.19)$$

$$\mathcal{J}_{c'}^{(p)} = \hat{E}_{c'}^{(p)} \Psi_{c'}^{(p)} e^{-j\beta_{c'}^{(p)} z} \delta(f_c - f_{c'}) \quad (4.20)$$

$$\mathcal{J}_{d'}^{(q)} = \hat{E}_{d'}^{(q)} \Psi_{d'}^{(q)} e^{-j\beta_{d'}^{(q)} z} \delta(f_d - f_{d'}), \quad (4.21)$$

we can rewrite Eq. (4.18) as

$$\begin{aligned} \tilde{\mathcal{P}}^{[3]}(f) = & \frac{1}{8} \varepsilon_0 \sum_{\substack{b', c', d' \\ \in \mathcal{S}}} \sum_{\substack{(o), (p), (q) \\ \in \mathcal{M}}} \iiint_{-\infty}^{\infty} \vec{\mathcal{X}}^{[3]}(f \leftarrow f_b, f_c, f_d) : \left[\mathcal{J}_{b'}^{(o)} \mathcal{J}_{c'}^{(p)} \mathcal{J}_{d'}^{(q)} + \right. \\ & + \mathcal{J}_{b'}^{(o)} \mathcal{J}_{c'}^{(p)} (\mathcal{J}_{d'}^{(q)})^* + \mathcal{J}_{b'}^{(o)} (\mathcal{J}_{c'}^{(p)})^* \mathcal{J}_{d'}^{(q)} + \mathcal{J}_{b'}^{(o)} (\mathcal{J}_{c'}^{(p)})^* (\mathcal{J}_{d'}^{(q)})^* + \\ & + (\mathcal{J}_{b'}^{(o)})^* \mathcal{J}_{c'}^{(p)} \mathcal{J}_{d'}^{(q)} + (\mathcal{J}_{b'}^{(o)})^* \mathcal{J}_{c'}^{(p)} (\mathcal{J}_{d'}^{(q)})^* + (\mathcal{J}_{b'}^{(o)})^* (\mathcal{J}_{c'}^{(p)})^* \mathcal{J}_{d'}^{(q)} + \\ & \left. + (\mathcal{J}_{b'}^{(o)})^* (\mathcal{J}_{c'}^{(p)})^* (\mathcal{J}_{d'}^{(q)})^* \right] \delta(f - f_b - f_c - f_d) df_b df_c df_d. \end{aligned} \quad (4.22)$$

The terms of interest have exactly one phase conjugation and are marked with a blue background. These nonlinear products have two positive and one negative frequency component, leading to idlers with wavelengths in the vicinity of the input fields. Expanding the $\mathcal{J}_{b'}^{(o)} \mathcal{J}_{c'}^{(p)} (\mathcal{J}_{d'}^{(q)})^*$ term gives

$$\begin{aligned} \tilde{\mathcal{P}}^{[3]}(f) = & \frac{1}{8} \varepsilon_0 \sum_{\substack{b', c', d' \\ \in \mathcal{S}}} \sum_{\substack{(o), (p), (q) \\ \in \mathcal{M}}} \iiint_{-\infty}^{\infty} \vec{\mathcal{X}}^{[3]}(f \leftarrow f_b, f_c, f_d) : \left[\Psi_{b'}^{(o)} \Psi_{c'}^{(p)} (\Psi_{d'}^{(q)})^* \right. \\ & * \hat{E}_{b'}^{(o)} \hat{E}_{c'}^{(p)} (\hat{E}_{d'}^{(q)})^* * e^{-j(\beta_{b'}^{(o)} + \beta_{c'}^{(p)} - \beta_{d'}^{(q)}) z} \delta(f_b - f_{b'}) \delta(f_c - f_{c'}) \delta(f_d + f_{d'}) + \\ & + \mathcal{J}_{b'}^{(o)} (\mathcal{J}_{c'}^{(p)})^* \mathcal{J}_{d'}^{(q)} + (\mathcal{J}_{b'}^{(o)})^* \mathcal{J}_{c'}^{(p)} \mathcal{J}_{d'}^{(q)} + \mathcal{J}_{b'}^{(o)} \mathcal{J}_{c'}^{(p)} \mathcal{J}_{d'}^{(q)} + \dots \left. \right] * \\ & * \delta(f - f_b - f_c - f_d) df_b df_c df_d, \end{aligned} \quad (4.23)$$

where all terms with more than one complex conjugation are hidden in the ellipsis.

Now we can apply the three integrals to the terms independently to obtain

$$\begin{aligned} \tilde{\mathcal{P}}^{[3]}(f) = & \frac{3}{8} \varepsilon_0 \sum_{\substack{b, c, d \\ \in \mathcal{S}}} \sum_{\substack{(o), (p), (q) \\ \in \mathcal{M}}} \vec{\mathcal{X}}^{[3]}(f \leftarrow f_b, f_c, -f_d) : \Psi_b^{(o)} \Psi_c^{(p)} (\Psi_d^{(q)})^* * \\ & * \hat{E}_b^{(o)} \hat{E}_c^{(p)} (\hat{E}_d^{(q)})^* e^{-j(\beta_b^{(o)} + \beta_c^{(p)} - \beta_d^{(q)}) z} \delta(f - f_b - f_c + f_d) \\ & + \frac{1}{8} \varepsilon_0 \sum_{\substack{b, c, d \\ \in \mathcal{S}}} \sum_{\substack{(o), (p), (q) \\ \in \mathcal{M}}} \vec{\mathcal{X}}^{[3]}(f \leftarrow f_b, f_c, f_d) : \Psi_b^{(o)} \Psi_c^{(p)} \Psi_d^{(q)} * \\ & * \hat{E}_b^{(o)} \hat{E}_c^{(p)} \hat{E}_d^{(q)} e^{-j(\beta_b^{(o)} + \beta_c^{(p)} + \beta_d^{(q)}) z} \delta(f - f_b - f_c - f_d) \\ & + \dots \end{aligned} \quad (4.24)$$

We made use of the fact that the three terms $\mathcal{T}_{b'}^{(o)} \mathcal{T}_{c'}^{(p)} (\mathcal{T}_{d'}^{(q)})^*$, $\mathcal{T}_{b'}^{(o)} (\mathcal{T}_{c'}^{(p)})^* \mathcal{T}_{d'}^{(q)}$ and $(\mathcal{T}_{b'}^{(o)})^* \mathcal{T}_{c'}^{(p)} \mathcal{T}_{d'}^{(q)}$ are equivalent under permutation of the indices (hence the new factor 3). The ellipsis still captures terms with more than one complex conjugation and we also included the expansion of $\mathcal{T}_{b'}^{(o)} \mathcal{T}_{c'}^{(p)} \mathcal{T}_{d'}^{(q)}$ for clarity. We further removed the primes from b' , c' and d' after the integration, since there is only one set of indices left.

We now insert the E-Field model Eq. (4.15) into the perturbation term Eq. (4.8) to obtain

$$\begin{aligned} \tilde{\mathcal{P}}'(f) = & -\frac{1}{2} \sum_{a'' \in \mathcal{S}} \sum_{(o'') \in \mathcal{M}} j \varepsilon_0 \varepsilon_{r,a''}'' \hat{E}_{a''}^{(o'')} \Psi_{a''}^{(o'')} e^{-j\beta_{a''}^{(o'')} z} \delta(f - f_{a''}) + \text{c.c.} \\ & + \frac{1}{2} \sum_{a' \in \mathcal{S}} \sum_{(o') \in \mathcal{M}} \varepsilon_0 \underline{\Delta} \varepsilon_r \Psi_{a'}^{(o')} \hat{E}_{a'}^{(o')} e^{-j\beta_{a'}^{(o')} z} \delta(f - f_{a'}) + \text{c.c.} \\ & + \tilde{\mathcal{P}}^{[3]}(f), \end{aligned} \quad (4.25)$$

where we made sure to introduce unique summation indices distinguished by primes. Now we can insert Eq. (4.24) and Eq. (4.25) into Eq. (4.17) to obtain

$$\begin{aligned} \text{«A»} & \left\{ \frac{1}{2} \sum_{a \in \mathcal{S}} \sum_{(m) \in \mathcal{M}} -2j\beta_a^{(m)} \frac{d\hat{E}_a^{(m)}}{dz} \Psi_a^{(m)} e^{-j\beta_a^{(m)} z} \delta(f - f_a) + \text{c.c.} = \right. \\ \text{«B»} & \left\{ + \frac{1}{2} \sum_{a'' \in \mathcal{S}} \sum_{(o'') \in \mathcal{M}} j k_0^2 \varepsilon_{r,a''}'' \hat{E}_{a''}^{(o'')} \Psi_{a''}^{(o'')} e^{-j\beta_{a''}^{(o'')} z} \delta(f - f_{a''}) + \text{c.c.} \right. \\ \text{«C»} & \left\{ - \frac{1}{2} \sum_{a' \in \mathcal{S}} \sum_{(o') \in \mathcal{M}} k_0^2 \underline{\Delta} \varepsilon_r \Psi_{a'}^{(o')} \hat{E}_{a'}^{(o')} e^{-j\beta_{a'}^{(o')} z} \delta(f - f_{a'}) + \text{c.c.} \right. \\ \text{«D»} & \left\{ - \frac{3}{8} \sum_{\substack{b,c,d \in \mathcal{S} \\ (o),(p),(q) \in \mathcal{M}}} k_0^2 \vec{\mathcal{X}}^{[3]}(f \leftarrow f_b, f_c, -f_d) : \Psi_b^{(o)} \Psi_c^{(p)} (\Psi_d^{(q)})^* \right. \\ & \quad \left. * \hat{E}_b^{(o)} \hat{E}_c^{(p)} (\hat{E}_d^{(q)})^* e^{-j(\beta_b^{(o)} + \beta_c^{(p)} - \beta_d^{(q)}) z} \delta(f - f_b - f_c + f_d) + \dots \right. \end{aligned} \quad (4.26)$$

Our goal is to derive an equation that models a wave at (positive) frequency f_{a^+} and in mode (m^+) , where the $(\cdot)^+$ is used to distinguish frequency and mode indices of the wave of interest from summation indices. We define the normalization factor

$$\mathcal{J}_a^{(m)} = \iint_{-\infty}^{\infty} |\Psi_a^{(m)}(x, y)|^2 dx dy, \quad (4.27)$$

multiply both sides of Eq. (4.26) with $\frac{1}{\mathcal{J}_{a^+}^{(m^+)}} (\Psi_{a^+}^{(m^+)})^*$ and integrate over the transversal plane. Due to mode orthogonality²⁰

$$\frac{1}{\mathcal{J}_a^{(m)}} \iint_{-\infty}^{\infty} (\Psi_a^{(m)})^* \cdot \Psi_a^{(o)} dx dy = \delta_{(m)(o)}, \quad (4.28)$$

all terms not in mode (m^+) vanish in «A» and «B» in Eq. (4.26). Again, we are interested in the wave at frequency f_{a^+} .

²⁰ The Kronecker Delta is defined as $\delta_{ik} = \begin{cases} 1, & i = k \\ 0, & i \neq k \end{cases}$.

To retain only terms at this frequency in «A», «B» and «C», it is enough to keep only terms with $a = a'' = a' = a^+$. However, the nonlinearity in «D» produces terms at various frequencies determined by $\delta(f - f_b - f_c + f_d)$. There are also similar terms hidden in the ellipsis, but they produce waves at either negative frequencies or at the sum of three positive input frequencies, hence never at f_{a^+} . To select nonlinear terms with the desired frequency only, we change the summation to the reduced set

$$\mathcal{S}_a = \{b, c, d : f_{a^+} = f_b + f_c - f_d\}, \quad (4.29)$$

which leads to $\delta(f - f_b - f_c + f_d) = \delta(f - f_{a^+})$. With these changes, we can solve Eq. (4.26) for $\frac{d\hat{E}_{a^+}^{(m^+)}}{dz}$ and get

$$\begin{aligned} \frac{d\hat{E}_{a^+}^{(m^+)}}{dz} = & -\frac{k_0^2}{2\beta_{a^+}^{(m^+)}} \varepsilon_{r,a^+}''^{(m^+)} \hat{E}_{a^+}^{(m^+)} \\ & - j \frac{k_0^2}{2\beta_{a^+}^{(m^+)} \mathcal{J}_{a^+}^{(m^+)}} \sum_{(o') \in \mathcal{M}_{-\infty}} \iint_{-\infty}^{\infty} (\Psi_{a^+}^{(m^+)})^* \cdot (\underline{\Delta\varepsilon}_r \Psi_{a^+}^{(o')}) dx dy \hat{E}_{a^+}^{(o')} e^{-j\overline{\Delta\beta}_a^{(m^+o')} z} \\ & - j \frac{3k_0^2}{8\beta_{a^+}^{(m^+)} \mathcal{J}_{a^+}^{(m^+)}} \sum_{\substack{b,c,d \\ \in \mathcal{S}_a}} \sum_{\substack{(o),(p),(q) \\ \in \mathcal{M}}} \iint_{-\infty}^{\infty} (\Psi_{a^+}^{(m^+)})^* \cdot (\overset{\leftrightarrow}{\mathbf{X}}^{[3]}(f_{a^+ \leftarrow f_b, f_c, -f_d}) : \\ & \quad : \Psi_b^{(o)} \Psi_c^{(p)} (\Psi_d^{(q)})^*) dx dy \hat{E}_b^{(o)} \hat{E}_c^{(p)} (\hat{E}_d^{(q)})^* e^{-j\Delta\beta_{a^+bcd}^{(m^+opq)} z} \end{aligned} \quad (4.30)$$

with linear and nonlinear phase mismatches $\overline{\Delta\beta}$ and $\Delta\beta$ defined in Eqs. (4.32) and (4.33). The last step is to drop the now redundant $(\cdot)^+$ from the indices and restructure some terms to arrive at our final equation

$$\begin{aligned} \frac{d\hat{E}_a^{(m)}}{dz} = & -\frac{\alpha_a^{(m)}}{2} \hat{E}_a^{(m)} \\ & - j \sum_{(o') \in \mathcal{M}} \mathbb{L}_a^{(m^+o')} \hat{E}_a^{(o')} e^{-j\overline{\Delta\beta}_a^{(m^+o')} z} \\ & - j \sum_{\substack{b,c,d \\ \in \mathcal{S}_a}} \sum_{\substack{(o),(p),(q) \\ \in \mathcal{M}}} \mathbb{N}_{a^+bcd}^{(m^+opq)} \hat{E}_b^{(o)} \hat{E}_c^{(p)} (\hat{E}_d^{(q)})^* e^{-j\Delta\beta_{a^+bcd}^{(m^+opq)} z}. \end{aligned} \quad (4.31)$$

The coefficients in Eq. (4.31) are defined as

$$\overline{\Delta\beta}_a^{(m^+o')} = \beta_a^{(o')} - \beta_a^{(m)} \quad (4.32)$$

$$\Delta\beta_{a^+bcd}^{(m^+opq)} = \beta_b^{(o)} + \beta_c^{(p)} - \beta_d^{(q)} - \beta_a^{(m)} \quad (4.33)$$

$$\alpha_a^{(m)} = \frac{k_0^2}{\beta_a^{(m)}} \varepsilon_{r,a}''^{(m)} \quad (4.34)$$

$$\mathbb{L}_a^{(m^+o')} = \frac{k_0^2}{2\beta_a^{(m)} \mathcal{J}_a^{(m)}} \iint_{-\infty}^{\infty} (\Psi_a^{(m)})^* \cdot (\underline{\Delta\varepsilon}_r \Psi_a^{(o')}) dx dy \quad (4.35)$$

$$\mathbb{N}_{a^+bcd}^{(m^+opq)} = \frac{3k_0^2}{8\beta_a^{(m)} \mathcal{J}_a^{(m)}} \iint_{-\infty}^{\infty} (\Psi_a^{(m)})^* \cdot (\overset{\leftrightarrow}{\mathbf{X}}^{[3]}(f_{a^+ \leftarrow f_b, f_c, -f_d}) : \Psi_b^{(o)} \Psi_c^{(p)} (\Psi_d^{(q)})^*) dx dy. \quad (4.36)$$

The reader might wonder how the phase mismatches defined in Eqs. (2.61) and (2.62) relate to Eq. (4.33). The two can be matched by appropriately selecting modes and frequencies of propagating waves. For example, $\beta^{(p)}(\omega_S)$ in Eq. (2.62) is the term with negative frequency and hence maps to $\beta_d^{(q)}$ in Eq. (4.33).

Equation (4.31) models the amplitude evolution of a wave at frequency f_a and in mode $(m)^{21}$. The first term on the right is responsible for linear attenuation. Usually, α is actually not derived from ε_r'' , but directly inserted based on CW measurements of the waveguide (see Appendix A.1.4 for conversion from dB/km to Np/m needed here). The second line is responsible for linear mode coupling from waves at the same frequency f_a . The third line describes nonlinear coupling among all considered modes and frequencies, including SPM, XPM and FWM. The strength of coupling is determined by \mathbb{L} and \mathbb{N} , while the coupling's oscillation period is determined by $\overline{\Delta\beta}$ and $\Delta\beta$. Our models for $\underline{\Delta\varepsilon}_r$ and $\overleftrightarrow{\mathbf{X}}^{[3]}$ are described in Sections 4.2 and 4.3.

To compute the evolution of waves in a waveguide, a set of these coupled differential equations needs to be numerically integrated for all considered modes, at all input frequencies and at all frequencies which are generated with high efficiency. Our solver is built around the `ode113` ordinary differential equation solver built into `MATLAB`. It is a variable step, variable order Adams-Bashforth-Moulton, Predict–Evaluate–Correct–Evaluate solver of orders 1 to 13 [72]. This means that it adjusts both the step size and the method order when integrating along the waveguide, depending on an error estimate computed in each step.

At the start of the waveguide (for roughly one micrometer), the power of waves with no power at the input increases very quickly. Therefore, the integration step size needs to be very small in that region. Later in the waveguide, the required step size depends on the actual coupling coefficients and phase mismatches, which can also change during propagation (see Section 4.2). Hence, `ode113` is a good choice for our problem.

4.2. Linear Coupling Model

The rib walls of our NR waveguide are created by etching of the SOI chip. This has the side effect that the walls will always have a random roughness. Additionally, the wall roughness varies along the z direction. Two main effects can arise from wall roughness: additional linear attenuation due to coupling into leaky modes and linear mode coupling to other guided modes (see e.g. [73, Chapter 3]).

In our simulation, the first effect is incorporated into the attenuation coefficients $\alpha_a^{(m)}$, where we use measured values.

The second effect needs to be covered by an appropriate choice of $\underline{\Delta\varepsilon}_r$ which determines the linear coupling coefficients \mathbb{L} via the integral in Eq. (4.35). We create random perturbations $\Delta\varepsilon_r$ independently for the left and right rib walls. Figure 4.1 shows $\sqrt{\varepsilon_r' + \Delta\varepsilon_r}$, zoomed at the right rib wall. The refractive index perturbation is zero at almost all positions in the grid and 2.03 or -2.03 at remaining positions (the difference between the silicon core and silica cladding). The sign depends on whether the rib is etched too wide or not wide enough and which rib wall is considered. For example, consider the right rib wall. The sign of $\Delta\varepsilon_r$ is positive, if not enough silicon was etched away and the core extends into the cladding (red peaks pointing right in Fig. 4.1). The sign is negative if too much silicon was etched away (blue peaks pointing left in Fig. 4.1).

²¹ The transversal field profiles Ψ in Eq. (4.35) and Eq. (4.36) are vectors of matrices of grid size. See Appendix A.4.1 for some implementation details.

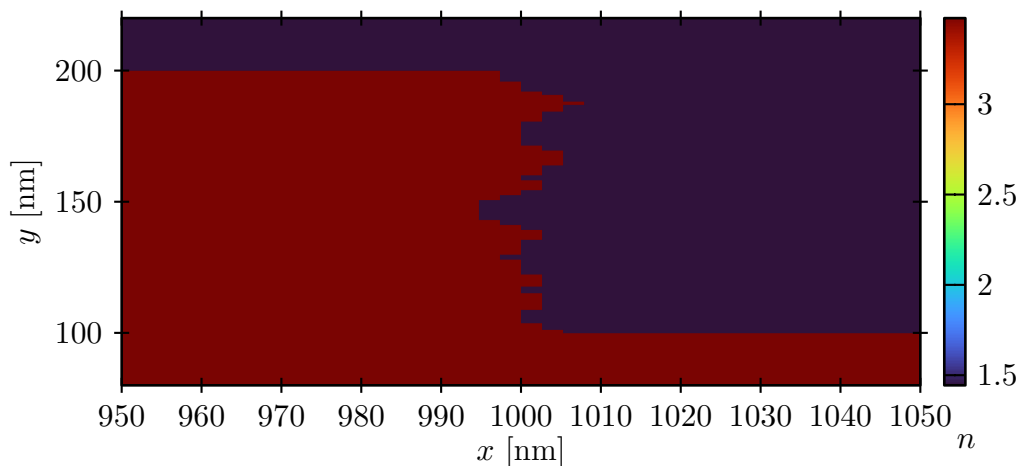


Figure 4.1.: Rib wall with random roughness.

We create the $\underline{\underline{\Delta\epsilon_r}}$ matrix²² as

$$\underline{\underline{\Delta\epsilon_r}} = \Delta\epsilon_r \begin{bmatrix} 1 & \frac{1}{2} & \frac{1}{2} \\ \frac{1}{2} & 1 & \frac{1}{2} \\ \frac{1}{2} & \frac{1}{2} & 1 \end{bmatrix}. \quad (4.37)$$

Since mode coupling is an inherently random process, there is not *the one correct* way to model it. We arbitrarily chose the factor $\frac{1}{2}$ in Eq. (4.37) to model that coupling among different polarizations is weaker. Further, the generation process of the random perturbation $\Delta\epsilon_r$ has some parameters: standard deviation of the roughness, height of vertical blocks and grade of low-pass filtering the roughness function. The standard deviation determines how much the roughness extends into core and cladding. Since it is unphysical that roughness changes too quickly with vertical position y , we firstly use the same random width in vertical blocks of 2 nm height. This explains the steps in the figure which look like quantization. Secondly, we low-pass filter the roughness of the vertical blocks.

The wall roughness changes along the propagation direction of real waveguides with some correlation [74]. However, we used a simplified approach where we simply recompute $\underline{\underline{\Delta\epsilon_r}}$ after every 0.5 mm of propagation.

Finally, we adjusted all these parameters to get coupling strengths comparable to measured values.

4.3. Nonlinear Coupling Model

Nonlinear coupling is determined by the third order susceptibility $\overset{\leftrightarrow}{\chi}^{[3]}$. This tensor has in general 81 components and depends on three frequencies. Since different waveguide materials have different susceptibilities, there is also a dependence on the x and y coordinates. We considered these effects in the model and simulation presented in [36], [39]. However, in this simulation, we chose to greatly simplify the susceptibility and reduce computation time by three orders of magnitude. First of all, we consider $\overset{\leftrightarrow}{\chi}^{[3]}$ to be constant across the waveguide's cross section. To reduce the error we make by this assumption, we limit the integrals in Eq. (4.36) to the rib and slab and thus ignore nonlinear interaction in the surrounding silica cladding. Thankfully, the neglected interaction is small. Most power propagates inside the core and silica has a much weaker nonlinearity than silicon.

²² Note that $\underline{\underline{\Delta\epsilon_r}}$ is actually a matrix of matrices. See Appendix A.4.1 for more details.

Secondly, we ignore the frequency dependence of $\overset{\leftrightarrow}{\chi}^{[3]}$, except for the selection rule Eq. (4.29). This implies that we neglect nonlinear interaction due to the Raman effect and only consider the effect of bound electrons.

Silicon belongs to the point group $m\bar{3}m$, which means only 21 of the 81 components of $\overset{\leftrightarrow}{\chi}^{[3]}$ are nonzero and they have only four independent values [19]. Namely, the value of all $\overset{\leftrightarrow}{\chi}_{iii}^{[3]}$ entries is the same, likewise of all $\overset{\leftrightarrow}{\chi}_{iikk}^{[3]}$ entries, $\overset{\leftrightarrow}{\chi}_{ikik}^{[3]}$ entries and all $\overset{\leftrightarrow}{\chi}_{ikki}^{[3]}$ entries. Here i and k address the x , y and z components of the output and three input field vectors. Symmetry considerations lead to $\overset{\leftrightarrow}{\chi}_{ikki}^{[3]} = \overset{\leftrightarrow}{\chi}_{iikk}^{[3]}$ [19].

We can further use Kleinman's symmetry condition, since our highest considered frequency is the edge of the O-band and thus below the bandgap of silicon. This allows us to approximate $\overset{\leftrightarrow}{\chi}_{iikk}^{[3]} \approx \overset{\leftrightarrow}{\chi}_{ikik}^{[3]}$. For the considered frequency range, experiments [75] have shown that $\overset{\leftrightarrow}{\chi}_{iii}^{[3]} \approx 2.36\overset{\leftrightarrow}{\chi}_{iikk}^{[3]}$. Thus, we can compute all values of $\overset{\leftrightarrow}{\chi}^{[3]}$ by fixing only one parameter. The effective value of $\overset{\leftrightarrow}{\chi}^{[3]}$ is given as [19]

$$\overset{\leftrightarrow}{\chi}_{\text{eff}}^{[3]} = \frac{4}{3}\varepsilon_0 c_0 n^2 n_2 + j \frac{2}{3} \frac{\varepsilon_0 c_0^2 n^2}{\omega} \beta_{\text{TPA}} \quad (4.38)$$

which depends on the nonlinear refractive index n_2 and the two photon absorption coefficient β_{TPA} – both of which can be measured. We used the values $n_2(\text{Si}) = 10 \cdot 10^{-18} \text{ m}^2/\text{W}$ and $\beta_{\text{TPA}}(\text{Si}) = 0.5 \cdot 10^{-11} \text{ m/W}$ from [19, Fig. 6] and [20]. For the NR waveguides in our experiments, $\overset{\leftrightarrow}{\chi}_{iii}^{[3]} \approx \overset{\leftrightarrow}{\chi}_{\text{eff}}^{[3]}/1.1356$ is valid [20, Eq. 1.15].

Combining all these approximations, we can use²³

$$\begin{aligned} \overset{\leftrightarrow}{\chi}_{iii}^{[3]} &= (37.7 + 2.25j) \cdot 10^{-20} \text{ m}^2/\text{V}^2 \\ \overset{\leftrightarrow}{\chi}_{iikk}^{[3]} = \overset{\leftrightarrow}{\chi}_{ikik}^{[3]} = \overset{\leftrightarrow}{\chi}_{ikki}^{[3]} &= (16.0 + 0.95j) \cdot 10^{-20} \text{ m}^2/\text{V}^2 \end{aligned} \quad (4.39)$$

in our simulation for the susceptibility of silicon.

²³ Note that the unit here is m^2/V^2 in contrast to $\text{m}^2/\text{V}^2/\text{s}^2$ in the list of symbols. The difference is that the latter is defined as a time dependent impulse response which needs to be applied with convolution integrals and the values here are simply constants.

Table 4.1.: Simulated propagating waves in the NR waveguide example.

Mode \ Wavelength	1260.00 nm	1265.50 nm	1553.91 nm	1545.62 nm	1063.47 nm
TE ₀	$w_{1,1}$	$w_{1,2}$	$w_{1,3}$	$w_{1,4}$	$w_{1,5}$
TE ₁	P ₁	P ₂	$w_{2,3}$	$w_{2,4}$	$w_{2,5}$
TE ₂	$w_{3,1}$	$w_{3,2}$	S	I _{BS}	I _{OPC}

4.4. Examples of Propagating Waves

We usually simulate typical FWM experiments like those described in Section 2.4.5, where PM results need to be already available. In these experiments, the three input waves (pumps and signal) will interact and generate new waves in all guided waveguide modes and at new frequencies. By linear mode coupling, waves at all frequencies couple into all available modes at the same frequencies. Due to nonlinear interaction, waves at all possible frequency combinations are generated in all available modes. In theory, this means that more and more idlers are generated along the waveguide. However, they are much weaker than the input waves and mostly not phase-matched. Therefore, we limit the simulation by only considering light propagation in a subset of waveguide modes – the input modes, the phase-matched idler’s mode and sometimes one or two more. We further only consider the input frequencies f_{P_1}, f_{P_2}, f_S and idler frequencies $f_{I_{BS}}, f_{I_{OPC}}$. This means that we need to simulate the coupled propagation of $3 \times 5 = 15$ propagating wave amplitudes.

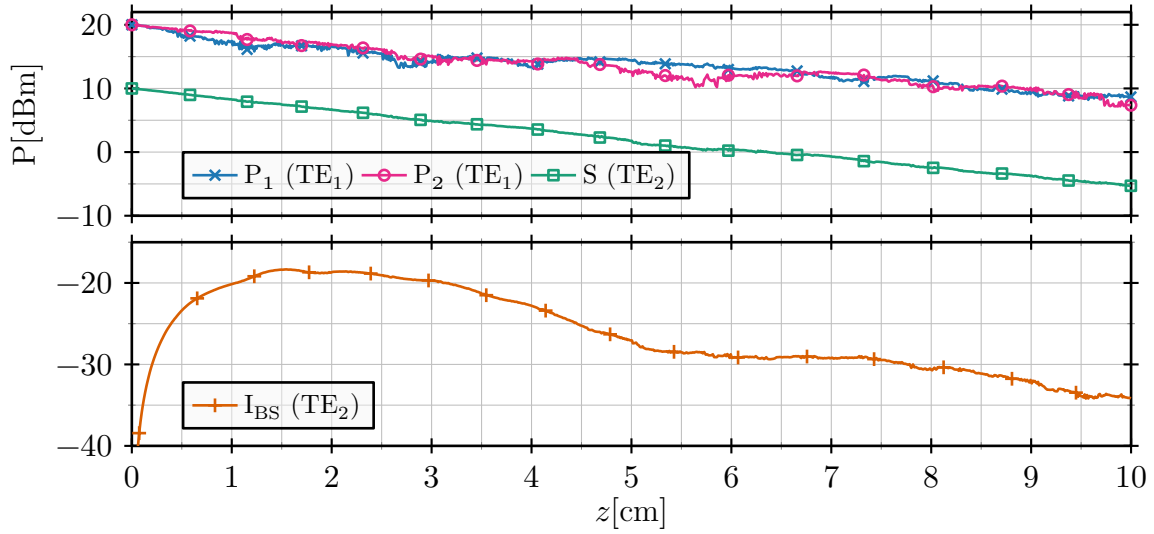
As a first example, Fig. 4.2 shows the power evolution in waveguide 7 (third kind PM) of Table 2.3 with the unusual PM configuration shown in Fig. 3.5. We have summarized the propagating fields in Table 4.1.

The first observable effect in Fig. 4.2a is linear attenuation. We have used $\alpha_{TE_0} = 0.8$ dB/cm, $\alpha_{TE_1} = 1.0$ dB/cm and $\alpha_{TE_2} = 1.5$ dB/cm in the simulation. The figure shows how the pumps in TE₁ are attenuated by 1 dB/cm and the signal by 1.5 dB/cm. The TPA process (nonzero imaginary part of $\vec{\chi}^{[3]}$) leads to an additional attenuation of ≈ 0.2 dB.

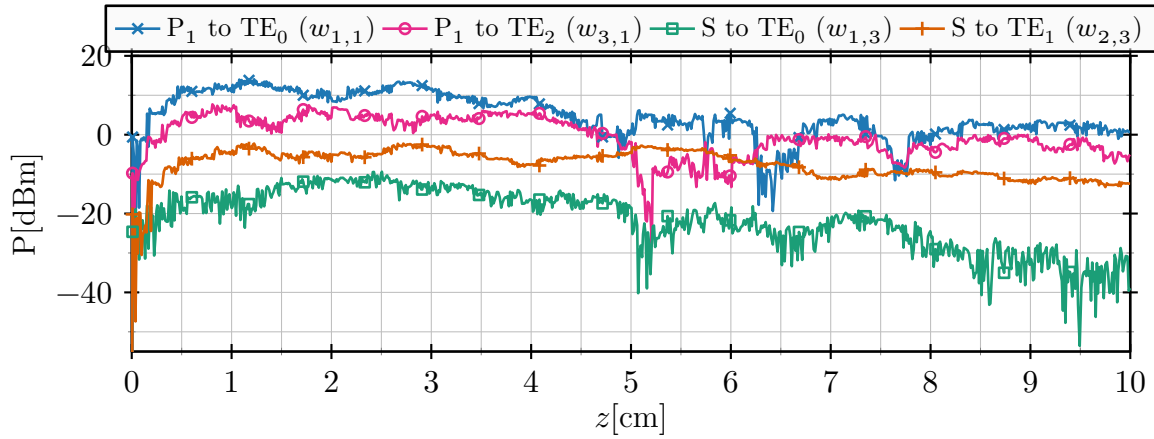
This waveguide has two large dips, which generate severe linear coupling leading to the noise-like shape of the curves. Without or with much weaker linear coupling, the curves would look smooth – compare e.g. with Figs. 5.4 and 6.10. The strong waves generated by linear coupling are shown in Fig. 4.2b, where powers of up to 15 dBm are reached. Figure 4.2c magnifies a small propagation distance of Fig. 4.2b²⁴. Six positions where $\Delta\epsilon_r$ and thus linear coupling coefficients are recomputed are visible (every 0.5 mm, e.g. at 2.652 cm). At these positions, the coupling coefficients don’t only change their magnitude, but sometimes also their sign. This affects the oscillation amplitudes and when the sign changes, the coupling has a phase change of π and the idler power switches from increasing to decreasing or vice versa. For example, wave $w_{2,3}$ (S coupled into TE₁) at 2.652 cm gains in strength by this phase change.

Finally, the lower plot in Fig. 4.2a shows the phase-matched BS idler generated by nonlinear interaction. PM was optimized for a waveguide length of 2 cm, based on the FWM efficiency. The idler power peak in the figure is very close to this predicted point.

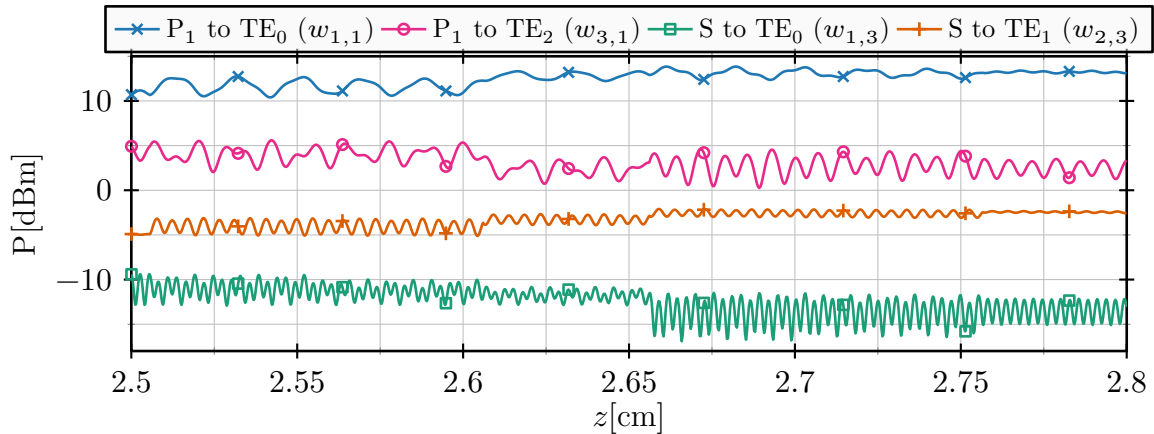
²⁴ Figure 4.2c shows undecimated data, while Figs. 4.2a and 4.2b show only every 50th z sample along the waveguide.



(a) Pumps, signal and idler.



(b) Coupling from pump 1 and from signal into not phase-matched waves.



(c) Zoom on a small section of Subfig. (b).

Figure 4.2.: Simulated power evolution in waveguide 7 (third kind PM) of Table 2.3. PM is of the “third kind” shown in Fig. 3.5.

Table 4.2.: Simulated propagating waves in the optical fiber example. Rows denote in which modes the signals are (mode indices and mode names) and columns denote which frequencies the signals have (frequency indices and wavelength values).

$(m) \setminus a$	1 (1538.00 nm)	2 (1544.85 nm)	3 (1542.85 nm)	4 (1536.02 nm)
1 (HE _{11e})	P ₁	(suppressed)	(suppressed)	I _{BS}
2 (TE ₀₁)	(suppressed)	P ₂	S	(suppressed)

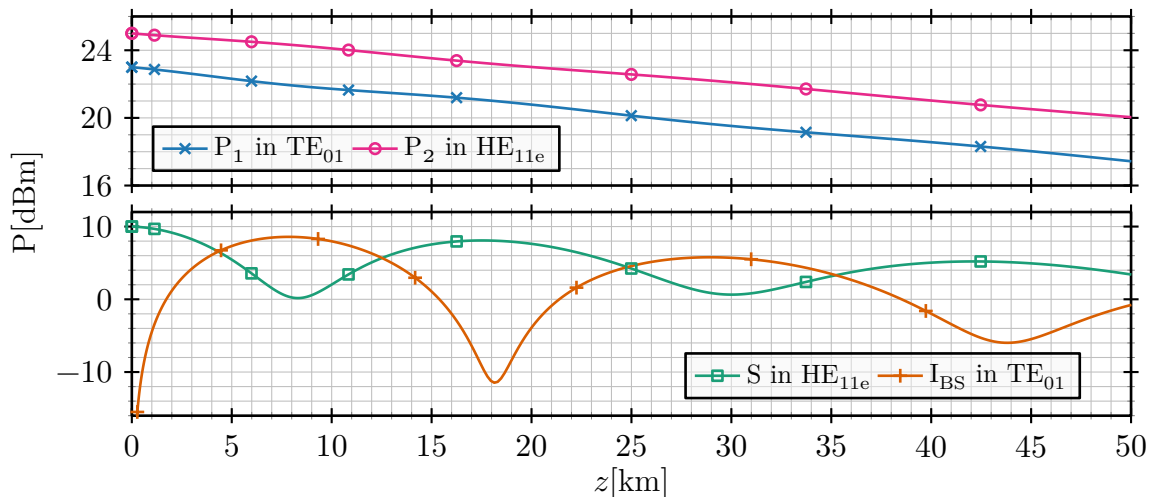


Figure 4.3.: Simulated power evolution of pumps, signal and idler in fiber 3 (depressed cladding) of Table 2.2 with PM according to Fig. 3.2 with wavelengths from Table 4.2.

Another example – this time for an optical fiber – is shown in Fig. 4.3, which is meant to be as close to [15] as possible. Here we simulated fiber 3 (depressed cladding) of Table 2.2 and PM was according to Fig. 3.2, but we used the wavelengths from Table 4.2.

However, we had to make some coarse approximations. The linear coupling oscillation periods are in the mm range and thus very expensive to simulate on the km scale. Nonlinear coupling to non-phase-matched idlers has the same problem, the periods can even be in the μm range. Hence, we only simulated the four waves listed in Table 4.2 and totally neglected linear coupling to be able to simulate kilometers of fiber. We also ignored the small effect of TPA. The last approximation is that core and cladding have the same susceptibility $\chi^{(3)}$. Fortunately, this is not a severe approximation, since both are made of silica with a small fraction of Germanium doping in the core.

If these results are compared to [15], it is clear that the impact of our approximations is too high. While the idler power in [15] is 33 dB below the signal at the output after 4 km, our idler is much stronger at only 16 dB below the signal and we have a strong periodic exchange of power between signal and idler. We still include these results as a reminder that our CW frequency domain approach is not really usable for simulating the long propagation distances in fiber-based experiments. There are other much better suited approaches like the split-step Fourier method applied to the time-domain optical nonlinear Schrödinger equation, which can be derived with many further steps and approximations from Eq. (4.31), e.g. by the Manakov-PMD approach [76].

There is a small residual phase mismatch in Fig. 4.3, but that is not responsible for the cyclic exchange of power between signal and idler. The cause for this effect is analyzed in Appendix A.3.

5

Four-Wave Mixing with Three and Four Modes

Usually, FWM experiments are performed with either all four waves in one mode, or with placing two waves in one mode and the remaining two in another mode (as explained in Section 3.1.2). We call these one-mode four-wave mixing (1-FWM) and two-mode four-wave mixing (2-FWM), respectively. In this chapter, we explore the feasibility of FWM when three or four modes are used and call it three-mode four-wave mixing (3-FWM) and four-mode four-wave mixing (4-FWM), respectively. The principle of multi-mode FWM was already shown in Fig. 2.23, in this chapter we simply make use of the freedom to choose up to four different modes for P_1 , P_2 , S and I. There is no way to cancel β_0 terms with more than two modes and thus we ignore the limitation in Section 3.1.1 to allow for a fair comparison between 1-FWM, 2-FWM, 3-FWM and 4-FWM. Furthermore, we allow all lasers to be in the O-, E-, S-, C-, L and U-bands (1260–1675 nm or 179–238 THz) without any limitation and don't restrict FWM to *useful* configurations (e.g., wavelength conversion from C- to O-band, etc.) – in contrast to the results of our work [33] presented in Section 3.2.

The extension of all-optical signal processing to more than two modes could potentially be beneficial in future SDM networks, when signals from different fibers and modes need to be all-optically multiplexed and processed. This kind of multiplexing can be realized by all-optical WLC based on FWM. Such experiments (using 1-FWM or 2-FWM, we never saw 3-FWM or 4-FWM in literature) are commonly performed with fibers or NR waveguides as nonlinear interaction medium, see for example [14], [16]. Hence, we consider graded index depressed cladding FMFs and NR silicon waveguides for the FWM analysis in this chapter. We compute and compare FWM bandwidths B_{FWM} and nonlinearity parameters γ of FWM configurations with one to four modes.

This chapter is based on our work [37].

Table 5.1.: Geometry values considered for optimizations.

Parameter	Values	Number of Values
Few-Mode Fibers		
r_{core}	6–40 μm	18
w_{trench}	{0, 0.25, 0.5, 1, 2, 4, 8} μm	7
r_{clad}	$r_{\text{core}} + w_{\text{trench}} + 10 \mu\text{m}$	-
Nano-Rib Waveguides		
w_{rib}	1000–3000 nm	20
h_{slab}	70–180 nm	12
h_{SOI}	220 nm	1

5.1. Waveguide Geometry and Phase Matching

The geometry values we used for optimizations in this chapter are listed in Table 5.1. We always considered all guided modes of the sets $\{\text{HE}_{11e}, \text{HE}_{21e}, \text{HE}_{31e}, \text{HE}_{12e}\}$ for fibers and $\{\text{TE}_0, \text{TE}_1, \text{TE}_2, \text{TE}_3\}$ for NR waveguides.

We optimized the geometry of both FMFs and NR waveguides with the procedure described in Section 3.2, repeating the optimization for 1-FWM, 2-FWM, 3-FWM and 4-FWM. Figure 5.1 shows the best achievable FWM bandwidths B_{FWM} . On the left, Figs. 5.1a, 5.1c and 5.1e show results for FMFs and on the right, Figs. 5.1b, 5.1d and 5.1f for NR waveguides. The first row shows 1-FWM, the second row 2-FWM and the third row 3-FWM. The bandwidths for 4-FWM are so low in both waveguides that we did not include them. Therefore, we ignore 4-FWM in the rest of this chapter with the conclusion that it is unusable due to infeasible PM.

The optimizations for FMFs were performed with only 10 m fiber length to be able to cope with the large searched bandwidth, which would need much more simulation time otherwise (see Appendix A.4.4). In reality, the lengths need to be in the range of several hundred meters up to some kilometers to build up sufficient idler powers (see Fig. 4.3)²⁵.

This means that FWM bandwidths of FMFs are much lower in reality than shown here (see, e.g., [15] and note that length reduces bandwidth in Eq. (2.63)). Our results in this chapter for FMFs are therefore not comparable to our results for NR waveguides. This is not a problem, however, since our goal is to compare FWM with different numbers of modes, among the *same type* of waveguides.

From Figs. 5.1a, 5.1c and 5.1e, one can conclude that FWM with one, two and three modes gives roughly the same maximal FWM bandwidth in FMFs. However, note that fibers with huge cores are needed to achieve high B_{FWM} in 3-FWM. To understand the reason, compare the group delays of fibers 2 (graded index) and 4 (large core) in Table 2.2, shown in Fig. 2.6c and Fig. 2.6g, respectively. Due to the large core of the latter, all the considered mode groups have very similar group delays and the process effectively becomes 1-FWM for any number of used modes.

²⁵ Even though the idler power in that section was way off from reality, the approximations did not affect the effect of PM. The fact that the idler power needs a long distance in fibers is still valid and is caused by the orders of magnitude lower nonlinearity and larger core size (compared to NR waveguides).

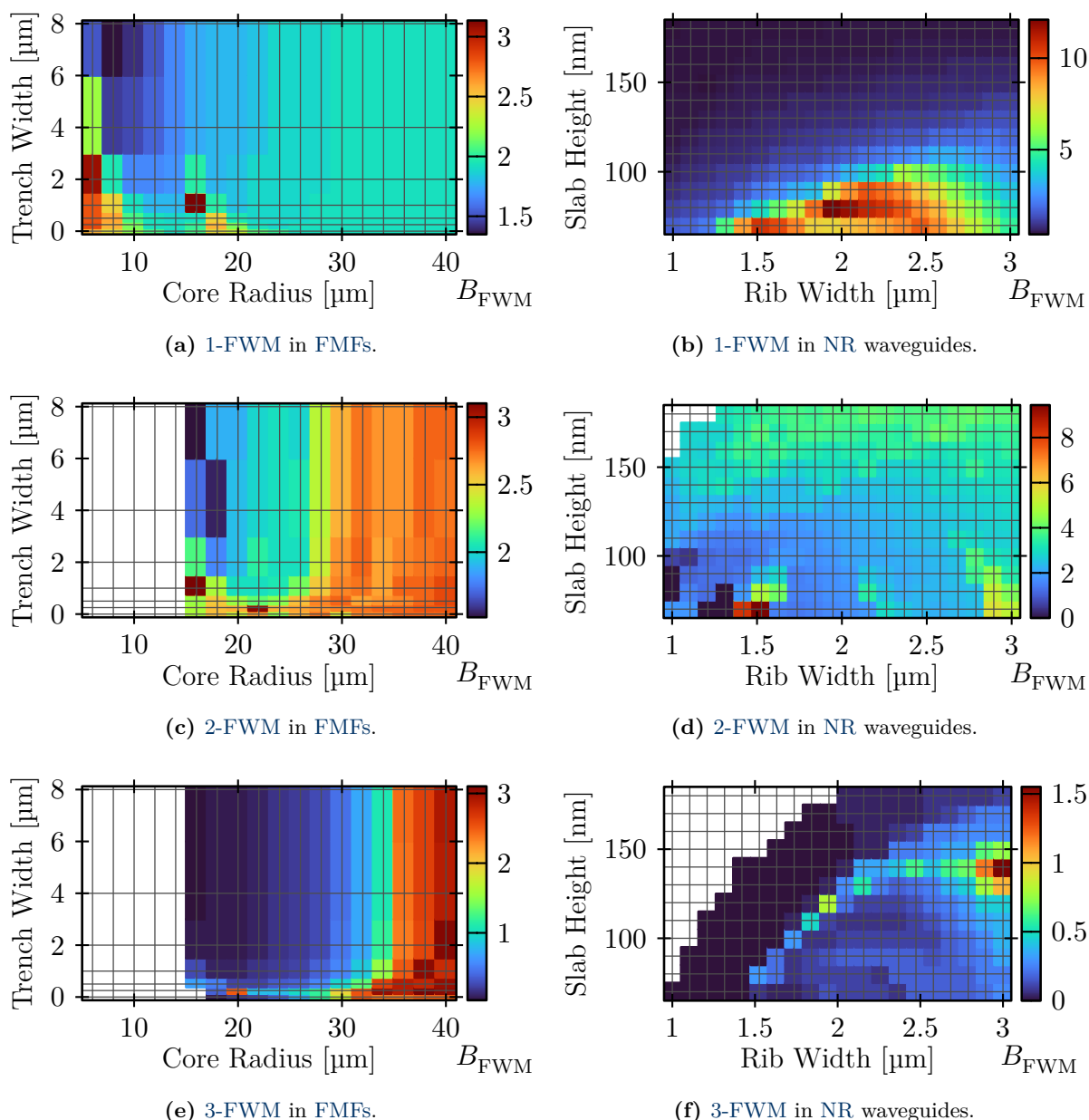


Figure 5.1.: Highest achievable FWM bandwidths for FMFs and NR waveguides with different geometries. All normalized to multiples of the C-band’s frequency range. Waveguides in white areas don’t support enough guided modes.

The two best waveguides in Fig. 5.1a use the first kind of PM from Section 3.1.3 (a broad zero dispersion region of one mode), allowing for the high FWM bandwidths.

For NR waveguides, comparing Figs. 5.1b, 5.1d and 5.1f reveals that increasing the number of utilized modes in the FWM process decreases FWM bandwidths. Here, larger cores also lead to approaching group delay curves (similar to fibers with small and large cores), but the difference stays much larger and the process does not effectively become 1-FWM for the geometries simulated here. The difference in group delay curve shapes and magnitudes in Figs. 2.6 and 2.11 also indicates that NR waveguides behave differently.

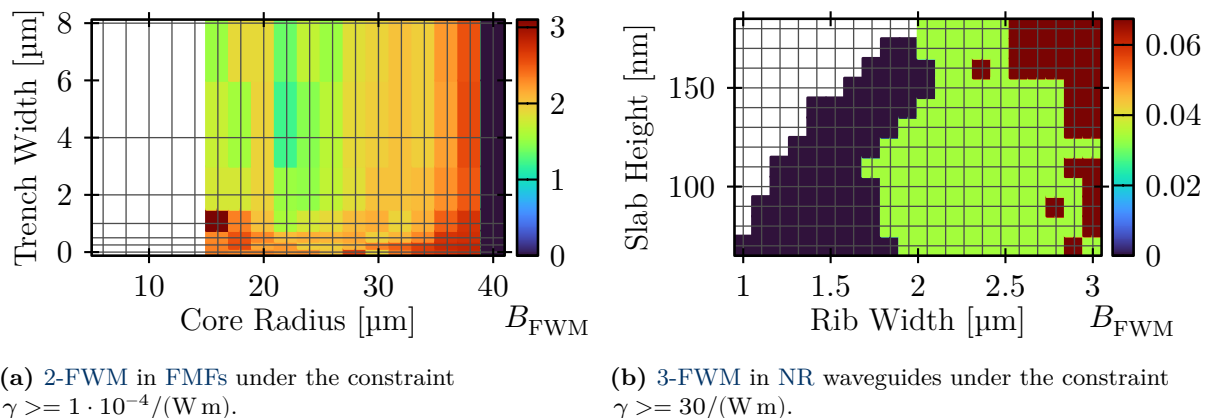


Figure 5.2.: FWM bandwidths for FMFs and NR waveguides with enforced high nonlinearity coefficients. Bandwidths are normalized to multiples of the C-band’s frequency range. Waveguides in white areas don’t support enough guided modes. The figures for 1-FWM in FMFs, 1-FWM in NR waveguides, and 2-FWM in NR waveguides are exactly the same as Figs. 5.1a, 5.1c and 5.1d, respectively, and are not repeated here. The bandwidths for 3-FWM in FMFs are always zero (γ too small) and hence we don’t include a figure.

By comparing the plots in Fig. 5.1, it is clear that FWM in NR waveguides is more sensitive to geometry variations than in FMFs, especially for 2-FWM and 3-FWM. The ultra high bandwidths (more than 10 times the C-band) in Fig. 5.1b are also based on the first kind of phase matching from Section 3.1.3, see e.g. the TE_3 mode in Fig. 2.11f.

5.2. Considering Modal Overlap

From the results in Section 5.1, one could conclude that 3-FWM gives almost equal results as 1-FWM or 2-FWM in the considered parameter ranges. However, the power of a generated FWM idler (Eq. (2.65)) also depends on the nonlinearity coefficient (Eq. (2.66)). In the following, we present FWM bandwidths again (in Fig. 5.2) and additionally nonlinearity coefficients (in Fig. 5.3), but this time forcing the optimizer to only accept FWM configurations where nonlinearity coefficients have at least a predefined minimal value. For FMFs, this value is $\gamma \geq 1 \cdot 10^{-4}/(\text{W m})$ and for NR waveguides $\gamma \geq 30/(\text{W m})$. We selected these numbers, since they represent roughly 10% of the highest achievable values in their respective waveguide types.

Even though we performed PM with the artificially short $L_{\text{wg}} = 10 \text{ m}$, one has to insert the actual fiber length in Eq. (2.65) to compute the correct idler power.

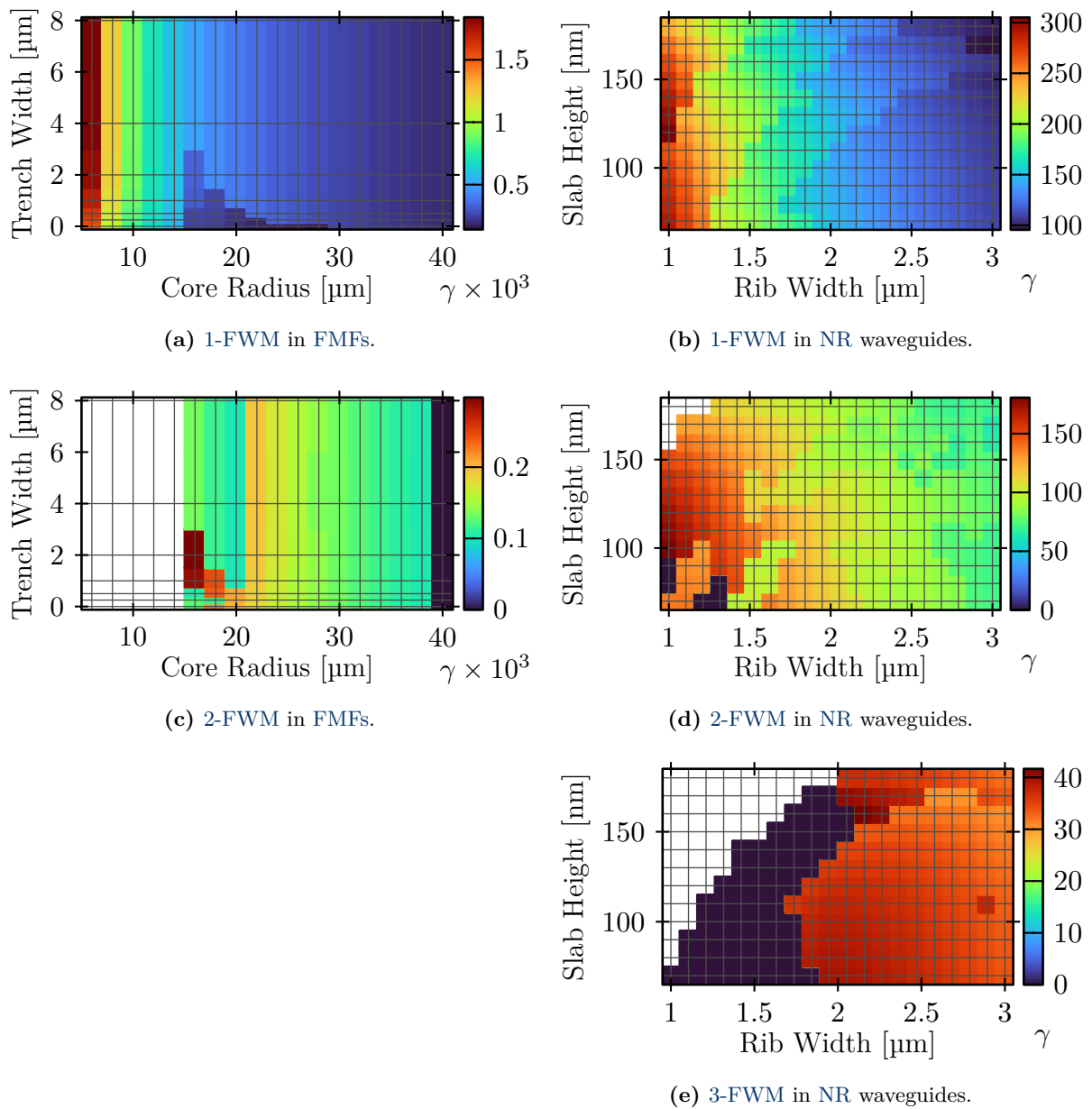


Figure 5.3.: Approximate nonlinearity coefficients for the configurations in Fig. 5.2. Waveguides in white areas don't support enough guided modes. We don't include a figure for 3-FWM in FMFs, since the threshold $\gamma \geq 1 \cdot 10^{-4}/(\text{W m})$ is never fulfilled. The scaling multiplier in the FMF figures is to be understood in a way that gamma values are one thousand times smaller than shown.

Few-Mode Fibers Firstly, enforcing γ values above the chosen threshold does not change the results for 1-FWM, meaning that all configurations in Fig. 5.1a have γ values above the threshold. Secondly, comparing Fig. 5.2a with Fig. 5.1c shows that enforcing a minimal γ also does not have a huge effect on 2-FWM. We see similar bandwidths, except for fibers with $r_{\text{core}} = 40 \mu\text{m}$. A bandwidth of zero in the figure means that our limit on γ could not be achieved by any FWM configuration. The reason is that larger cores have larger effective areas, which leads to lower nonlinearity (see Eq. (2.66)). Finally, there is no 3-FWM configuration in the considered FMFs, where γ values are above our limit. Therefore, idler powers are very weak and we consider 3-FWM in FMFs as infeasible.

Figure 5.3a shows the resulting nonlinearity coefficients γ for the constrained optimization with minimal γ . It is clear that larger cores have lower nonlinearity and that almost all waveguides have γ values at least 5 times higher than our limit. Figure 5.3a and Fig. 5.1a reveal that waveguides with small cores have high 1-FWM bandwidth and high nonlinearity coefficients. For 2-FWM, Fig. 5.3c shows that γ values are lower (roughly around our limit) and the good PM configurations for large cores in Fig. 5.1c have low nonlinearity. However, the configurations with core sizes around $16 \mu\text{m}$ have good bandwidth, acceptable nonlinearity coefficients and 2-FWM is feasible in those fibers.

Nano-Rib Waveguides Enforcing γ values above the chosen threshold does not change the bandwidths in 1-FWM and 2-FWM. Comparing Fig. 5.2b with Fig. 5.1f shows that 3-FWM is severely affected by enforcing high γ values. But, in contrast to FMFs, NR waveguides *do* support 3-FWM. However, the bandwidth is reduced by orders of magnitude to roughly 250 GHz, which still can be enough for processing a few optical channels.

Figures 5.3b and 5.3d show that almost all NR geometries support FWM configurations with high γ values. For 1-FWM, all configurations have nonlinearity coefficients above $100/(\text{W m})$. For 2-FWM, the coefficients are close to $100/(\text{W m})$, except for some scattered geometries where PM fails. To understand the reason for this failure, we have to inspect Fig. 2.11g. The group delay curves do not have any vertical overlap, which means 2-FWM is impossible according to Eq. (3.7).

Finally, Fig. 5.3e, shows that NR 3-FWM γ values are not very sensitive to geometry variations and the coefficients are around $40/(\text{W m})$.

5.3. Power Evolution

In this short section, we show some interesting properties of the power evolution – computed with the same procedure as in Section 4.4 – for an exemplary waveguide with $w_{\text{Rib}} = 3000 \text{ nm}$ and $h_{\text{Slab}} = 140 \text{ nm}$. Figure 5.4 shows idler power evolution under different assumptions A to F. We considered linear attenuation, linear coupling (among modes TE_0 to TE_3), nonlinear coupling and we simulated signal, pumps, BS idler and OPC idler. The figure shows the BS idlers in a 3-FWM configuration where the signal was launched into mode TE_2 at wavelength 1502.0 nm with power 10 dBm , pump 1 into TE_2 at 1316.0 nm with 20 dBm , pump 2 into TE_3 at 1263.9 nm with 20 dBm and the idler evolved in TE_1 at 1576.1 nm .

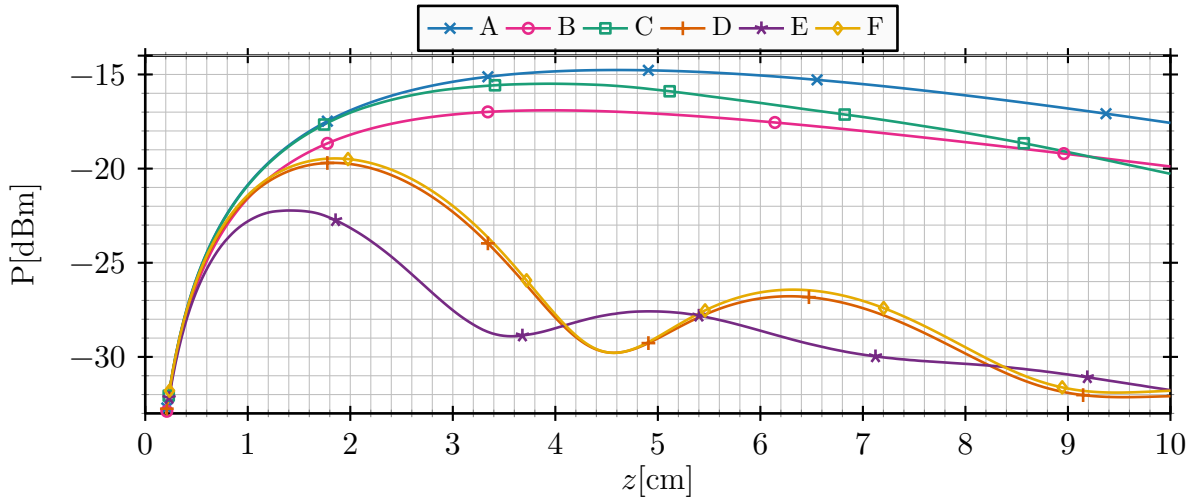


Figure 5.4.: Simulated evolution of the BS idler in a NR waveguide with $w_{\text{rib}} = 3000$ nm and $h_{\text{slab}} = 140$ nm, with five different propagation settings.

Table 5.2.: Attenuation values in [dB/cm] for simulation B in Fig. 5.4. Each column shows attenuation values at the frequency of the wave in the first row (I_{BS} , S, etc.).

Mode \ Frequency	I_{BS}	S	P_1	P_2	I_{OPC}
TE ₀	0.56	0.64	0.8	0.88	1.04
TE ₁	0.7	0.8	1	1.1	1.3
TE ₂	1.05	1.2	1.5	1.65	1.95
TE ₃	1.4	1.6	2	2.2	2.6

These wavelengths and modes are the optimum which lead to the bandwidth shown in Fig. 5.2 for $w_{\text{Rib}} = 3000$ nm and $h_{\text{slab}} = 140$ nm.

In scenario A, we assumed a flat attenuation of 1 dB/cm, no linear coupling and perfect PM. In B, we changed to mode- and frequency dependent loss with values listed in Table 5.2. In C, we added linear coupling to scenario A. We selected linear coupling values to achieve pump coupling similar to our measurements in [35]. In D, we moved the signal frequency from its optimum to the border of the PM region, which created a phase mismatch of $\Delta\beta = 140/\text{m}$ (keeping the rest as in A). The border was defined in Definition 2 such that the idler should drop by 3 dB at the waveguide's end (2 cm). As one can see in the figure, the difference between A and D is indeed close to 3 dBm at 2 cm. Scenario E combines variable attenuation, linear coupling and phase mismatch and one can see that its behavior is different from A to D. The interplay of variable attenuation, linear coupling and phase mismatch can lead to quite different nonlinear behavior (see e.g. [69] or [64, Ch. 3]). Finally, scenario F is like D, but the two photon absorption coefficient was set to $\beta_{\text{TPA}} = 0$ – the effect is very small.

A waveguide length of 2 cm is not the optimum for this waveguide in terms of generated idler power. However, our goal was to optimize and compare FWM bandwidths among different waveguide geometries and FWM types. Hence, we fixed the waveguide lengths to allow for a fair comparison.

6

Experimental Evaluation

In this chapter, we compare our simulation against one of the first and one of the second generation of manufactured waveguides. Measurements of the first generation waveguide were published in [77] and of the second generation in [34], [35]. It should be noted that all measurements were performed by our partners at TUB and HHI. Simulation and geometry parameters and values are listed in Table 6.1.

Table 6.1.: Parameters of the first and second generation waveguides and their operation modes. In the Operation row, e.g. C/L stands for conversion from C- to L-band, etc. Linear attenuations α are measured CW values and exclude GC and MUX losses.

Experiment	1	2
Chip gen.	1	2
Operation	WLC C/L	WLC C/O
w_{rib} [nm]	1190	1672
h_{slab} [nm]	100	100
L_{wg} [mm]	11.7	11.7
α [dB/cm]	TE ₁ : 2.5 TE ₂ : 7.0	TE ₀ : 0.9 TE ₁ : 1.8
λ_{P_1} [nm]	1591.50	1300.00
λ_{P_2} [nm]	1541.00	1540.00
λ_{S^+} [nm]	1544.85	1548.00
λ_{I^+} [nm]	1595.60	1311.75
Mode P ₁	TE ₂	TE ₀
Mode P ₂	TE ₁	TE ₁
Mode S	TE ₁	TE ₁
Mode I	TE ₂	TE ₀
\mathcal{P}_{P_1} [dBm]	26.0	19.33
\mathcal{P}_{P_2} [dBm]	27.0	23.95
\mathcal{P}_{S} [dBm]	12.5	11.28
Measured $\alpha_{\text{GC,out}}$ [dB]	3.2	4.8
Measured CE _{IO} [dB]	48.5	44.0

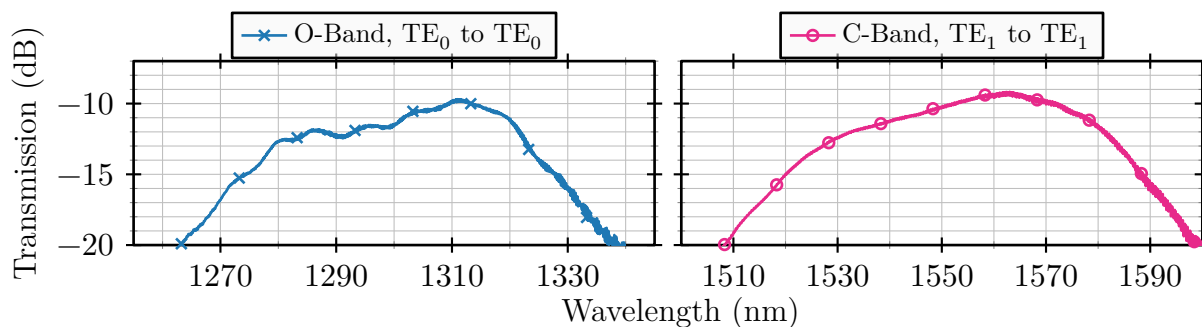


Figure 6.1.: Back to back measurements of a second generation waveguide’s transmission with only negligible waveguide length. Measurements include grating coupler and mode multiplexer losses at both input and output.

6.1. Linear Power Transmission and Group Delay

All our waveguides need grating couplers (GCs) for coupling light in and out of the waveguide, as well as mode multiplexers (MUXs) to excite different waveguide modes by the input lasers and to separate the modes at the output. Both components also contribute to frequency and mode dependent loss, in addition to the attenuation shown in Table 6.1. The combined loss of input and output GCs and mode MUXs is shown in Fig. 6.1. The figure shows power transmission measurements for both modes of a second generation waveguide with negligible length L_{wg} . Total attenuation is in the range 10–15 dB and depends on the offset of laser wavelengths w.r.t the coupler optimum.

We noticed in [77] that SOI waveguides can have severe linear mode coupling. This can also clearly be seen in Fig. 6.2, which shows four measurements of power transmission and linear coupling in the second generation waveguide. In the presented data, coupling loss from Fig. 6.1 and linear attenuation of the actual wave guiding part (α in Table 6.1) are subtracted. The waveguide has wavelength sensitive linear crosstalk, up to more than 10 dB from TE_1 to TE_0 in some narrow regions in the C-band. Hence, for the intended C-to-O-band operation, we expect narrow “dips” in CE_{IO} of up to 10 dB due to linear mode coupling.

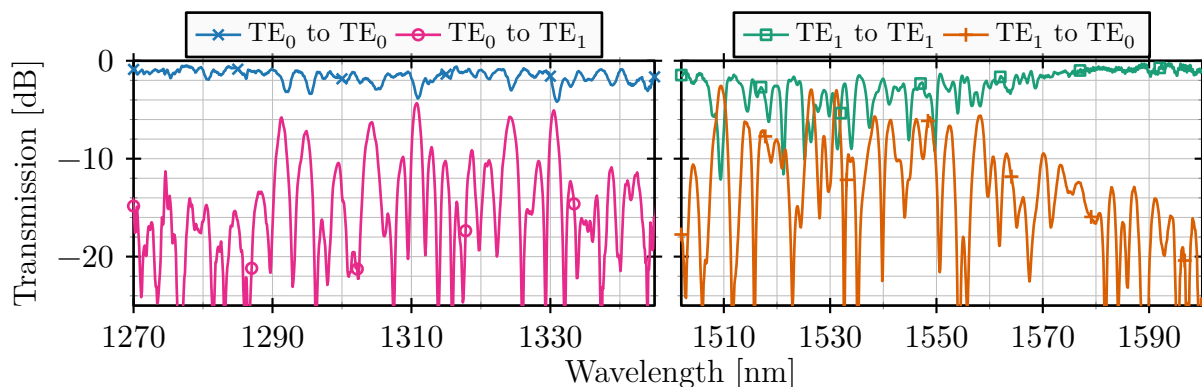


Figure 6.2.: CW power transmission and linear mode coupling of a second generation waveguide.

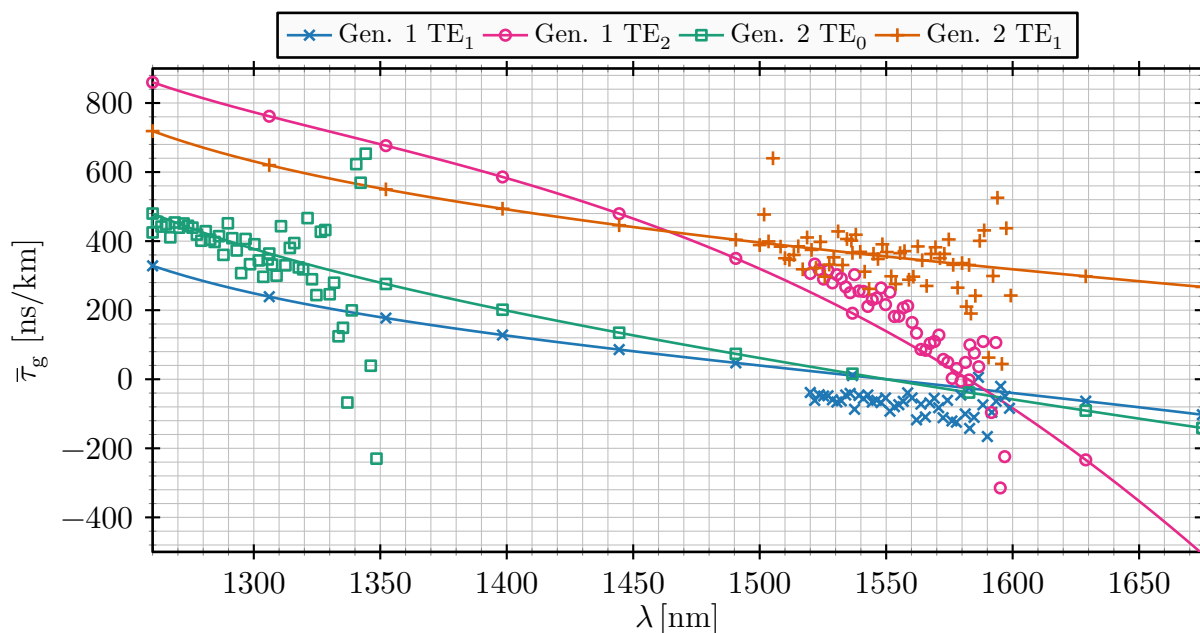


Figure 6.3.: Normalized relative group delays of the two waveguides in this chapter, including CW measurements of each mode. The measurements of the second generation waveguide were shifted down by 170 ns/km for the plot.

Figure 6.3 shows the group delays of the waveguides and modes in Table 6.1, together with C- or O-band CW measurements of each mode. The TE₂ mode of the first generation waveguide is very weakly guided, i.e. light is poorly confined and a significant fraction of the mode’s power propagates close to the rib walls and outside of the rib. This leads to interesting PM properties, but also increases attenuation and linear crosstalk due to the interaction with the rough waveguide walls. In the second generation waveguide, we use modes TE₀ and TE₁, which are more confined and experience less attenuation and mode coupling.

Simulation and measurement in Fig. 6.3 match well, except for a constant offset of 170 ns/km in the second generation waveguide which we corrected in the figure. A constant group delay offset – as long as it is identical for both modes – does not affect PM.

Nevertheless, we tested two hypotheses about the origin of this offset. First, we wanted to know whether slight variations in waveguide dimensions due to manufacturing tolerances could be the cause. We simulated many waveguide geometries around the nominal values in Table 6.1 and compared them with the measurements. For the first generation, we tested rib widths in the range 1186–1194 nm, slab heights in 95–105 nm and SOI heights in 215–225 nm. For the second generation waveguide, we tested rib widths in the range 1655–1687 nm and slab heights in 92–108 nm with smaller steps in between.

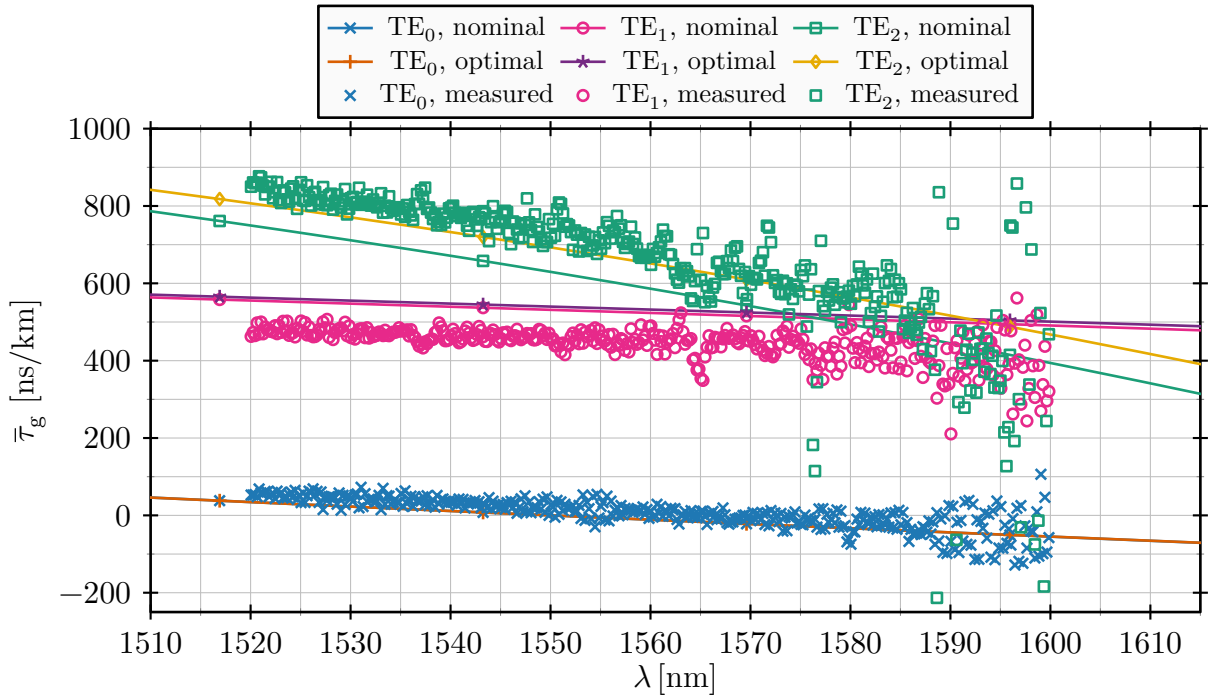


Figure 6.4.: Group delays of the first generation waveguides for nominal and best-fitting geometry values.

We computed the group delays for each geometry and stored the mean square error (MSE)

$$\text{MSE} = \sum_{(m)} \frac{1}{N^{(m)}} \sum_{n=1}^{N^{(m)}} \left(\tau_{g,\text{sim}}^{(m)}[n] - \tau_{g,\text{meas}}^{(m)}[n] \right)^2 \quad (6.1)$$

between measured group delays ($\tau_{g,\text{meas}}$) and simulated group delays of the current geometry ($\tau_{g,\text{sim}}$). Here, n is the frequency sample index and $N^{(m)}$ the total number of measured frequency points of mode (m). Figures 6.4 and 6.5 show simulated group delays for nominal and best fitting (lowest MSE) geometry values, as well as the measurements they were compared to. As it can be seen in the figures, these small geometry fluctuations are not the reason for the vertical offset. While the TE₂ mode in the best fitting geometry of the first generation is slightly closer to the measured values, the fluctuations were by far not enough to achieve the 170 nm/km shift in the second generation.

The second hypothesis was that a tilt of the rib walls ($\alpha_{\text{tilt,l}}$ and $\alpha_{\text{tilt,r}}$ as shown in Fig. 2.8b) could be the case. Figure 6.6 shows the MSE for tilts of up to $\alpha_{\text{tilt,l}} = \pm 15^\circ$ and $\alpha_{\text{tilt,r}} = \pm 15^\circ$. The conclusion is that tilting the walls inwards (replacing core material with silica, upper left direction in the figure) increases group delays and moves the curves in direction of the measurement. However, the total effect on the group delay curves is very small (similar to Fig. 6.5) and thus this is also not the reason for the offset.

We conclude that the vertical shift is most likely a systematic measurement error.

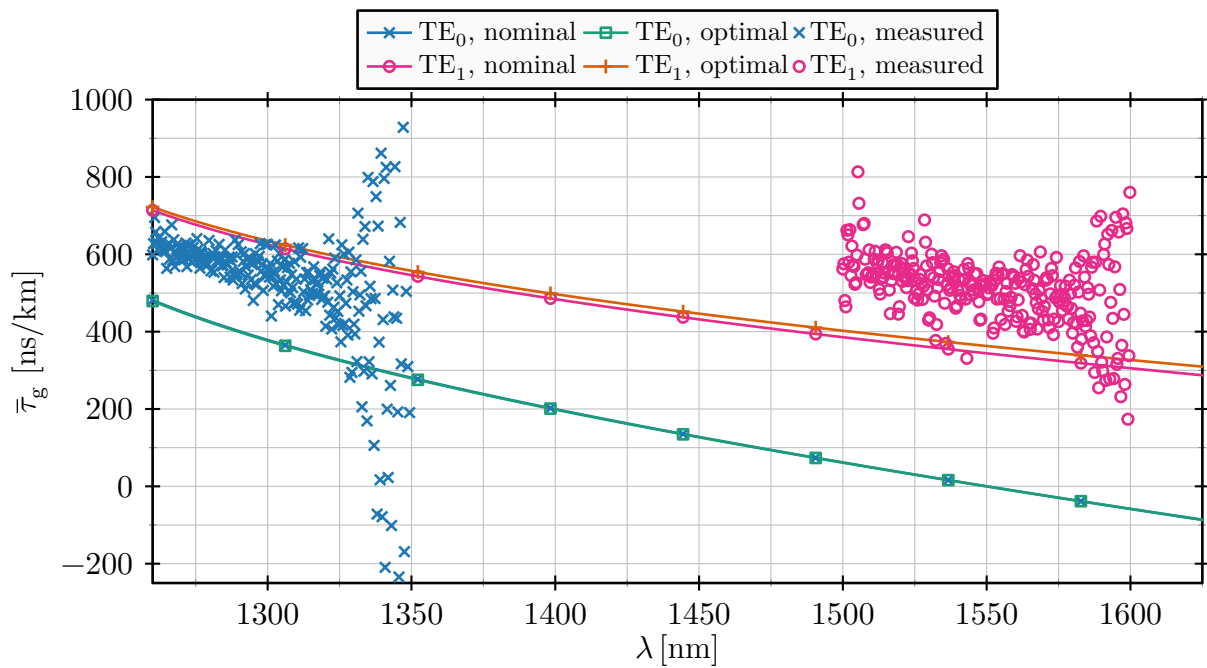


Figure 6.5.: Group delays of the second generation waveguides for nominal and best-fitting geometry values.

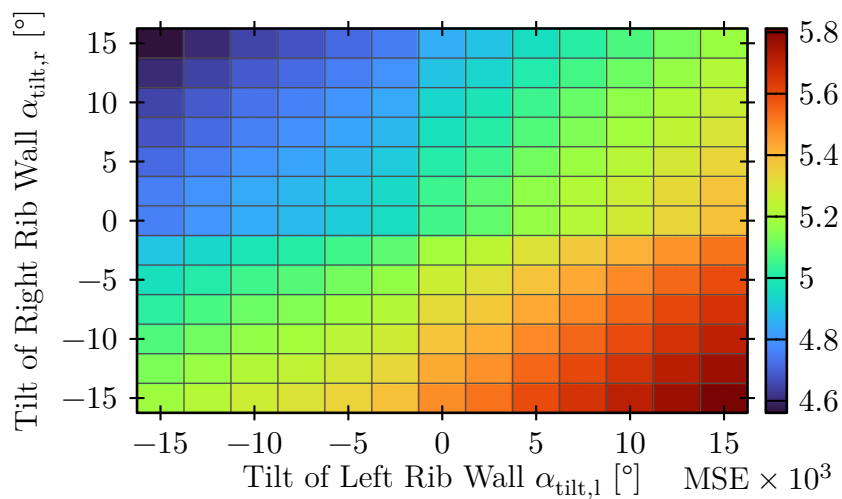


Figure 6.6.: The effect of rib wall tilts on the MSE between measured and simulated group delays. The scaling multiplier is to be understood in a way that MSE values are one thousand times smaller than shown.

6.2. Normalized Idler Power

Figures 6.8a and 6.9a show normalized idler power estimates (see Eqs. (2.63) and (2.65))

$$\mathcal{P}_I \propto |\eta_{\text{FWM}}(\Delta\beta) / \max |\eta_{\text{FWM}}||^2 \quad (6.2)$$

of both experiments with the manufactured geometries in Table 6.1. The wavelengths used in the CW experiments are marked as S⁺, I⁺ and P₂⁺.

Figures 6.8b and 6.9b are slices along P₂⁺ in Figs. 6.8a and 6.9a, respectively. The slices also include measured CW idler powers. Several effects need to be explained which lead to discrepancies between simulation and measurement. Firstly, the tolerance of the etching process can lead to deviations of up to several nanometers of w_{rib} and h_{slab} , as explained above. In contrast to the group delay, these deviations can have a more prominent effect on PM. For the simulation of experiment 1, we needed to assume $w_{\text{rib}} = 1201$ nm to match the measured data and for experiment 2 $w_{\text{rib}} = 1662$ nm and $h_{\text{slab}} = 95$ nm (instead of the nominal values shown in Table 6.1). Secondly, the dips in linear coupling also lead to drops in the idler power (see [77] for the first generation and Fig. 6.2 for the second generation of waveguides). For example, PM is optimal in theory when signal and pump wavelengths coincide. However, the measured idler power in Fig. 6.8b drops close to P₂⁺ due to severe mode coupling in that wavelength region. Finally, keep in mind that idler powers estimated from FWM efficiency are not exact (see Section 2.4.7). Nevertheless, the FWM efficiency η_{FWM} is a very good tool for estimating best-case FWM bandwidth B_{FWM} .

Figure 6.7 shows measured normalized FWM efficiency for varying values of signal and pump, in analogy to Fig. 6.9a. Comparing the two figures, one can see that the bandwidth is smaller in Fig. 6.7 and we attribute the difference to the limiting effect of the GCs and to linear coupling.

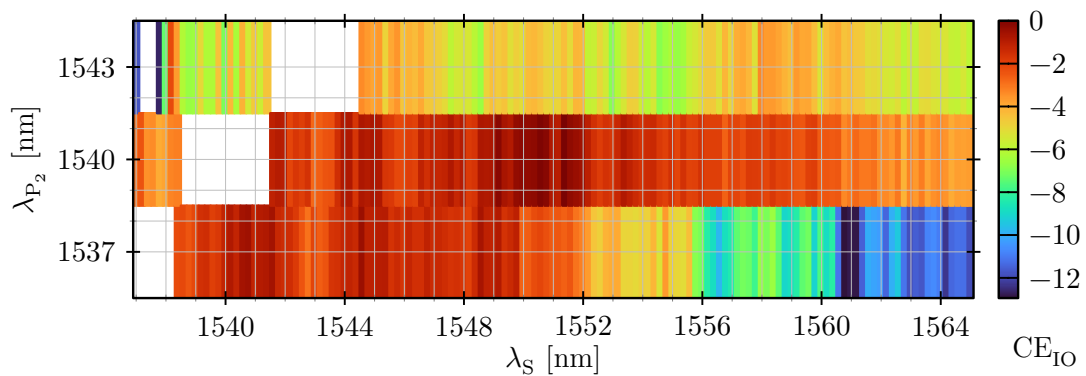
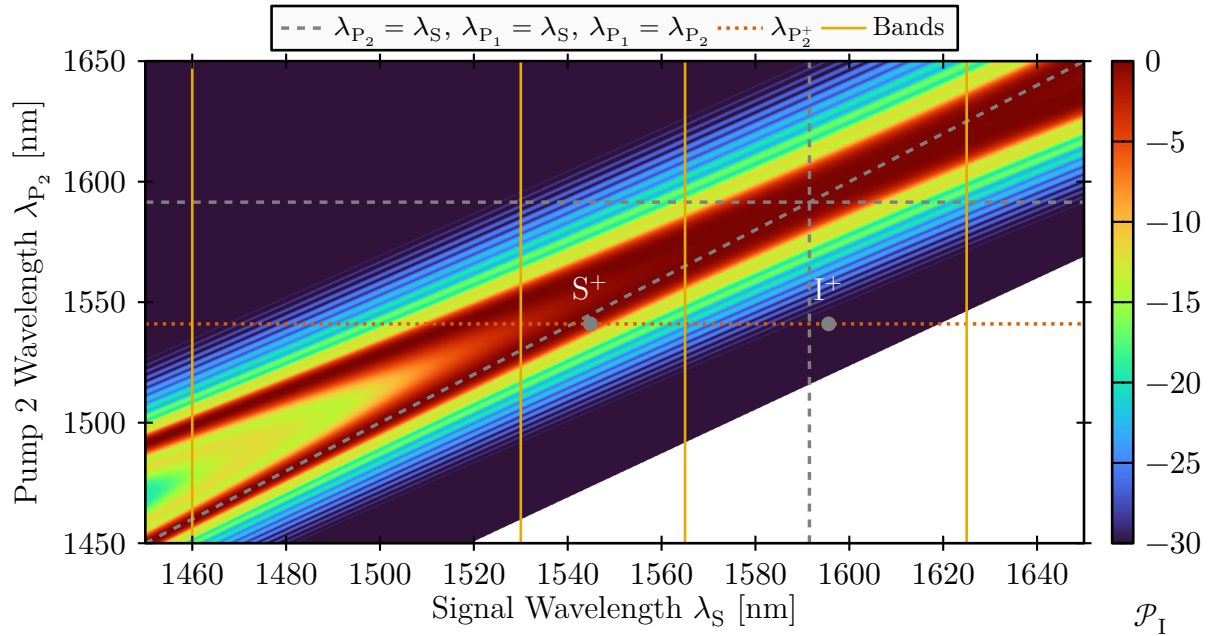
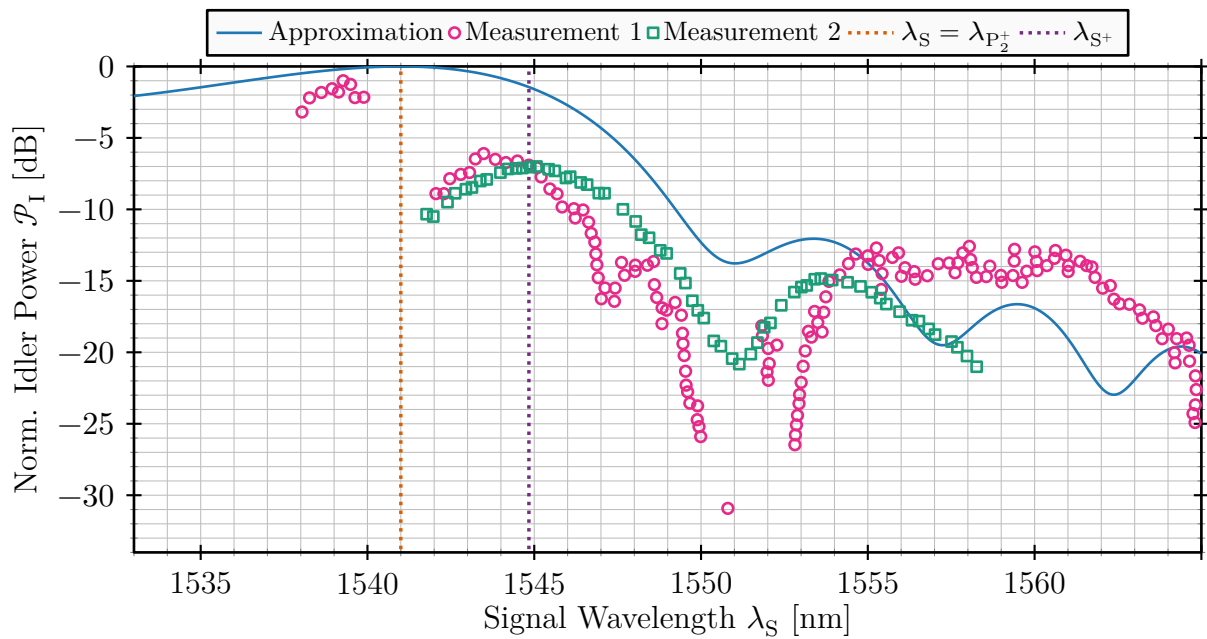
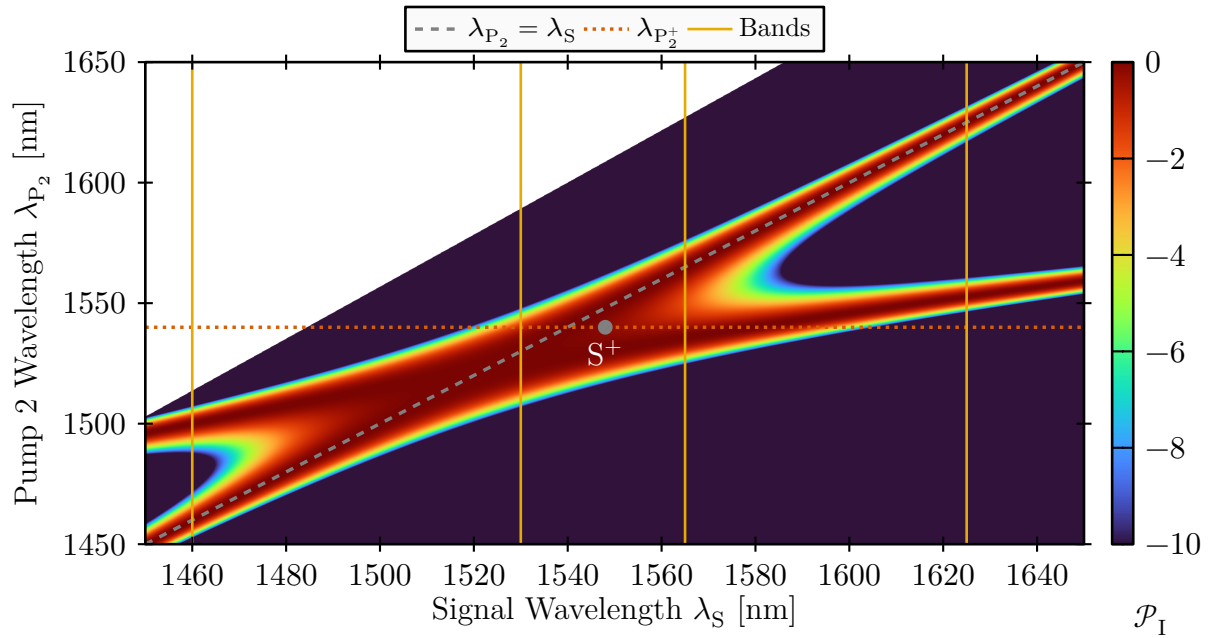


Figure 6.7.: Measured FWM efficiency of the second generation waveguide for varying signal and pump 2 wavelengths. Pump 1 is fixed at 1300 nm and each row is normalized to its peak efficiency.

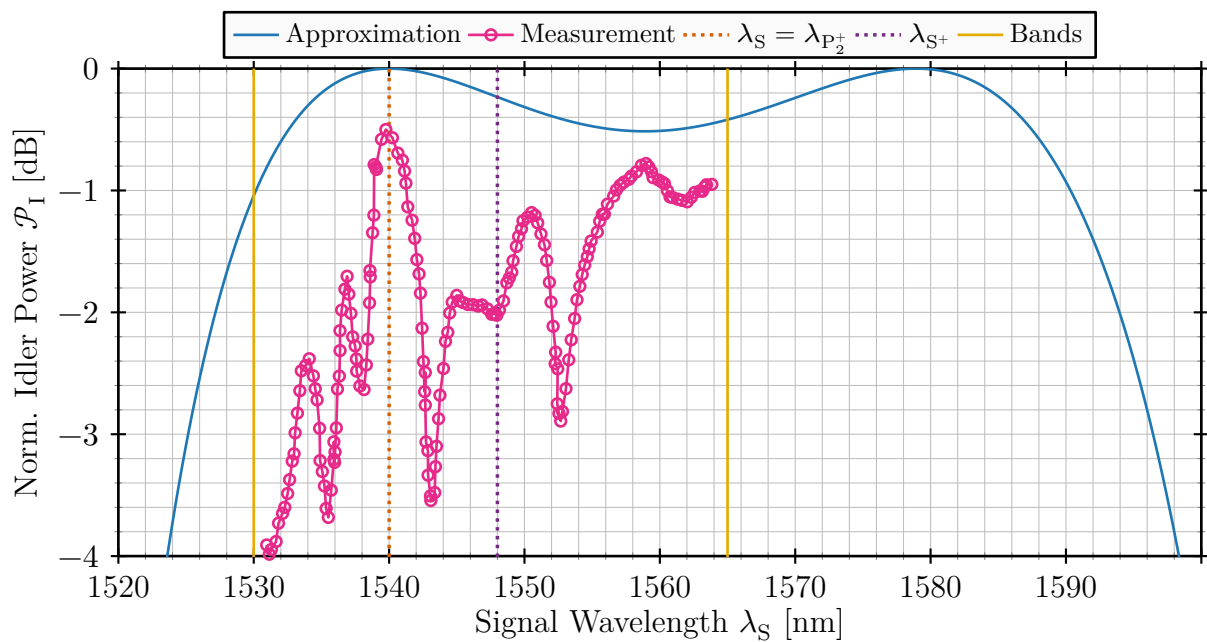


(a) Two-dimensional plot.

(b) Slice along P_2^+ . Two CW idler power measurements are added, both vertically shifted to fit the simulation.**Figure 6.8.:** Simulated and measured normalized idler power in experiment 1 from Table 6.1.



(a) Two-dimensional plot.

(b) Slice along P_2^+ . A CW idler power measurement is added, vertically shifted to fit the simulation.**Figure 6.9.:** Simulated and measured normalized idler power in experiment 2 from Table 6.1.

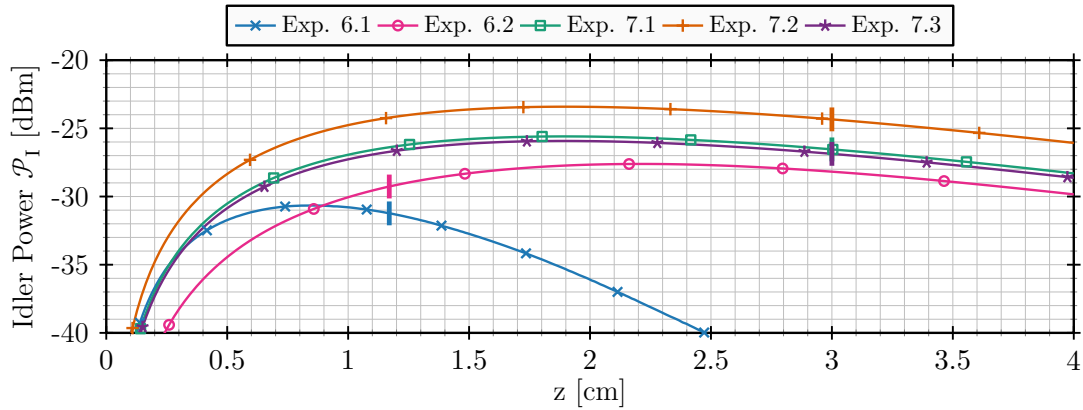


Figure 6.10.: Simulated idler power evolution along the waveguides in both experiments in Table 6.1 (Experiments 6.1 and 6.2) and in the three experiments in Table 7.1 from Chapter 7 (Experiments 7.1, 7.2 and 7.3). The vertical bars mark waveguide lengths L_{wg} .

6.3. Absolute Conversion Efficiency

To compare the absolute measured idler power in terms of CE_{IO} (see Definition 1) between simulation and experimental results, we performed simulations with our propagation framework introduced in Chapter 4 for both experiments in Table 6.1. We did the same for the three experiments in Table 7.1 from Chapter 7 and already include the results here. For each simulation, we considered 12 waves: one in each of the modes TE_0 , TE_1 and TE_2 , at the frequencies of pump 1, pump 2, signal and idler. We used $n_2 = 10 \cdot 10^{-18} \text{ m}^2/\text{W}$ for the nonlinear refractive index of silicon and $\beta_{TPA} = 0.5 \cdot 10^{-11} \text{ m/W}$ for the two photon absorption coefficient. The simulated idler powers are presented in Fig. 6.10.

The shown powers are *inside* the waveguides. Therefore, to compute the CE_{IO} , the output GC loss needs to be subtracted: $CE_{IO} = \mathcal{P}_I - \mathcal{P}_S - \alpha_{GC,out}$. When we insert the values from Table 6.1 and Fig. 6.10, the simulation predicts $CE_{IO} = -31.2 \text{ dBm} - 12.5 \text{ dBm} - 3.2 \text{ dB} = -46.9 \text{ dB}$ for the first experiment, which is close to the measured value of -48.5 dB . For the second experiment, we get $CE_{IO} = -29.3 \text{ dBm} - 11.28 \text{ dBm} - 4.8 \text{ dB} = -45.38 \text{ dB}$, also close to the measured value of -44.0 dB .

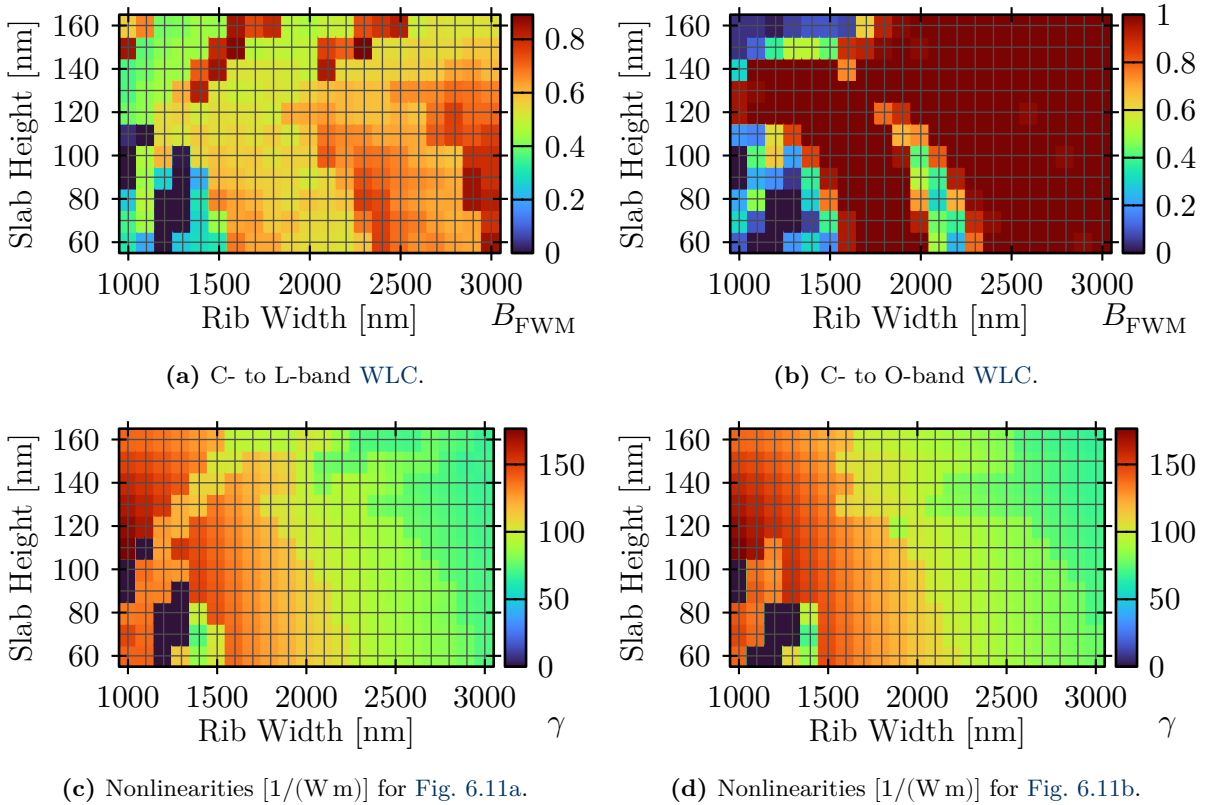


Figure 6.11.: Highest achievable FWM bandwidths and nonlinearity parameters for the two experiments in Table 6.1, in waveguides with different geometries. Two-mode operation with two lasers per mode is enforced. All bandwidths are normalized and clipped to the C-band’s width.

6.4. Geometry Optimization

We developed our optimization framework after manufacturing the first three generations of waveguides. Nevertheless, we performed a geometry optimization with our method from Section 3.2 for both experiments in Table 6.1, under the constraint that nonlinearity coefficients are at least $\gamma \geq 50/(\text{W m})$ (roughly one third of the highest achievable value). The resulting FWM bandwidths and nonlinearity coefficients can be seen in Fig. 6.11. These figures show which geometries would have been optimal and what we can expect from our already manufactured waveguides.

Since we consider a conversion of the C-band into another band, we normalized the FWM bandwidth to the full width of the C-band and all higher bandwidths are clipped to 1. The figures show the highest achievable B_{FWM} for each of the considered waveguides. We enforced two-mode operation and considered modes TE_0 , TE_1 , TE_2 and TE_3 .

The optimizations in Fig. 6.11a show the results for WLC from C- to L-band. According to the simulation, the manufactured first generation waveguide ($w_{\text{rib}} \approx 1190 \text{ nm}$, $h_{\text{slab}} \approx 100 \text{ nm}$) would allow for about 60 % of the C-band. However, conversion is unfortunately restricted by the GC transmission bands, which we had to design before having the optimization framework ready.

The optimizations in Fig. 6.11b show the results for WLC from C- to O-band. It can be seen that our manufactured waveguide ($w_{\text{rib}} \approx 1672 \text{ nm}$, $h_{\text{slab}} \approx 100 \text{ nm}$) is capable of converting more than the C-band. Here we luckily designed the GC transmission bands suitingly and get the broadband conversion shown in Fig. 6.9b above.

7

Broadband FWM in the TE₂ Mode

The first kind of phase matching in Section 3.1.3 has the benefit of an enormous FWM bandwidth for both, BS and OPC. In this chapter, we present a geometry optimization with the goal to have one single waveguide which can be operated in different modes by simply changing pump wavelengths. The three modes are OPC from C- to L-band, OPC from C- to C-band²⁶ and WLC from C- to S-band. We have already four generations of manufactured waveguides (see Chapter 6 for experiments with the first two). The results of this chapter are in fabrication at the time of writing and will be the fifth generation.

We optimized NR geometry for 1-FWM in the TE₂ mode, again under the constraint that nonlinearity coefficients are enforced to be at least $\gamma \geq 50/(\text{W m})$ (roughly one third of the highest achievable value). The results can be seen in Fig. 7.1. The figures show the maximal achievable B_{FWM} for each of the considered waveguides, under the additional constraints of the respective scenario (C- to L- WLC, etc.). Since we consider a conversion from the C-band into another band, we normalized B_{FWM} to the full width of the C-band and all higher bandwidths are clipped to 1. Figure 7.1a shows the results for OPC from C- to L-band, Fig. 7.1b OPC from C- to C-band and Fig. 7.1c BS from C- to S-band. From comparing the three figures, we decided on a geometry in the middle of all three regions with high B_{FWM} : $w_{\text{rib}} = 1700 \text{ nm}$, $h_{\text{slab}} = 72 \text{ nm}$. The regions are broad enough to allow for a manufacturing tolerance margin. Figure 7.1d shows the nonlinearity coefficients of the waveguide, which are the same for all experiments since all of them use the TE₂ mode and the frequency dependence on the overlap integrals (and hence on the nonlinearity parameters) is barely noticeable. Fortunately, the selected geometry also has relatively high nonlinearity coefficients of roughly $180/(\text{W m})$.

The group delay of the TE₂ mode of this waveguide with its wide low-dispersion region is shown in Figure 7.2. Optimal PM for the three operating modes is achieved with the laser wavelengths listed in Table 7.1.

With the optimal values for λ_{P_1} from Table 7.1, the versatility of this waveguide is evident from Fig. 7.3. The figures show normalized idler power estimates (see Eq. (6.2)). The wavelengths of signal and pump 2 can be tuned in a very wide range, without affecting the idler power. S^+ , I^+ and P_2^+ are the values used in the propagation simulation below. The waveguide is in

²⁶ Intra-band optical phase conjugation works by placing the pumps symmetrically below and above of the band. This way, signals from the lower part of the band are conjugated and mirrored at the band's center to the upper part of the band.

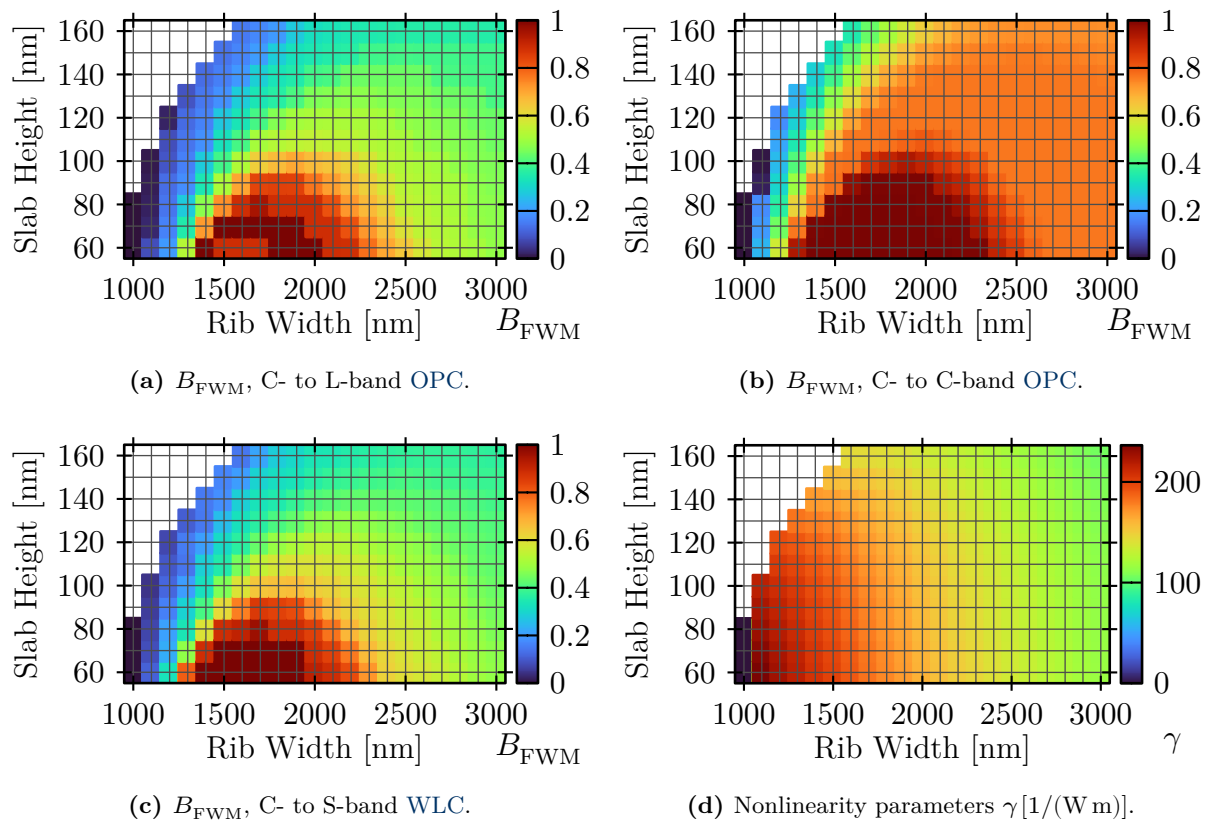


Figure 7.1.: Highest achievable FWM bandwidths and corresponding nonlinearity parameters for the three operation modes from Table 7.1, in waveguides with different geometries. All lasers are enforced to propagate in the TE_2 mode and waveguides in white areas don't support this mode. All bandwidths are normalized and clipped to the C-band's width.

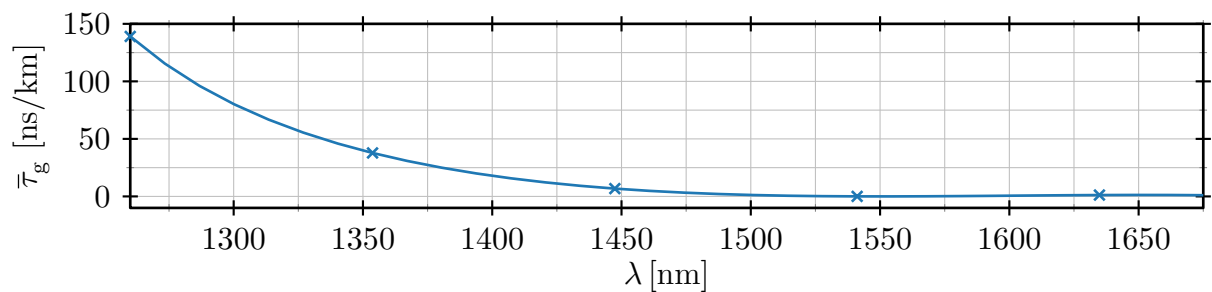


Figure 7.2.: Normalized relative group delay of the TE_2 mode in the fifth generation waveguide.

Table 7.1.: Parameters of the fifth generation waveguide and its three planned operation modes. In the Operation row, e.g. C/L stands for conversion from C- to L-band, etc. Extrapolating from measurements of similar waveguides, we expect the shown attenuation values in this waveguide.

Experiment	1	2	3
Chip gen.		5	
Operation	OPC C/L	OPC C/C	WLC C/S
w_{rib} [nm]		1700	
h_{slab} [nm]		72	
L_{wg} [mm]		30	
α [dB/cm]	TE ₀ : 1.4, TE ₁ : 2.3, TE ₂ : 2.5		
λ_{P_1} [nm]	1606.65	1571.20	1567.56
λ_{P_2} [nm]	1527.99	1524.13	1606.53
λ_{S^+} [nm]	1547.50	1543.81	1547.50
λ_{I^+} [nm]	1585.63	1550.82	1511.31
\mathcal{P}_{P_1} [dBm]		25	
\mathcal{P}_{P_2} [dBm]		25	
\mathcal{P}_S [dBm]		12	
Estimated $\alpha_{GC,out}$ [dB]		5	

principle capable of much higher bandwidths than the C-band, but operation is limited by the GC bandwidths (see Chapter 6). We selected the three operation modes in Table 7.1 in a way that they are achievable with the GCs we use on the chip.

We simulated 12 waves with our propagation framework introduced in Chapter 4: modes TE₀, TE₁ and TE₂ at the frequencies of pump 1, pump 2, signal and idler in Table 7.1 – once for each operation mode. The results were already shown in Fig. 6.10. Since we have again idler powers *inside* the waveguide, we need to subtract the GC losses. We expect CE_{IO} values of roughly $-27 \text{ dBm} - 12 \text{ dBm} - 5 \text{ dB} = -44 \text{ dB}$ for experiments 1 and 3 and $-25 \text{ dBm} - 12 \text{ dBm} - 5 \text{ dB} = -42 \text{ dB}$ for experiment 2. The peak power difference comes from GC transmission characteristics which cause 2 dB extra loss for one pump in experiments 1 and 3 each.

In summary, we expect to have found a very versatile waveguide for different modes of operation, with simply adjusting pump wavelengths.

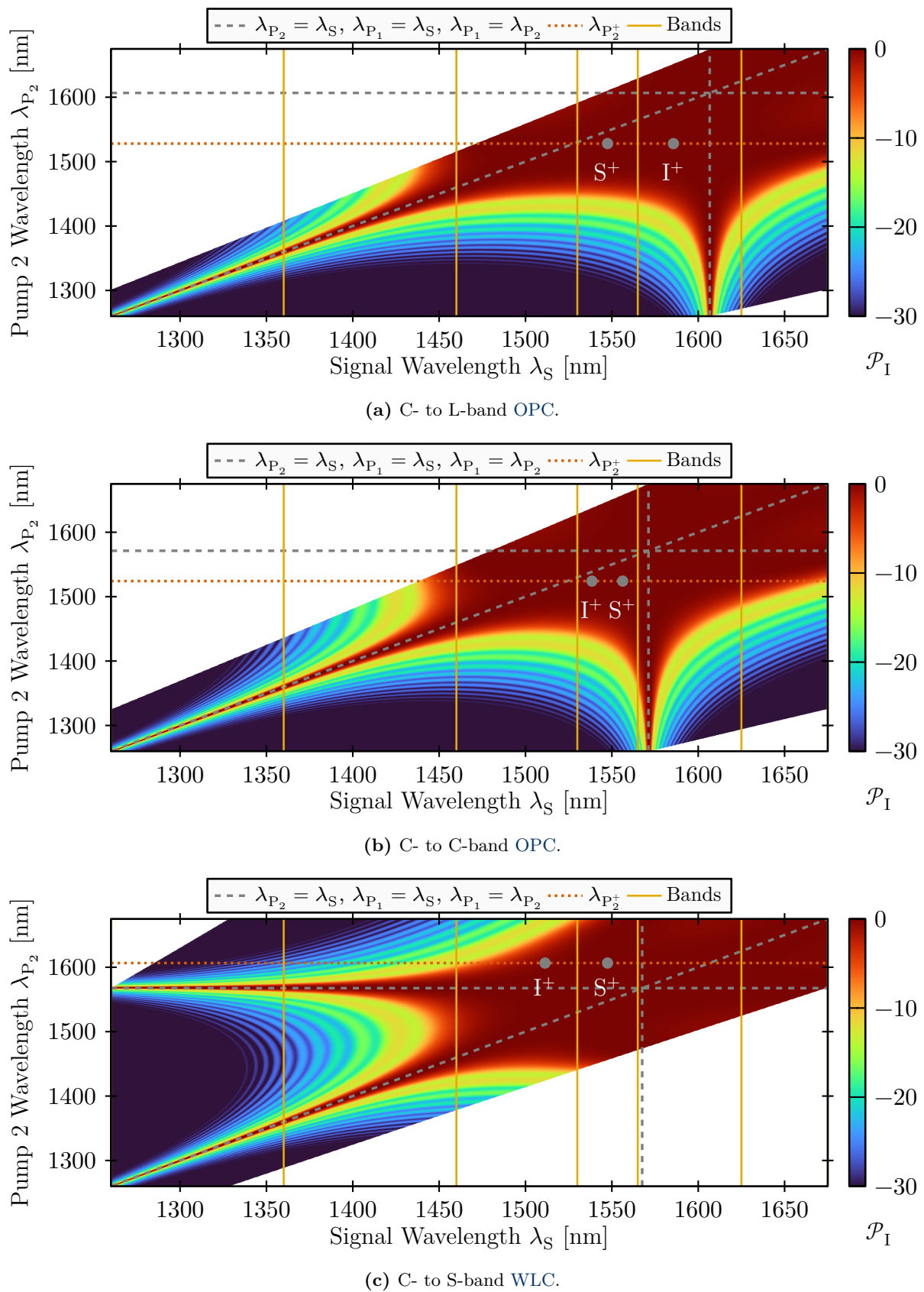


Figure 7.3.: Estimates of normalized idler power in the three operation modes from Table 7.1.

8

Conclusions

We gave a brief introduction into the fascinating field of nonlinear optical processing. The nonlinear nature of electron and molecular response to propagating light becomes evident whenever the light is strong enough and/or the interaction length is high enough. While this can be a disturbing effect in long-haul fiber links, we use this effect for all-optical signal processing to achieve [wavelength conversion](#) and [optical phase conjugation](#).

We introduced models of frequency dependent refractive index, material nonlinearity and linear mode coupling.

We performed optimizations and simulations in optical fibers and [NR](#) waveguides to maximize [FWM](#) efficiency and to predict the resulting CE_{IO} .

In [Chapter 3](#), we presented our numerical approaches for [phase matching](#) and waveguide geometry optimization.

[PM](#) is the process of maximizing [FWM](#) conversion efficiency in a given waveguide. Laser wavelengths and the selection of modes are optimized to fulfill energy conservation and match momentum conservation as close as possible. We also computed overlap integrals of the propagating mode fields to be able to exclude [PM](#) configurations which result in very low idler power.

For optimizing waveguide geometry, we computed [FWM](#) bandwidths and approximate idler powers for several waveguide geometries and compared them. We have shown that good [PM](#) is achievable for both, [wavelength conversion](#) and [optical phase conjugation](#) for converting between the C- and other optical bands.

By adding dips, it is possible to alter the dispersion behavior of a waveguide – which is beneficial for certain kinds of [PM](#).

In **Chapter 4**, we presented our **CW** propagation simulation for computing accurate idler power estimates in **NR** waveguides. It considers linear attenuation, linear coupling and nonlinear coupling.

We base our model for linear coupling on the roughness of the waveguide walls which emerges from etching the chip while it is manufactured.

We model material nonlinearity by the susceptibility tensor $\overset{\leftrightarrow}{\chi}^{[3]}$, where we assume that its values are constant for all considered wavelengths.

In **Chapter 5**, we showed that **1-FWM** and **2-FWM** perform better than **3-FWM** in both, **FMFs** and **NR** waveguides. **FWM** bandwidths as well as nonlinearity coefficients are both larger. However, some **NR** waveguides do work with acceptable efficiency in narrowband operation. Depending on the intended use case, it might be acceptable to sacrifice some idler power and broadband operation to gain the flexibility to place signal, pump and idler in three different modes. While this holds for **3-FWM** in **NR** waveguides, **4-FWM** does not work in neither **FMFs**, nor in **NR** waveguides.

In **Chapter 6**, we compared our **PM** and **CW** propagation simulations against lab measurements of two waveguides. We found that **FWM** efficiency is a good approximation for maximal achievable **FWM** bandwidth. The absolute idler powers computed with our **CW** simulation match the measured values very well, even though our linear coupling model is quite simple.

In **Chapter 7**, we discovered that the TE_2 mode of certain **NR** geometries supports a very wide region of low dispersion. We showed that it is possible to perform **WLC** from C- to S-band, **OPC** from C- to L-band and **OPC** from C- to C-band, with one single waveguide. The operation modes can be switched by merely tuning the pumps to different wavelengths. We will test the flexible operation modes in the next generation of waveguides which are in the process of manufacturing.

In summary, we presented a simulation framework which can be used to find waveguides suited for different all-optical processing tasks and which can predict the resulting idler powers to a sufficiently high accuracy.

We are especially looking forward to test the performance and versatility of the TE_2 -based, next generation waveguides from **Chapter 7**.

A

Appendices

A.1. Conventions And Transformations Used Throughout the Thesis

In this appendix, we collect several transformations and conventions used throughout the thesis.

A.1.1. Fourier Transform

We define the Fourier transform as

$$x(f) = \mathcal{F}\{x(t)\} = \int_{-\infty}^{\infty} x(t)e^{-j2\pi ft} dt \quad (\text{A.1})$$

$$x(t) = \mathcal{F}^{-1}\{x(f)\} = \int_{-\infty}^{\infty} x(f)e^{j2\pi ft} df. \quad (\text{A.2})$$

If a quantity is in time or frequency domain is either clear from context, or we explicitly write the time or frequency dependence, as above. We don't use the convention that lowercase letters denote time domain and uppercase letters frequency domain quantities. However, sometimes we do both, e.g. $x(t) \circ \bullet X(f)$.

In the rest of this section, we repeat some Fourier theorems we use in the thesis.

Time Shift An offset τ in time domain is equivalent to multiplication with a complex oscillation in frequency domain

$$x(t - \tau) \circ \bullet X(f)e^{-j2\pi\tau f}. \quad (\text{A.3})$$

Derivatives A derivative in time domain is equivalent to a multiplication with $j2\pi f = j\omega$ in frequency domain

$$\frac{dx(t)}{dt} \circ \bullet j2\pi f X(f) = j\omega X(f). \quad (\text{A.4})$$

Convolution Convolution in time domain is equivalent to multiplication in frequency domain

$$(x \otimes y)(t) \circ \bullet X(f)Y(f). \quad (\text{A.5})$$

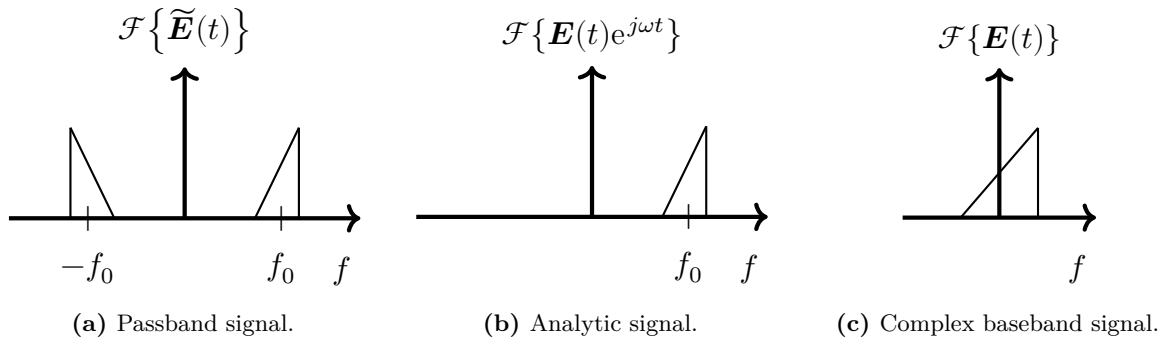


Figure A.1.: Spectra of different representations of the same signal.

A.1.2. Passband, Analytic, and Baseband Signal Conventions

In communications engineering, it is common to encounter modulated signals (e.g. a modulated laser or radio wave), which consist of the multiplication of a fast sinusoidal carrier wave with a typically orders of magnitude slower payload signal. The spectrum of such a signal is depicted in Fig. A.1a. We denote such (rapidly varying) passband signals with a tilde, e.g. $\tilde{\mathbf{E}}(t)$.

Since such a signal is always real-valued, its spectrum obeys the property $\tilde{\mathbf{E}}(-f) = \tilde{\mathbf{E}}(f)^*$. This means that the negative half of the spectrum is redundant and a passband signal can be represented as an analytic signal without any loss of information. Figure A.1b shows the analytic version of a passband signal (in Fourier domain). We denote analytic signals without a tilde as in $\mathbf{E}(t)e^{j\omega t}$, where ω is the carrier frequency. To convert a passband signal to its analytic form, the Hilbert transform can be used. It simply removes negative frequencies.

Finally, $\mathbf{E}(t)$ is the baseband signal which is the slowly varying part of $\tilde{\mathbf{E}}(t)$ and is shown in Fig. A.1c.

An analytic signal can simply be converted back to the passband by removing its imaginary part

$$\tilde{\mathbf{E}}(t) = \mathcal{R}e\{\mathbf{E}(t)e^{j\omega t}\}.$$

A complex phasor is a special case of an analytic signal, where the baseband signal is time invariant. Its spectrum is a Dirac delta instead of the sketched triangles in Fig. A.1.

One needs to be careful when manipulating terms with analytic or baseband signals. Only linear operations like addition, subtraction, derivatives and integrals are allowed. For example, these computations give the same result:

$$\begin{aligned} & \tilde{\mathbf{E}}_1(t) + \tilde{\mathbf{E}}_2(t) \\ &= \left(\frac{1}{2}\mathbf{E}_1(t)e^{j\omega_1 t} + c.c.\right) + \left(\frac{1}{2}\mathbf{E}_2(t)e^{j\omega_2 t} + c.c.\right) \\ &= \mathcal{R}e\{\mathbf{E}_1(t)e^{j\omega_1 t} + \mathbf{E}_2(t)e^{j\omega_2 t}\}, \end{aligned}$$

meaning that adding analytic signals and transforming the result to passband gives the correct result. However, whenever nonlinear operations are involved, the passband signals must be used:

$$\begin{aligned} & \tilde{\mathbf{E}}_1(t) \cdot \tilde{\mathbf{E}}_2(t) \\ &= \left(\frac{1}{2}\mathbf{E}_1(t)e^{j\omega_1 t} + c.c.\right) \cdot \left(\frac{1}{2}\mathbf{E}_2(t)e^{j\omega_2 t} + c.c.\right) \\ &\neq \mathcal{R}e\{\mathbf{E}_1(t)e^{j\omega_1 t} \cdot \mathbf{E}_2(t)e^{j\omega_2 t}\}. \end{aligned}$$

A.1.3. Plane Wave Convention

We model the propagation of a plane wave in positive z direction as

$$e^{j(\omega t - \beta z)}. \quad (\text{A.6})$$

A.1.4. Converting Attenuation

In our propagation model Eq. (4.31), we need attenuation coefficients $\alpha_a^{(m)}$ in Np/m. It is easy to convert values measured in dB/km to Np/m by

$$\alpha_{\text{Np/m}} = \frac{\alpha_{\text{dB/km}}}{10^3} \frac{1}{10 \log_{10} e} \approx \frac{\alpha_{\text{dB/km}}}{4343}. \quad (\text{A.7})$$

A.2. The Maximum of FWM Efficiency

In this appendix, we show that FWM efficiency is maximal for $\Delta\beta = 0$, irrespective of attenuation α and waveguide length L_{wg} . For that, we show that the maximum of

$$|\eta_{\text{FWM}}(\Delta\beta)|^2 = \left| \frac{1 - \exp(-(\alpha + j\Delta\beta)L_{\text{wg}})}{(\alpha + j\Delta\beta)L_{\text{wg}}} \right|^2$$

is achieved for $\Delta\beta = 0$.

We start with defining some shortened variables

$$\bar{\alpha} := \alpha L_{\text{wg}} \tag{A.8}$$

$$\bar{\beta} := \Delta\beta L_{\text{wg}} \tag{A.9}$$

$$w := \bar{\alpha} + j\bar{\beta}, \quad |w|^2 = \bar{\alpha}^2 + \bar{\beta}^2, \tag{A.10}$$

to rewrite η_{FWM} and separate real and imaginary parts as

$$\begin{aligned} \eta_{\text{FWM}}(w(\bar{\beta}(\Delta\beta))) &= \frac{1 - e^{-w}}{w} = \frac{1 - e^{-\bar{\alpha}} e^{-j\bar{\beta}}}{w} \\ &= \frac{1 - e^{-\bar{\alpha}} \cos(\bar{\beta}) + j e^{-\bar{\alpha}} \sin(\bar{\beta})}{w}. \end{aligned} \tag{A.11}$$

Now we can compute the squared magnitude as

$$\begin{aligned} F(\bar{\beta}) := |\eta_{\text{FWM}}(\bar{\beta})|^2 &= \frac{1 - 2e^{-\bar{\alpha}} \cos(\bar{\beta}) + e^{-2\bar{\alpha}} \cos^2(\bar{\beta}) + e^{-2\bar{\alpha}} \sin^2(\bar{\beta})}{|w|^2} \\ &= \frac{1 + e^{-2\bar{\alpha}} - 2e^{-\bar{\alpha}} \cos(\bar{\beta})}{\bar{\alpha}^2 + \bar{\beta}^2}. \end{aligned} \tag{A.12}$$

To show that the point $\Delta\beta = 0$ is the maximum, we need the derivative

$$\begin{aligned} \frac{dF(\bar{\beta})}{d(\Delta\beta)} &= \frac{dF(\bar{\beta})}{d\bar{\beta}} \frac{d\bar{\beta}}{d(\Delta\beta)} = \frac{dF(\bar{\beta})}{d\bar{\beta}} L_{\text{wg}} \\ &= \frac{|w|^2 2e^{-\bar{\alpha}} \sin(\bar{\beta}) - (1 + e^{-2\bar{\alpha}} - 2e^{-\bar{\alpha}} \cos(\bar{\beta})) 2\bar{\beta}}{|w|^4} L_{\text{wg}}. \end{aligned} \tag{A.13}$$

The efficiency has an extremum for $\Delta\beta = 0$, since

$$\left. \frac{dF(\bar{\beta})}{d\bar{\beta}} \right|_{\bar{\beta}=0} = \frac{|w|^2 2e^{-\bar{\alpha}} \sin(0) - (1 + e^{-2\bar{\alpha}} - 2e^{-\bar{\alpha}} \cos(0)) 2 \cdot 0}{\bar{\alpha}^4} = 0. \tag{A.14}$$

To determine the extremum type, we rewrite Eq. (A.13) and use some approximations

$$\begin{aligned} \frac{dF(\bar{\beta})}{d\bar{\beta}} &= \frac{2e^{-\bar{\alpha}}}{|w|^4} (|w|^2 \sin(\bar{\beta}) - (e^{\bar{\alpha}} + e^{-\bar{\alpha}}) \bar{\beta} + 2\bar{\beta} \cos(\bar{\beta})) \\ &= \frac{2e^{-\bar{\alpha}}}{|w|^4} \left(|w|^2 \underbrace{\sin(\bar{\beta})}_{\approx \bar{\beta}} - 2\bar{\beta} \cosh(\bar{\alpha}) + 2\bar{\beta} \underbrace{\cos(\bar{\beta})}_{\approx 1 - \frac{\bar{\beta}^2}{2}} \right) \end{aligned} \quad (\text{A.15})$$

$$\begin{aligned} &\approx \frac{2e^{-\bar{\alpha}}}{|w|^4} (\bar{\beta}^3 + \bar{\alpha}^2 \bar{\beta} - 2\bar{\beta} \cosh(\bar{\alpha}) + 2\bar{\beta} - \bar{\beta}^3) \\ &= \bar{\beta} \frac{2e^{-\bar{\alpha}}}{|w|^4} (\bar{\alpha}^2 + 2 - 2 \cosh(\bar{\alpha})) \\ &= \bar{\beta} \frac{2e^{-\bar{\alpha}}}{|w|^4} \left(\bar{\alpha}^2 + 2 - 2 \left(1 + \frac{\bar{\alpha}^2}{2!} + \frac{\bar{\alpha}^4}{4!} + \dots \right) \right) \\ &= \bar{\beta} \frac{2e^{-\bar{\alpha}}}{\underbrace{(\bar{\alpha}^2 + \bar{\beta}^2)}_{>0}} \underbrace{\left(-\frac{\bar{\alpha}^4}{4!/2} - \frac{\bar{\alpha}^6}{6!/2} + \dots \right)}_{<0}. \end{aligned} \quad (\text{A.16})$$

Equation (A.16) shows that the derivative is positive for $\bar{\beta} < 0$ and negative for $\bar{\beta} > 0$ and we can conclude that we have a maximum.

We used the small angle approximation in Eq. (A.15) for both, sin and cos. Hence, the above result is only valid in the close vicinity of $\Delta\beta = 0$. For larger values we can see from Eq. (A.12) that the $\bar{\beta}^2$ term in the denominator leads to continuous decrease of the function, making $\bar{\beta} = 0$ the global maximum.

Figure A.2 shows the FWM efficiency, its derivative and our approximative derivative, for three different values of α . It can clearly be seen that the small angle approximation is only valid for very small values of $\Delta\beta$. From the figure, it is also clear that the global maximum is in the center.

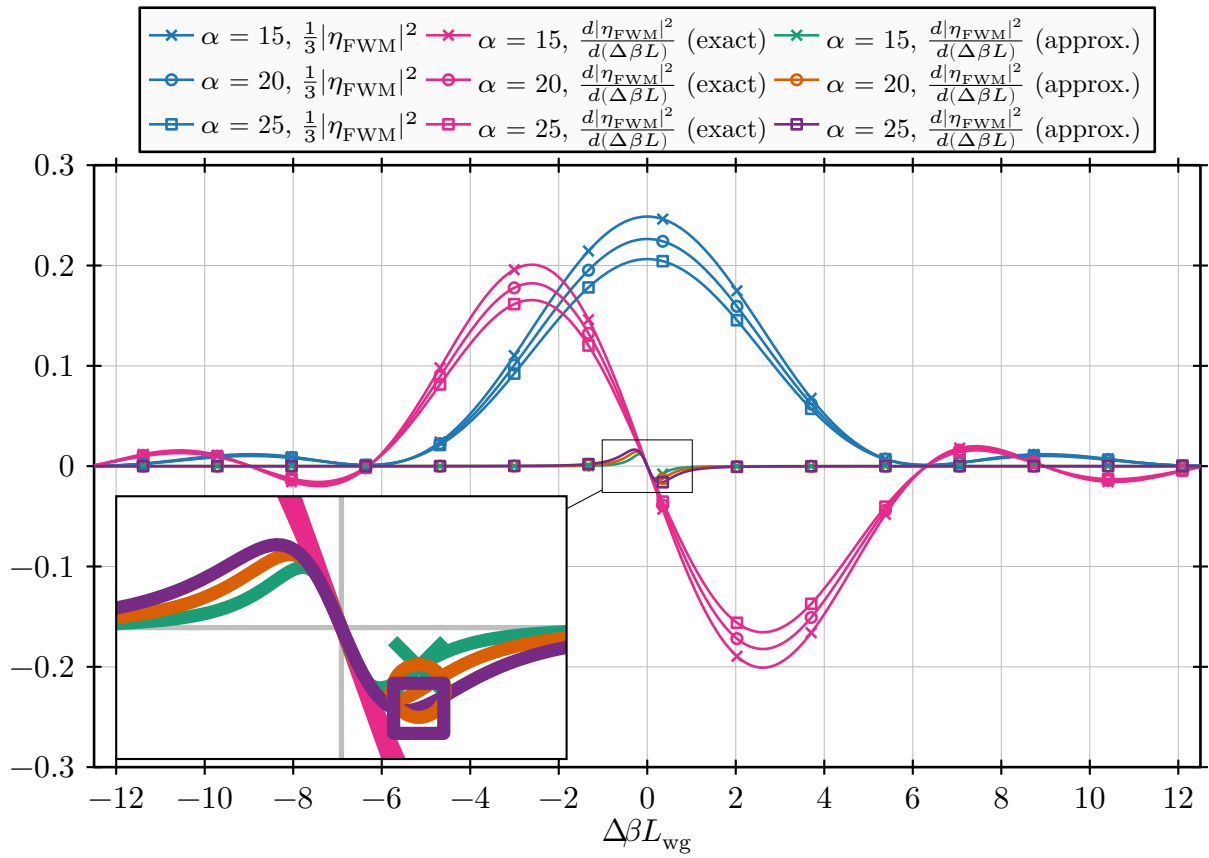


Figure A.2.: Typical form of the FWM efficiency η_{FWM} , its derivative and approximate derivative for different values of attenuation α and fixed length $L_{\text{wg}} = 2$ cm. The values are selected to resemble a typical NR waveguide and η_{FWM} is scaled to fit into the plot.

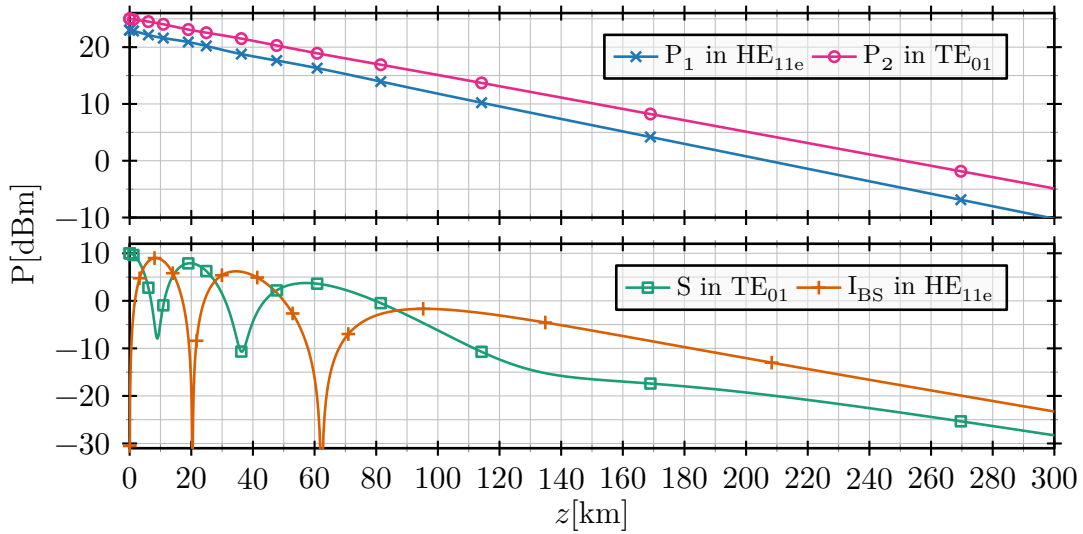


Figure A.3.: Simulated power evolution of pumps, signal and idler in fiber 3 (depressed cladding) of Table 2.2, similar to Fig. 4.3, but with very small phase mismatch.

A.3. Power Evolution With low Phase Mismatch

In this appendix, we analyze a simplified variant of the simulation shown in Fig. 4.3.

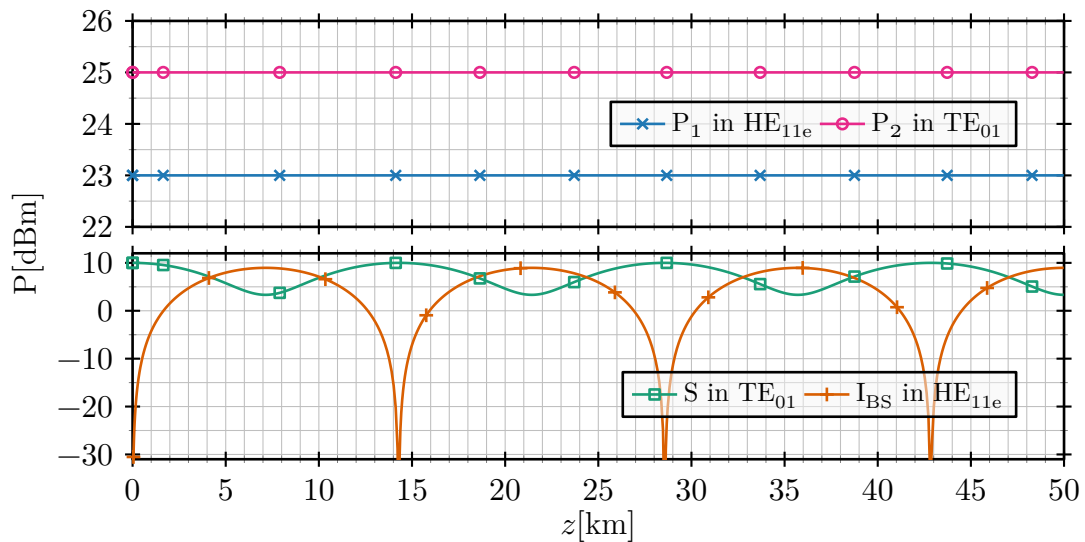
Before we start simplifying the problem, Fig. A.3 shows the same experiment, but with signal wavelength $\omega_s = 1542.69 \text{ nm} \rightarrow \omega_1 = 1535.86 \text{ nm}$. At this signal wavelength, the phase mismatch is very low with $\frac{2\pi}{|\Delta\beta|} = 524.9 \text{ km}$, as compared to $\frac{2\pi}{|\Delta\beta|} = 36.48 \text{ km}$ in Fig. 4.3. We can see that signal and idler periodically exchange power, which stops roughly after 150 km when the propagating powers are so low that nonlinear interaction gets negligible and only linear attenuation remains. Note that the oscillation period of 524.9 km due to phase mismatch is much longer than the period we see in the figure. The goal of this appendix is to determine the cause of the oscillations.

The simulation above involves linear attenuation and nonlinear coupling between all propagating waves, modeled by Eq. (4.31). Even though it is small, we did not ignore the phase mismatch $\Delta\beta$ in this simulation. It was considered via the $e^{-j\Delta\beta \binom{m+opq}{a+abcd} z}$ term in the nonlinear coupling equations.

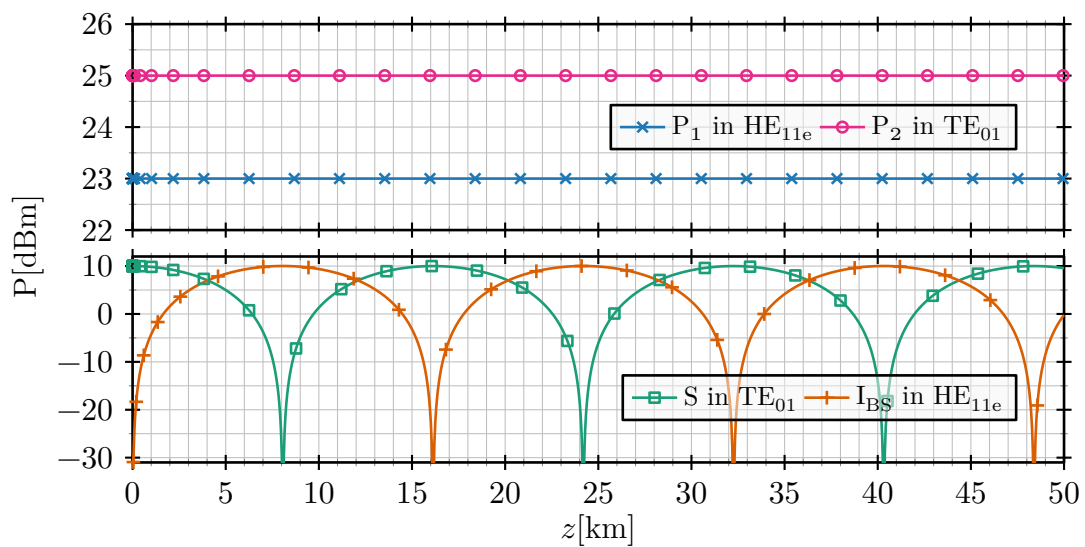
Now we want to derive an analytic expression for the signal and idler evolution. For that, we need to introduce the following approximations:

- The phase mismatch is negligible, i.e., PM is perfect. We set $\Delta\beta = 0$ for all combinations.
- Attenuation is very low, we set $\alpha = 0$.
- There is no linear coupling, we set $\mathbb{L} = 0$.
- Pumps are not depleted in the process, i.e., \hat{E}_{P_1} and \hat{E}_{P_2} are constant.

With these approximations, Fig. A.4a shows the simulated evolution along the waveguide. One can see that FWM is slightly more efficient than in Fig. A.3. Furthermore, the signal and idler exchange powers in an almost sinusoidal way.



(a) Same as in Fig. A.3, but without attenuation and without pump depletion.



(b) Same as above in (a), but with only the nonlinear terms listed in Eqs. (A.19) and (A.20) (no SPM and no XPM).

Figure A.4.: Simulated power evolution of pumps, signal and idler similar to Fig. A.3, but with approximations.

To derive an analytic expression of the idler evolution, recall that only the four signals in Table 4.2 propagate along the waveguide, all other nonlinear interaction is suppressed in the simulation. The evolution of the pumps is clear, they are constant in this approximation so their amplitude does not change along the waveguide. If we incorporate our approximations (no linear attenuation, no linear coupling and no phase mismatch) into Eq. (4.31), the idler evolution is described by the remaining terms

$$\frac{d\hat{\mathbb{I}}}{dz} = -j \sum_{\substack{b,c,d(o),(p),(q) \\ \in \mathcal{S}_a}} \sum_{\in \{1,2\}} \mathbb{N}_{a+bc d}^{(m+opq)} \hat{E}_b^{(o)}(z) \hat{E}_c^{(p)}(z) (\hat{E}_d^{(q)}(z))^*. \quad (\text{A.17})$$

We introduced $\hat{\mathbb{I}} = \hat{E}_{a=4}^{(m)=(1)}(z)$, where the indices $(m) = (1)$ and $a = 4$ are taken from Table 4.2. Likewise we will use $\hat{\mathbb{S}} = \hat{E}_3^{(2)}(z)$, $\hat{\mathbb{P}}_1 = \hat{E}_1^{(1)}(0)$ and $\hat{\mathbb{P}}_2 = \hat{E}_2^{(2)}(0)$ below (note that $\hat{\mathbb{S}}$ and $\hat{\mathbb{I}}$ are z dependent, while $\hat{\mathbb{P}}_1$ and $\hat{\mathbb{P}}_2$ are constant). The set \mathcal{S}_a in the first sum considers all frequency combinations which give rise to a wave at the idler's frequency. The summation thus considers certain combinations of $\{1, 2, 3, 4\}$ (as defined in Table 4.2).

If we write out both sums, we get

$$\begin{aligned} \frac{d\hat{\mathbb{I}}}{dz} = & -j\mathbb{N}_{\text{P}_1\text{SP}_2}^{\text{I}} \hat{\mathbb{P}}_1 \hat{\mathbb{S}} (\hat{\mathbb{P}}_2)^* & -j\mathbb{N}_{\text{SP}_1\text{P}_2}^{\text{I}} \hat{\mathbb{S}} \hat{\mathbb{P}}_1 (\hat{\mathbb{P}}_2)^* \\ & -j\mathbb{N}_{\text{III}}^{\text{I}} \hat{\mathbb{I}} \hat{\mathbb{I}} (\hat{\mathbb{I}})^* \\ & -j\mathbb{N}_{\text{P}_2\text{IP}_2}^{\text{I}} \hat{\mathbb{P}}_2 \hat{\mathbb{I}} (\hat{\mathbb{P}}_2)^* & -j\mathbb{N}_{\text{IP}_2\text{P}_2}^{\text{I}} \hat{\mathbb{I}} \hat{\mathbb{P}}_2 (\hat{\mathbb{P}}_2)^* \\ & -j\mathbb{N}_{\text{P}_1\text{IP}_1}^{\text{I}} \hat{\mathbb{P}}_1 \hat{\mathbb{I}} (\hat{\mathbb{P}}_1)^* & -j\mathbb{N}_{\text{IP}_1\text{P}_1}^{\text{I}} \hat{\mathbb{I}} \hat{\mathbb{P}}_1 (\hat{\mathbb{P}}_1)^* \\ & -j\mathbb{N}_{\text{SIS}}^{\text{I}} \hat{\mathbb{S}} \hat{\mathbb{I}} (\hat{\mathbb{S}})^* & -j\mathbb{N}_{\text{ISS}}^{\text{I}} \hat{\mathbb{I}} \hat{\mathbb{S}} (\hat{\mathbb{S}})^*, \end{aligned} \quad (\text{A.18})$$

where we introduced shorter names for the nonlinear coupling coefficient, e.g. $\mathbb{N}_{\text{P}_1\text{SP}_2}^{\text{I}}$ determines the coupling strength for the FWM process $\omega_{\text{I}} = \omega_{\text{P}_1} + \omega_{\text{S}} - \omega_{\text{P}_2}$, etc. The two coefficients $\mathbb{N}_{\text{P}_1\text{SP}_2}^{\text{I}}$ and $\mathbb{N}_{\text{SP}_1\text{P}_2}^{\text{I}}$ have the same value and we simply call them \mathbb{N}^{I} below. Similarly we define $\mathbb{N}^{\text{S}} := \mathbb{N}_{\text{IP}_2\text{P}_1}^{\text{S}}$. The two terms in the first row of Eq. (A.18) are responsible for FWM, the term in the second row for SPM of the idler and the remaining terms are XPM between the idler and the three other propagating waves. The equations for the signal can be derived with identical steps.

There are too many coupled terms in Eq. (A.18) to be able to find an analytic solution. Therefore, our next approximation is to ignore all SPM and XPM terms, both, for signal and idler. Then we can model the severely simplified interaction with

$$\frac{d\hat{\mathbb{I}}}{dz} = -2j\mathbb{N}^{\text{I}} \hat{\mathbb{S}} \hat{\mathbb{P}}_1 (\hat{\mathbb{P}}_2)^* \quad (\text{A.19})$$

$$\frac{d\hat{\mathbb{S}}}{dz} = -2j\mathbb{N}^{\text{S}} \hat{\mathbb{I}} \hat{\mathbb{P}}_2 (\hat{\mathbb{P}}_1)^*. \quad (\text{A.20})$$

Figure A.4b shows the evolution similar to Fig. A.4a but with all SPM and XPM terms removed from the simulation.

One can see that when we ignore the SPM and XPM terms, the power oscillation period between signal and idler becomes slightly longer and the signal and idler exchange more power.

Now we can take the derivative of Eq. (A.19) and insert Eq. (A.20) to get

$$\frac{d^2\hat{I}}{dz^2} = -4\mathbb{N}^I\mathbb{N}^S |\hat{P}_1|^2 |\hat{P}_2|^2 \hat{I} = -\rho^2 \hat{I}, \quad (\text{A.21})$$

where we defined the constant

$$\rho = 2\sqrt{\mathbb{N}^I\mathbb{N}^S} |\hat{P}_1| |\hat{P}_2|. \quad (\text{A.22})$$

This is a simple differential equation with the general solution

$$\hat{I} = c_1 \sin(\rho z) + c_2 \cos(\rho z). \quad (\text{A.23})$$

The constants c_1 and c_2 can be computed from the initial conditions $\hat{I}(0) = I_0 = 0$ (no idler at the start of the fiber) and $\hat{S}(0) = S_0$ (amplitude of the signal at the start of the fiber). We get

$$\hat{I}(0) = c_1 \sin(\rho 0) + c_2 \cos(\rho 0) \stackrel{!}{=} I_0 = 0 \Rightarrow c_2 = 0. \quad (\text{A.24})$$

By taking the derivative of Eq. (A.23) and setting it equal to Eq. (A.19), we can solve for

$$S(z) = \frac{-c_1 \rho}{2j\mathbb{N}^I \hat{P}_1 (\hat{P}_2)^*} \cos(\rho z). \quad (\text{A.25})$$

With $S(0) \stackrel{!}{=} S_0$ we can also compute the constant

$$c_1 = -jS_0 \sqrt{\frac{\mathbb{N}^I \hat{P}_1 (\hat{P}_2)^*}{\mathbb{N}^S (\hat{P}_1)^* \hat{P}_2}}. \quad (\text{A.26})$$

One can see that the oscillation period $\frac{2\pi}{|\rho|}$ depends on the overlap integrals hidden in \mathbb{N}^I and \mathbb{N}^S , as well as on the pump amplitudes. We get $\frac{2\pi}{|\rho|} = 32.26$ km if we insert the values, which is exactly the period in Fig. A.4b and is not too far away from the more realistic Fig. A.4a with SPM and XPM. Note that the plotted powers show absolute values and thus one period $\frac{2\pi}{|\rho|}$ extends over two of apparent periods in the figure.

Since we set all $\Delta\beta$ values to zero, the oscillations in Figs. A.4a and A.4b are not caused by a phase mismatch, but from the nonlinear “direct” interaction of signal and idler (as shown in Eq. (A.18)).

In summary, we gained some insight on nonlinear interaction when linear attenuation and phase mismatch are very low. However, the more approximations we incorporate, the more the results deviate from the actual behavior in fiber. The most interesting insight gained by this analytical approach is that the power exchange oscillations between signal and idler not only happen due to residual phase mismatch, but also due to the “direct” nonlinear interaction between the propagating waves when the phase mismatch is low.

A.4. Collected Implementation Details and Issues

In this appendix, we present selected implementation details and some issues we encountered and had to solve.

A.4.1. Representing Fields as 3D Vectors of Matrices

The working principle of the **FDM** is to discretize fields on a grid. Implementation-wise, this means that all components of a three-dimensional field like $\mathbf{E} = [E_x \ E_y \ E_z]^T$ have to be represented as matrices. Hence, the matrix nature of field components needs to be considered when implementing operations like $\mathbf{E}^* \cdot \mathbf{H}$ or the tensor product $\overset{\leftrightarrow}{\chi}^{[3]}(\tau_b, \tau_c, \tau_d) : \widetilde{\mathbf{E}}(t - \tau_b) \widetilde{\mathbf{E}}(t - \tau_c) \widetilde{\mathbf{E}}(t - \tau_d)$ in Eq. (4.1). Another example is the matrix multiplication $(\Psi_{a^+}^{(m+)})^* \cdot (\underline{\Delta}\epsilon_r \Psi_{a^+}^{(o')})$ in Eq. (4.30), where $\underline{\Delta}\epsilon_r$ needs to be a 3×3 matrix of grid-sized matrices.

Yet another example is the computation of the nonlinear coupling coefficient in Eq. (4.36). Each transversal field profile Ψ is a vector of three matrices as above and the result of the tensor product is also such a vector. The scalar product of the vectors yields a matrix (of grid size) and finally the two integrals turn the matrix into a scalar.

A.4.2. Linear Combination of LP Modes

Mode fields can be represented in different bases. The two most commonly used bases are the physical modes consisting of

$$\{\text{HE}_{11e}, \text{HE}_{11o} \mid \text{HE}_{21e}, \text{HE}_{21o}, \text{TE}_{01}, \text{TM}_{01} \mid \text{HE}_{31e}, \text{HE}_{31o}, \text{EH}_{11e}, \text{EH}_{11o} \mid \text{HE}_{12e}, \text{HE}_{12o}\}$$

and the linearly polarized modes

$$\{\text{LP}_{01x}, \text{LP}_{01y} \mid \text{LP}_{11ax}, \text{LP}_{11ay}, \text{LP}_{11bx}, \text{LP}_{11by} \mid \text{LP}_{21ax}, \text{LP}_{21ay}, \text{LP}_{21bx}, \text{LP}_{21by} \mid \text{LP}_{02x}, \text{LP}_{02y}\},$$

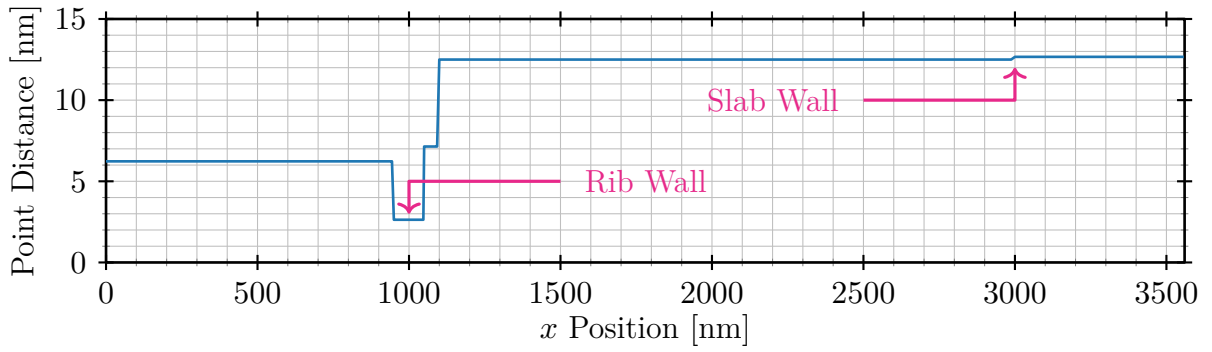
where $|$ mark mode groups. Propagation constants in a mode group are very similar.

The two sets can be transformed into each other by linear combination of the modes in the mode groups. For example, we get

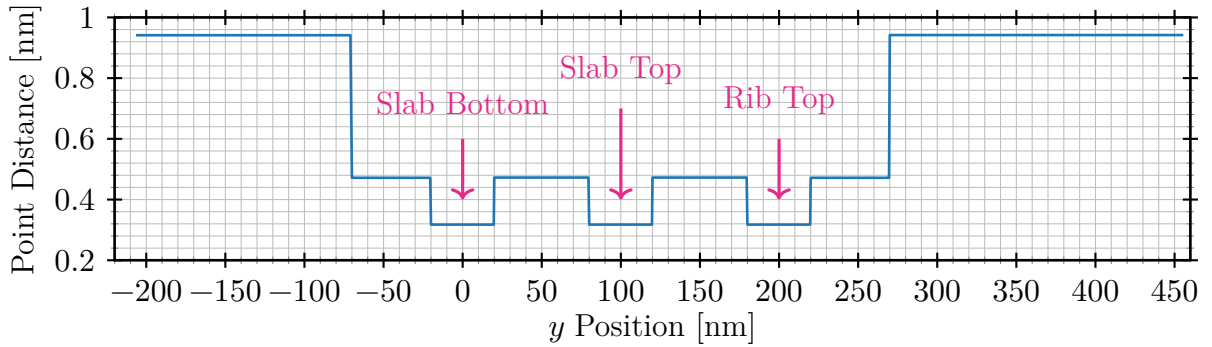
$$\begin{aligned} \text{LP}_{11ax} &= +0.501 \ \text{HE}_{21e} \ +0.000 \ \text{HE}_{21o} \ -0.000 \ \text{TE}_{01} \ +0.500 \ \text{TM}_{01} \\ \text{LP}_{11by} &= +0.501 \ \text{HE}_{21e} \ -0.000 \ \text{HE}_{21o} \ -0.000 \ \text{TE}_{01} \ -0.500 \ \text{TM}_{01} \\ \text{LP}_{21ax} &= -0.499 \ \text{HE}_{31e} \ +0.006 \ \text{HE}_{31o} \ +0.512 \ \text{EH}_{11e} \ -0.004 \ \text{EH}_{11o} \\ \text{LP}_{21by} &= -0.511 \ \text{HE}_{31e} \ +0.007 \ \text{HE}_{31o} \ -0.502 \ \text{EH}_{11e} \ +0.004 \ \text{EH}_{11o} \end{aligned}$$

from a simple minimization of the **MSE** between mode fields. Hence, an LP mode launched into a waveguide will always excite more than one physical mode. Even though the superposition is always between modes of one mode group where propagation constants are similar, they are not exactly the same. The modes propagate with slightly different phase velocities which leads to a *beating* behavior along the waveguide.

The physical modes of **NR** waveguides are already very close to linear polarization and hence are directly excited by linear polarized input waves.



(a) Horizontal dimension, zoom on the right half of the waveguide.



(b) Vertical dimension.

Figure A.5.: Non-equidistant FDM grid resolution (distance between neighboring points) for computing NR waveguide modes.

A.4.3. Optimal FDM Grid

It is possible to use non-equidistant grids with the FDM. The grid resolution can thus be increased at places where we expect fast changes of the fields (i.e. at material boundaries). The drawback is that the approximation error increases at the border of regions with different resolutions [53, Chapter 4.1]. Hence, it is desirable to have only few density changes and/or no big differences.

For NR waveguides, we use the point distances shown in Fig. A.5. The horizontal resolution is very high around the rib wall, medium in the core, changes to low resolution in the cladding with two steps and to an even lower resolution right of the slab. The resolution in the left half of the waveguide is the same, but mirrored. In the vertical direction, we have a high density around the bottom and top of the slab, as well as at the top of the rib. The density is medium in the core and low below the slab and above the rib. Figure A.6 shows the resulting grid around the right upper corner of the rib.

It is clear that we do have some places with large difference in point distances. However, the changes are in places with relatively low field magnitudes and there are not too many changes in total, limiting the introduced error. The benefit of having a finer resolution at places with rapidly changing fields outweighs the drawbacks.

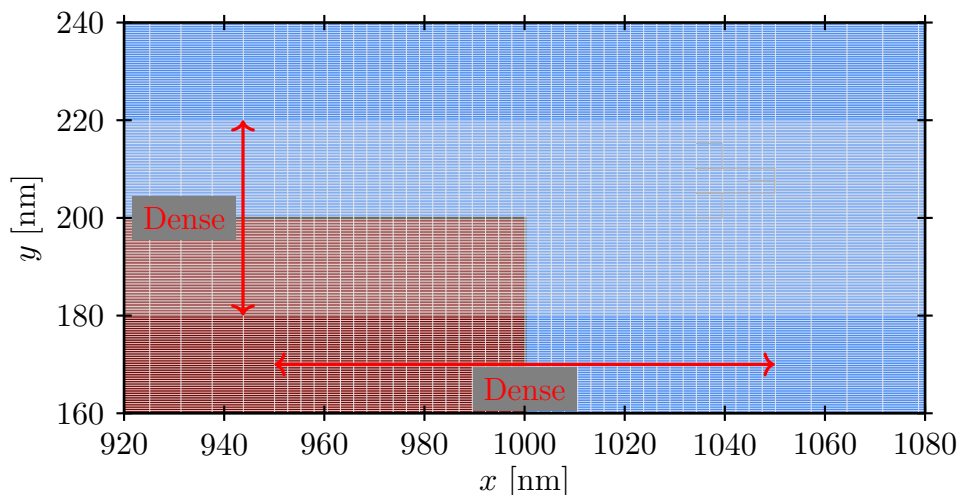


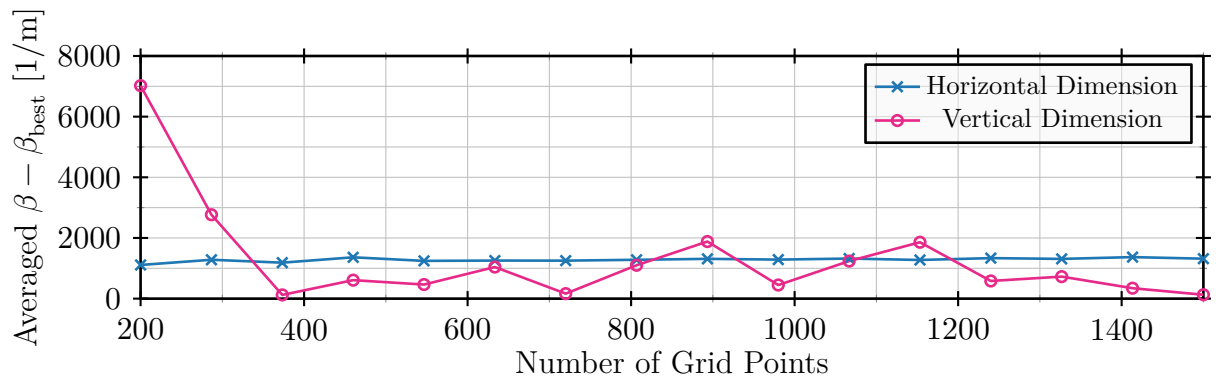
Figure A.6.: Non-equidistant FDM grid mesh for computing NR waveguide modes, zoom on the upper right corner of the rib.

The reader might have noticed in Figs. A.5a and A.5b that point distances are much higher in horizontal direction. We found that the vertical resolution has a higher impact on accuracy. To estimate this effect, we computed modes of a NR waveguide and a FMF for different grid sizes. In Fig. A.7a, we compare the resulting propagation constants against the propagation constant computed with the largest number of grid points. It is evident that the vertical dimension is much more sensitive to a variation of point distances. Based on this result, we always used 500 points in the horizontal dimension and 1000 points in the vertical dimension. Figure A.7b shows the optimization for a FMF. It is not possible to define meaningful non-equidistant grids for the circular geometry of fibers (in contrast to finite-element methods, where the mesh can freely be chosen) and hence we use an equidistant one. We decided to use 600 points in both dimensions.

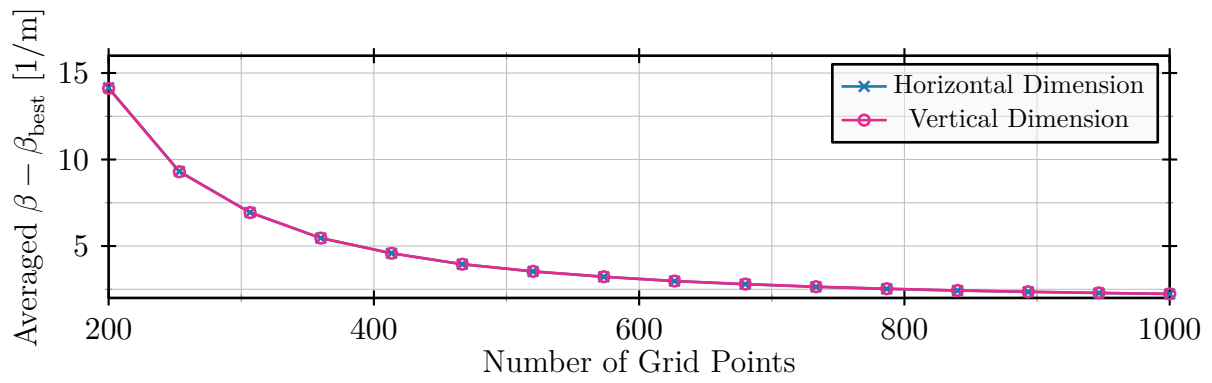
A.4.4. PM Optimization for Fibers

A caveat when we perform PM for fibers is that their FWM bandwidth is very low. For example, the experiment in [15] has $B_{\text{FWM}} \approx 2$ nm (actually even less if the region around the pump is excluded). When we try to optimize PM for the full range from O- to U-band, we would need way too many pixels in our algorithm explained in Section 3.1 to achieve a high enough resolution. Furthermore, the values for enforced separation between pumps and signal etc. in Section 3.1 are for NR waveguides. That choice of values excludes all PM configurations in fibers since B_{FWM} is always zero with them.

However, we can still use our optimization when we artificially decrease the fiber length from several kilometers to, e.g., 10 m. This leads to much higher B_{FWM} values and our algorithm works well for the optimization. Of course, such a low interaction length would lead to very low idler powers and nonfunctional FWM in reality. It also means that our simulated FWM bandwidths are a lot higher than in reality. Hence, for those calculations the actual fiber length has to be used. This approach works well when we want to compare PM in fibers and not between fibers and NR waveguides.



(a) Nano-rib waveguide.



(b) Few-mode fiber.

Figure A.7.: The effect of grid resolution on computed propagation constants.

B

Lists, Notation and Abbreviations

B.1. List of Figures

1.1. Schematic of a routing scenario where all-optical WLC helps to resolve a wavelength conflict.	2
1.2. Simple schematic of a transmission system with optical phase conjugation. . . .	3
2.1. The coordinate system used for light propagation throughout the thesis.	7
2.2. Effective, material and waveguide dispersion of the fundamental modes in a FMF and NR waveguide.	10
2.3. Wavelength dependent refractive index of different materials.	12
2.4. Refractive index profile of a graded index, depressed cladding FMF.	14
2.5. Transversal electric field distributions of four modes of FMF 2 (graded index) in Table 2.2.	15
2.6. Normalized relative group delay and dispersion of four selected modes in different FMFs.	16
2.7. Refractive index profile of a NR waveguide with layer stack and rails.	17
2.8. Variants of the NR waveguide with tunable parameters.	18
2.9. Transversal electric field distributions of the four lowest order modes of waveguide 1 (regular) in Table 2.3.	19
2.10. Transversal electric field distributions of the four lowest order modes of waveguide 2 (dips) in Table 2.3.	19
2.11. Normalized relative group delay and dispersion of the four lowest order modes in selected NR waveguides.	21
2.12. Refractive index regions of a buried rectangular waveguide, defined in Marcatili's approximation.	23
2.13. Non-equidistant discretization grid used in the FDM solvers.	26
2.14. Transversal electric field distributions of six modes of FMF 2 (graded index) in Table 2.2, computed with the linear polarized solver.	28
2.15. Schematic of different types of electron potential wells.	30

2.16. Frequencies generated by nonlinear propagation of two and three sinusoidal waves in a nonlinear medium.	32
2.17. Energy diagrams and frequencies for a BS and an OPC FWM process.	34
2.18. Energy diagrams of the two Raman scattering processes.	36
2.19. Stimulated Raman scattering contribution to the BS process in Fig. 2.17.	36
2.20. The two types of possible phonons in a crystal.	37
2.21. Energy diagram of two-photon absorption.	37
2.22. Working principle of inter-modal FWM-based all-optical signal processing.	38
2.23. Example of an OPC FWM process.	38
2.24. Phase matching diagrams in a crystal and in a waveguide.	39
2.25. An example of overlapped mode fields of waveguide 1 (regular) in Table 2.3, demonstrating good and bad nonlinear interaction.	41
3.1. Signal and idler range combinations considered in this work.	44
3.2. Example of FWM efficiency in a fiber, for the BS process.	45
3.3. An example of the graphical phase matching approach introduced in Section 3.1.2.	47
3.4. Hypothetical optimal group delay curves leading to broadband intra-band PM for the OPC process.	47
3.5. An example of PM of third kind in a NR waveguide.	48
3.6. Highest achievable FWM bandwidths for C- to O-band WLC in waveguides with different geometries.	49
3.7. FWM bandwidth for different dip configurations in a NR waveguide for O- to O-band WLC.	52
3.8. Normalized relative group delays for two waveguides of Fig. 3.7.	52
4.1. Rib wall with random roughness.	61
4.2. Simulated power evolution in NR waveguide.	64
4.3. Simulated power evolution of pumps, signal and idler in fiber 3 (depressed cladding) of Table 2.2.	65
5.1. Highest achievable FWM bandwidths for FMFs and NR waveguides with different geometries.	69
5.2. FWM bandwidths for FMFs and NR waveguides with enforced high nonlinearity coefficients.	70
5.3. Approximate nonlinearity coefficients for the configurations in Fig. 5.2.	71
5.4. Simulated evolution of the BS idler in a NR waveguide with five different propagation settings.	73
6.1. Back to back measurements of a second generation waveguide's transmission with only negligible waveguide length.	76
6.2. CW power transmission and linear mode coupling of a second generation waveguide.	76
6.3. Normalized relative group delays of the two waveguides in Chapter 6.	77
6.4. Group delays of the first generation waveguides for nominal and best-fitting geometry values.	78
6.5. Group delays of the second generation waveguides for nominal and best-fitting geometry values.	79

6.6. The effect of rib wall tilts on the MSE between measured and simulated group delays.	79
6.7. Measured FWM efficiency of the second generation waveguide.	80
6.8. Simulated and measured normalized idler power in experiment 1 from Table 6.1.	81
6.9. Simulated and measured normalized idler power in experiment 2 from Table 6.1.	82
6.10. Simulated idler power evolution along the waveguides in the experiments in Chapters 6 and 7.	83
6.11. Highest achievable FWM bandwidths and nonlinearity parameters for the two experiments in Table 6.1, in waveguides with different geometries.	84
7.1. Highest achievable FWM bandwidths and corresponding nonlinearity parameters for the three operation modes from Table 7.1, in waveguides with different geometries.	86
7.2. Normalized relative group delay of the TE ₂ mode in the fifth generation waveguide.	86
7.3. Estimates of normalized idler power in the three operation modes from Table 7.1.	88
A.1. Spectra of different representations of the same signal.	92
A.2. Typical form of the FWM efficiency, its derivative and approximate derivative. .	96
A.3. Simulated power evolution of pumps, signal and idler in a fiber, with perfect PM and with linear attenuation.	97
A.4. Simulated power evolution of pumps, signal and idler similar to Fig. A.3, but with approximations.	98
A.5. Non-equidistant FDM grid resolution for computing NR waveguide modes. . . .	102
A.6. Non-equidistant FDM grid mesh for computing NR waveguide modes.	103
A.7. The effect of grid resolution on computed propagation constants.	104

B.2. List of Tables

2.1. Sellmeier (-like) coefficients of different materials.	11
2.2. Parameters of FMFs used in the thesis.	13
2.3. Parameters of NR waveguides used in the thesis.	13
3.1. Optimization results of our work in [33].	50
3.2. Geometry parameter search space for a small optimization over dip parameters.	51
4.1. Simulated propagating waves in the NR waveguide example.	63
4.2. Simulated propagating waves in the optical fiber example. Rows denote in which modes the signals are (mode indices and mode names) and columns denote which frequencies the signals have (frequency indices and wavelength values).	65
5.1. Geometry values considered for optimizations.	68
5.2. Attenuation values for simulation B in Fig. 5.4.	73

6.1. Parameters of the first and second generation waveguides and their operation modes.	75
7.1. Parameters of the fifth generation waveguide and its three planned operation modes.	87

B.3. Mathematical Notation

$ \cdot $	Absolute Value
\propto	Approximately Proportional to
$\partial_z^2(\cdot)$	Short Form of Partial Derivative w.r.t. z
$\nabla \cdot (\mathbf{A})$	Divergence Operator
$\nabla(a)$	Gradient Operator
$\nabla \times (\mathbf{A})$	Curl Operator
$\Delta(\cdot) = (\partial_x^2 + \partial_y^2 + \partial_z^2)(\cdot)$	Laplace Operator
$(\dots) + \text{c.c.}$	Complex Conjugate of Terms in the Ellipsis
$(\cdot)^*$	Complex Conjugate
$(\cdot)^T$	Transpose
$(\cdot)^H$	Hermitian (Complex Conjugate Transpose)
$\delta(t)$	Dirac's Delta Distribution
δ_{ik}	Kronecker's Delta Symbol
$F(f) = \mathcal{F}\{f(t)\}$	Fourier Transform
$f(t) = \mathcal{F}^{-1}\{F(f)\}$	Inverse Fourier Transform
$f(t) \circ \bullet F(f)$	Fourier Pair
$\mathcal{OP}\{\cdot\}$	A Generic Operator
$\mathbf{A} \cdot \mathbf{B}$	Inner Product
$\overset{\leftrightarrow}{\mathbf{x}}^{[2]} : \mathbf{BC}$	Contraction of Third Rank Tensor With Two Vectors
$\overset{\leftrightarrow}{\mathbf{x}}^{[3]} : \mathbf{BCD}$	Contraction of Fourth Rank Tensor With Three Vectors
$\mathbf{A} \times \mathbf{B}$	Cross Product
$(x \otimes y)(t)$	Convolution of Two Functions
$(\cdot) * (\cdot)$	Multiplication (Used When Split Across Lines)
$\mathcal{Re}\{\cdot\}$	Real Part
$\mathcal{Im}\{\cdot\}$	Imaginary Part
x or X	Scalar
\mathbf{x} or \mathbf{X}	Vector
$\underline{\mathbf{x}}$ or $\underline{\mathbf{X}}$	Matrix
$\underline{\mathbf{1}}$	Identity Matrix
$\overset{\leftrightarrow}{\mathbf{x}}^{[n]}$ or $\overset{\leftrightarrow}{\mathbf{X}}^{[n]}$	Tensor of Rank n

B.4. Symbols

Symbol	Description	Unit
$(\cdot)^{(m)}$	Quantity At Frequency f_a and in Mode m	
$A_{\text{eff}x}^{(mopq)}$	Cross Effective Area Among Modes m, o, p, q	m^2
α	Waveguide Attenuation	dB/km
$k_0 = \omega\sqrt{\varepsilon_0\mu_0}$	Wave Number in Vacuum	$1/\text{m}$
$k = nk_0 = \omega\sqrt{\varepsilon\mu_0}$	Wave Number in a Medium With Refr. Index n	$1/\text{m}$
$\beta = n_{\text{eff}}k_0$	Propagation Constant	$1/\text{m}$
β_i	i -th Term of the Taylor Series Expansion of β	s^i/m
$\overline{\Delta\beta}^{(m\circ\sigma')}$	Linear Phase Mismatch	$1/\text{m}$
$\Delta\beta_{a+bcd}^{(m\circ pq)}$	Nonlinear Phase Mismatch	$1/\text{m}$
β_{TPA}	Two Photon Absorption Coefficient	m/W
B_{FWM}	FWM Bandwidth	Hz or nm
c_0	Speed of Light in Vacuum	m/s
CE_{IO}	Input-Output Conversion Efficiency	
$\vec{\chi}^{[1]}, \vec{\chi}^{[3]}, \vec{\chi}^{[1]}, \vec{\chi}^{[3]}$	Time and Frequency Dependent Linear and Third Order Susceptibility Tensors in Time and Frequency Domain	$1/\text{s}$, $\text{m}^2/\text{V}^2/\text{s}^3$, -, $\text{m}^2/\text{V}^2/\text{s}^2$
D	Chromatic Dispersion	$\text{ps}/(\text{nm km})$
\hat{E}, Ψ	Amplitude and Transversal Profile of the \mathbf{E} Field	V/m , -
η_{FWM}	FWM Efficiency	
$\mathbf{E}, \mathbf{H}, \mathbf{D}, \mathbf{B}$	Electric and Magnetic Fields and Flux Densities	V/m , A/m , C/m^2 , Wb/m^2
ε_0	Vacuum Permittivity	F/m
ε_r	Relative Permittivity	
ε'_r	Waveguiding and Material Dispersion Induced By $\vec{\chi}^{[1]}(f)$	
$\underline{\Delta\varepsilon}_r$	Linear Perturbations Part Induced By $\vec{\chi}^{[1]}(f)$	
ε''_r	Source of Linear Attenuation in Maxwell Equations	
$\Delta\varepsilon_r$	Random Perturbations of the Permittivity in the Linear Coupling Model	
f	Frequency	Hz
$\omega = 2\pi f$	Angular Frequency	$1/\text{s}$
$\gamma^{(mopq)}$	Nonlinearity Parameter Among Modes m, o, p, q	$1/(\text{W m})$
γ_{grad}	Refractive Index Grading Exponent	

Symbol	Description	Unit
h, \hbar	(Reduced) Planck's Constant	$\text{m}^2\text{kg}/\text{s}$
λ	Wavelength	m
L_{wg}	Propagation Length in the Waveguide	m
$\mathbb{L}_a^{(m \leftrightarrow o')}$	Linear Mode Coupling Coefficient From Mode o' to Mode m	1/m
$\mathbb{N}_{a \leftrightarrow bcd}^{(m \leftrightarrow opq)}$	Nonlinear Mode Coupling Coefficient From Modes o, p, q to Mode m	$\text{m}/\text{V}^2/\text{s}^2$
HE, EH, TE, TM, LP	Mode Names	
μ_0	Vacuum Permeability	H/m
μ_r	Relative Permeability	
n	Refractive Index	
Δn	Refractive Index Difference Between Core and Cladding	
n_2	Nonlinear Refractive Index	
\mathbf{P}	Material Polarization Vector	C/m^2
\mathbf{P}	Linear and Nonlinear Perturbations	C/m^2
\mathcal{P}_X	Power of Wave X	dBm or W
P_1, P_2, S, I	Pump 1, Pump 2, Signal and Idler	
\mathcal{M}	Set of All Considered Modes	
\mathcal{S}	Set of All Considered Frequencies	
\mathcal{S}_a	Set of All Considered Frequencies Which Fulfill $f_a = f_b + f_c - f_d$	
t	Time	s
τ_g	Normalized Group Delay	ns/km
$\bar{\tau}_g$	Normalized Relative Group Delay	ns/km

B.5. Abbreviations

CE _{IO}	Input-Output Conversion Efficiency
B2B	Back to Back
BS	Bragg Scattering
COD	Associate Professorship of Coding and Cryptography
CW	Continuous Wave
DFG	Difference Frequency Generation
DMD	Differential Mode Delay (also called Differential Group Delay)
FCA	Free-Carrier Absorption
FDM	Finite-Difference Method
FEM	Finite-Element Method
FMF	Few-Mode Fiber
FWM	Four-Wave Mixing
1-FWM	One-Mode Four-Wave Mixing
2-FWM	Two-Mode Four-Wave Mixing
3-FWM	Three-Mode Four-Wave Mixing
4-FWM	Four-Mode Four-Wave Mixing
FPGA	Field Programmable Gate Array
FWHM	Full Width At Half Maximum
GC	Grating Coupler
HHI	Fraunhofer-Institut Heinrich-Hertz-Institut für Nachrichtentechnik
IHP	Innovations for High Performance Microelectronics GmbH
LNT	Chair of Communications Engineering
LP	Linear Polarized
LÜT	Associate Professorship of Line Transmission Technology
MSE	Mean Square Error
MUX	Multiplexer
NR	Nano-Rib
OPC	Optical Phase Conjugation
OR	Optical Rectification
PM	Phase Matching

SDM	Space-Division Multiplexing
SFG	Sum Frequency Generation
SHG	Second Harmonic Generation
SOI	Silicon On Insulator
SPM	Self-Phase Modulation
THG	Third Harmonic Generation
TPA	Two-Photon Absorption
TUB	Technische Universität Berlin
TUM	Technische Universität München
WLC	Wavelength Conversion
XPM	Cross-Phase Modulation

Bibliography

- [1] R.-J. Essiambre and R. W. Tkach, “Capacity trends and limits of optical communication networks”, *Proc. IEEE*, vol. 100, pp. 1035–1055, May 2012.
- [2] R.-J. Essiambre, G. Kramer, P. J. Winzer, G. J. Foschini, and B. Goebel, “Capacity limits of optical fiber networks”, *J. Lightw. Technol.*, vol. 28, pp. 662–701, Feb. 2010.
- [3] R. S. Luis, G. Rademacher, B. J. Puttnam, *et al.*, “1.2 Pb/s throughput transmission using a 160 μ m cladding, 4-core, 3-mode fiber”, *J. Lightw. Technol.*, vol. 37, pp. 1798–1804, Apr. 15, 2019.
- [4] B. J. Puttnam, R. S. Luis, G. Rademacher, *et al.*, “0.61 Pb/s S, C, and L-band transmission in a 125 μ m diameter 4-core fiber using a single wideband comb source”, *J. Lightw. Technol.*, vol. 39, pp. 1027–1032, Feb. 15, 2021.
- [5] F. Yan, W. Miao, T. Li, Y. Maeda, Z. Cao, and N. Calabretta, “Monolithically integrated wavelength converter for intra-data center routing applications”, *IEEE Photon. Technol. Lett.*, vol. 28, pp. 2854–2857, Dec. 15, 2016.
- [6] S. Yoo, “Wavelength conversion technologies for WDM network applications”, *J. Light. Technol.*, vol. 14, pp. 955–966, Jun. 1996.
- [7] I. Sackey, A. Gajda, A. Peczek, *et al.*, “1024 Tb/s wavelength conversion in a silicon waveguide with reverse-biased p-i-n junction”, *Opt. Express*, vol. 25, p. 21 229, Sep. 4, 2017.
- [8] A. Amari, O. A. Dobre, R. Venkatesan, O. S. S. Kumar, P. Ciblat, and Y. Jaouen, “A survey on fiber nonlinearity compensation for 400 Gb/s and beyond optical communication systems”, *IEEE Commun. Surv. Tutorials*, vol. 19, pp. 3097–3113, Win. 2017.
- [9] G. He, “Optical phase conjugation: Principles, techniques, and applications”, *Prog. Quantum Electron.*, vol. 26, pp. 131–191, May 2002.
- [10] D. M. Pepper and A. Yariv, “Compensation for phase distortions in nonlinear media by phase conjugation”, *Opt. Lett.*, vol. 5, p. 59, Feb. 1, 1980.
- [11] S. Watanabe, T. Chikama, G. Ishikawa, T. Terahara, and H. Kuwahara, “Compensation of pulse shape distortion due to chromatic dispersion and Kerr effect by optical phase conjugation”, *IEEE Photon. Technol. Lett.*, vol. 5, pp. 1241–1243, Oct. 1993.
- [12] A. Gajda, F. Da Ros, E. P. da Silva, *et al.*, “Silicon waveguide with lateral p-i-n diode for nonlinearity compensation by on-chip optical phase conjugation”, presented at the Optical Fiber Communication Conference, Optical Society of America, 2018.
- [13] A. E. Willner, S. Khaleghi, M. R. Chitgarha, and O. F. Yilmaz, “All-optical signal processing”, *J. Light. Technol.*, vol. 32, pp. 660–680, Feb. 2014.

-
- [14] R.-J. Essiambre, M. A. Mestre, R. Ryf, *et al.*, “Experimental investigation of inter-modal four-wave mixing in few-mode fibers”, *IEEE Photon. Technol. Lett.*, vol. 25, pp. 539–542, Mar. 2013.
- [15] G. Rademacher, R. S. Luis, B. J. Puttnam, *et al.*, “Investigation of intermodal four-wave mixing for nonlinear signal processing in few-mode fibers”, *IEEE Photon. Technol. Lett.*, vol. 30, pp. 1527–1530, Sep. 1, 2018.
- [16] C. Koos, L. Jacome, C. Poulton, J. Leuthold, and W. Freude, “Nonlinear silicon-on-insulator waveguides for all-optical signal processing”, *Opt. Express*, vol. 15, p. 5976, May 14, 2007.
- [17] M. L. Zimmermann, “Monolithic electronic-photonic co-integration in photonic BiCMOS”, p. 3, 2016.
- [18] K. S. Kim, W. A. Reed, K. W. Quoi, and R. H. Stolen, “Measurement of the nonlinear index of silica-core and dispersion-shifted fibers”, *Opt. Lett.*, vol. 19, p. 257, Feb. 15, 1994.
- [19] R. M. Jr. Osgood, N. C. Panoiu, J. I. Dadap, *et al.*, “Engineering nonlinearities in nanoscale optical systems: Physics and applications in dispersion-engineered silicon nanophotonic wires”, *Adv. Opt. Photon.*, vol. 1, p. 162, Jan. 1, 2009.
- [20] A. Gajda, “Four wave mixing at 1550 nm in silicon waveguides: Enhancement and application”, Dipl.Ing, Technischen Universität Berlin, 2017.
- [21] J. Chen and S. Gao, “Wavelength-assignable 1310/1550 nm wavelength conversion using completely phase-matched two-pump four-wave mixing in a silicon waveguide”, *Opt. Commun.*, vol. 356, pp. 389–394, Dec. 2015.
- [22] M. A. Foster, A. C. Turner, R. Salem, M. Lipson, and A. L. Gaeta, “Broad-band continuous-wave parametric wavelength conversion in silicon nanowaveguides”, *Opt. Express*, vol. 15, p. 12949, 2007.
- [23] A. C. Turner-Foster, M. A. Foster, R. Salem, A. L. Gaeta, and M. Lipson, “Frequency conversion over two-thirds of an octave in silicon nanowaveguides”, *Opt. Express*, vol. 18, p. 1904, Feb. 1, 2010.
- [24] D. Wu, L. Shen, H. Ren, *et al.*, “Four-wave mixing-based wavelength conversion and parametric amplification in submicron silicon core fibers”, *IEEE J. Sel. Topics Quantum Electron.*, vol. 27, pp. 1–11, Mar. 2021.
- [25] Z. Xu, Q. Jin, Z. Tu, and S. Gao, “All-optical wavelength conversion for telecommunication mode-division multiplexing signals in integrated silicon waveguides”, *Appl. Opt.*, vol. 57, p. 5036, Jun. 20, 2018.
- [26] S. Signorini, M. Finazzer, M. Bernard, M. Ghulinyan, G. Pucker, and L. Pavesi, “Silicon photonics chip for inter-modal four wave mixing on a broad wavelength range”, *Front. Phys.*, vol. 7, p. 128, Sep. 13, 2019.
- [27] C. Lacava, M. A. Eftabib, T. D. Bucio, *et al.*, “Intermodal Bragg-scattering four wave mixing in silicon waveguides”, *J. Lightwave Technol.*, vol. 37, pp. 1680–1685, Apr. 1, 2019.
- [28] M. Ding, M. Zhang, S. Hong, *et al.*, “High-efficiency four-wave mixing in low-loss silicon photonic spiral waveguides beyond the singlemode regime”, *Opt. Express*, vol. 30, p. 16362, May 9, 2022.

- [29] D. Vukovic, J. Schröder, F. Da Ros, *et al.*, “Multichannel nonlinear distortion compensation using optical phase conjugation in a silicon nanowire”, *Opt. Express*, vol. 23, p. 3640, Feb. 9, 2015.
- [30] I. Sackey, C. Schmidt-Langhorst, C. Schubert, and J. Fischer, “Fiber nonlinearity mitigation using optical phase conjugation based on inter-modal FWM”, in *45th Eur. Conf. Opt. Commun. ECOC 2019*, Dublin, Ireland: Institution of Engineering and Technology, 2019, 276 (4 pp.)–276 (4 pp.)
- [31] R. Freund, N. Hanik, and L. Zimmermann, *Ultra-broadband photonic signal-processor (project number 403154259, part of SPP 2111)*, Deutsche Forschungsgemeinschaft (DFG). [Online]. Available: <https://gepris.dfg.de/gepris/projekt/403154259>.
- [32] T. Kernetzky and N. Hanik, “Numerical phase matching optimization for multimode silicon nano-rib waveguides”, in *2019 21st Int. Conf. Transparent Opt. Netw. ICTON*, Angers, France: IEEE, Jul. 2019, pp. 1–4.
- [33] T. Kernetzky, Y. Jia, and N. Hanik, “Multi dimensional optimization of phase matching in multimode silicon nano-rib waveguides”, presented at the Photonic Networks; 21st ITG-Symposium, Leipzig, Germany, Nov. 24, 2020, p. 8.
- [34] T. Kernetzky, G. Ronniger, U. Höfler, L. Zimmermann, and N. Hanik, “Numerical optimization and CW measurements of SOI waveguides for ultra-broadband C-to-O-band conversion”, in *2021 Eur. Conf. Opt. Commun. ECOC*, Bordeaux, France: IEEE, Sep. 13, 2021, pp. 1–4.
- [35] G. Ronniger, I. Sackey, T. Kernetzky, *et al.*, “Efficient ultra-broadband C-to-O band converter based on multi-mode silicon-on-insulator waveguides”, in *2021 Eur. Conf. Opt. Commun. ECOC*, Bordeaux, France: IEEE, Sep. 13, 2021, pp. 1–4.
- [36] U. Höfler, T. Kernetzky, and N. Hanik, “Modeling material susceptibility in silicon for four-wave mixing based nonlinear optics”, in *2021 Int. Conf. Numer. Simul. Optoelectron. Devices NUSOD*, Turin, Italy: IEEE, Sep. 13, 2021, pp. 121–122.
- [37] T. Kernetzky and N. Hanik. “Phase matching for multimode four-wave mixing in few-mode fibers and nano-rib waveguides”. arXiv: [2208.05894](https://arxiv.org/abs/2208.05894). (Aug. 11, 2022), [Online]. Available: <http://arxiv.org/abs/2208.05894> (visited on 08/12/2022), preprint.
- [38] N. Hanik, T. Kernetzky, Y. Jia, *et al.*, “Ultra-broadband optical wavelength-conversion using nonlinear multi-modal optical waveguides”, in *2022 13th Int. Symp. Commun. Syst. Netw. Digit. Signal Process. CSNDSP*, Porto, Portugal: IEEE, Jul. 20, 2022, pp. 832–835.
- [39] U. Höfler, T. Kernetzky, and N. Hanik, “Analysis of material susceptibility in silicon on insulator waveguides with combined simulation of four-wave mixing and linear mode coupling”, *Opt Quant Electron*, vol. 54, p. 837, Dec. 2022.
- [40] T. Kernetzky, N. Hanik, Y. Jia, *et al.*, “Optimization of ultra-broadband optical wavelength conversion in nonlinear multi-modal silicon-on-insulator waveguides”, in *2023 23rd Int. Conf. Transparent Opt. Netw. ICTON*, Bucharest, Romania: IEEE, Jul. 2, 2023, pp. 1–6.
- [41] O. Günlü, T. Kernetzky, O. İşcan, V. Sidorenko, G. Kramer, and R. Schaefer, “Secure and reliable key agreement with physical unclonable functions”, *Entropy*, vol. 20, p. 340, May 3, 2018.

- [42] H. H. Li, “Refractive index of silicon and germanium and its wavelength and temperature derivatives”, *Journal of Physical and Chemical Reference Data*, vol. 9, pp. 561–658, Jul. 1980.
- [43] J. W. Fleming, “Dispersion in GeO₂-SiO₂ glasses”, *Appl. Opt.*, vol. 23, p. 4486, Dec. 15, 1984.
- [44] J. W. Fleming and D. L. Wood, “Refractive index dispersion and related properties in fluorine doped silica”, *Appl. Opt.*, vol. 22, p. 3102, Oct. 1, 1983.
- [45] K. Tsukuma, N. Yamada, S. Kondo, K. Honda, and H. Segawa, “Refractive index, dispersion and absorption of fluorine-doped silica glass in the deep UV region”, *Journal of Non-Crystalline Solids*, vol. 127, pp. 191–196, Feb. 1991.
- [46] K. Luke, Y. Okawachi, M. R. E. Lamont, A. L. Gaeta, and M. Lipson, “Broadband mid-infrared frequency comb generation in a Si₃N₄ microresonator”, *Opt. Lett.*, vol. 40, p. 4823, Nov. 1, 2015.
- [47] Edward D. Palik, Ed., *Handbook of Optical Constants of Solids*. San Diego: Academic Press, 1985.
- [48] T. Bååk, “Silicon oxynitride; a material for GRIN optics”, *Appl. Opt.*, vol. 21, 1982.
- [49] L. Cohen, D. Marcuse, and W. Mammel, “Radiating leaky-mode losses in single-mode lightguides with depressed-index claddings”, *IEEE J. Quantum Electron.*, vol. 18, pp. 1467–1472, Oct. 1982.
- [50] L. Gruner-Nielsen, Y. Sun, J. W. Nicholson, *et al.*, “Few mode transmission fiber with low DGD, low mode coupling, and low loss”, *J. Lightwave Technol.*, vol. 30, pp. 3693–3698, Dec. 2012.
- [51] R. Maruyama, N. Kuwaki, S. Matsuo, and M. Ohashi, “Two mode optical fibers with low and flattened differential modal delay suitable for WDM-MIMO combined system”, *Opt. Express*, vol. 22, p. 14311, Jun. 16, 2014.
- [52] A. W. Snyder and J. Love, *Optical Waveguide Theory*. New York: Chapman and Hall, 1983.
- [53] K. Kawano and T. Kitoh, *Introduction to Optical Waveguide Analysis: Solving Maxwell's Equations and the Schrödinger Equation*. New York: John Wiley & Sons, 2001.
- [54] G. P. Agrawal, *Nonlinear Fiber Optics*, Fifth edition. Amsterdam: Elsevier/Academic Press, 2013, 629 pp.
- [55] E. A. J. Marcatili, “Dielectric rectangular waveguide and directional coupler for integrated optics”, *Bell Syst. Tech. J.*, vol. 48, pp. 2071–2102, Sep. 1969.
- [56] A. B. Fallahkhair, K. S. Li, and T. E. Murphy, “Vector finite difference modesolver for anisotropic dielectric waveguides”, *J. Lightw. Technol.*, vol. 26, pp. 1423–1431, Jun. 2008.
- [57] P. Lusse, P. Stuwe, J. Schule, and H.-G. Unger, “Analysis of vectorial mode fields in optical waveguides by a new finite difference method”, *J. Lightwave Technol.*, vol. 12, pp. 487–494, Mar. 1994.
- [58] T. E. Murphy and A. B. Fallahkhair, *Waveguide Mode Solver*. [Online]. Available: <https://de.mathworks.com/matlabcentral/fileexchange/12734-waveguide-mode-solver>.

- [59] J. R. Winkler and J. Brian Davies, “Elimination of spurious modes in finite element analysis”, *Journal of Computational Physics*, vol. 56, pp. 1–14, Oct. 1984.
- [60] R. W. Boyd, *Nonlinear Optics*, Third edition. Amsterdam: Elsevier, 2008, 613 pp.
- [61] P. N. Butcher and D. Cotter, *The Elements of Nonlinear Optics* (Cambridge Studies in Modern Optics). New York: Cambridge University Press, 1990, 344 pp.
- [62] R. Engelbrecht, *Nichtlineare Faseroptik: Grundlagen und Anwendungsbeispiele*. Berlin: Springer Vieweg, 2014, 516 pp.
- [63] T. Schneider, *Nonlinear Optics in Telecommunications*. Berlin; London: Springer, 2011.
- [64] M. E. Marhic, *Fiber Optical Parametric Amplifiers, Oscillators and Related Devices*. Cambridge: Cambridge University Press, 2007.
- [65] C. McKinstrie, S. Radic, and A. Chraplyvy, “Parametric amplifiers driven by two pump waves”, *IEEE J. Select. Topics Quantum Electron.*, vol. 8, pp. 538–547, May 2002.
- [66] G. G. Luther and C. J. McKinstrie, “Transverse modulational instability of counterpropagating light waves”, *J. Opt. Soc. Am. B*, vol. 9, p. 1047, Jul. 1, 1992.
- [67] D. Dimitropoulos, R. Claps, Y. Han, and B. Jalali, “Nonlinear optics in silicon waveguides: Stimulated Raman scattering and two-photon absorption”, presented at the Integrated Optoelectronics Devices, Y. S. Sidorin and A. Tervonen, Eds., San Jose, CA, Jun. 17, 2003, p. 140.
- [68] K. O. Hill, D. C. Johnson, B. S. Kawasaki, and R. I. MacDonald, “CW three-wave mixing in single-mode optical fibers”, *J. Appl. Phys.*, vol. 49, pp. 5098–5106, Oct. 1978.
- [69] Y. Xiao, R.-J. Essiambre, M. Desgroseilliers, *et al.*, “Theory of intermodal four-wave mixing with random linear mode coupling in few-mode fibers”, *Opt. Express*, vol. 22, p. 32 039, Dec. 29, 2014.
- [70] M. Borghi, C. Castellan, S. Signorini, A. Trenti, and L. Pavesi, “Nonlinear silicon photonics”, *J. Opt.*, vol. 19, p. 093 002, Sep. 1, 2017.
- [71] G. Rademacher and K. Petermann, “Nonlinear gaussian noise model for multimode fibers with space-division multiplexing”, *J. Lightw. Technol.*, vol. 34, pp. 2280–2287, May 1, 2016.
- [72] MathWorks, *MATLAB ode113 solver*. [Online]. Available: <https://de.mathworks.com/help/matlab/ref/ode113.html>.
- [73] D. Marcuse, *Theory of Dielectric Optical Waveguides*. New York: Academic Press, 1974.
- [74] D. Melati, A. Melloni, and F. Morichetti, “Real photonic waveguides: Guiding light through imperfections”, *Adv. Opt. Photon.*, vol. 6, p. 156, Jun. 30, 2014.
- [75] J. Zhang, Q. Lin, G. Piredda, R. W. Boyd, G. P. Agrawal, and P. M. Fauchet, “Anisotropic nonlinear response of silicon in the near-infrared region”, *Appl. Phys. Lett.*, p. 4, 2007.
- [76] D. Marcuse and P. K. A. Wai, “Application of the Manakov-PMD equation to studies of signal propagation in optical fibers with randomly varying birefringence”, *J. Light. Technol.*, vol. 15, p. 12, 1997.
- [77] G. Ronniger, S. Lischke, C. Mai, L. Zimmermann, and K. Petermann, “Investigation of inter-modal four wave mixing in p-i-n diode assisted SOI waveguides”, in *2020 IEEE Photonics Soc. Summer Top. Meet. Ser. SUM*, Cabo San Lucas, Mexico: IEEE, Jul. 2020.